

Document downloaded from:

<http://hdl.handle.net/10251/154098>

This paper must be cited as:

Adam-Ortiz, R.; Mon, M.; Greco, R.; Kalinke, LH.; Vidal Moya, JA.; Fernandez, A.; Winpenny, RE.... (2019). Self-Assembly of Catalytically Active Supramolecular Coordination Compounds within Metal Organic Frameworks. *Journal of the American Chemical Society*. 141(26):10350-10360. <https://doi.org/10.1021/jacs.9b03914>



The final publication is available at

<https://doi.org/10.1021/jacs.9b03914>

Copyright American Chemical Society

Additional Information

# Self-Assembly of Catalytically-Active Supramolecular Coordination Compounds within Metal-Organic Frameworks

Rosa Adam,<sup>§,◇</sup> Marta Mon,<sup>†,◇</sup> Rossella Greco,<sup>§</sup> Lucas H. G. Kalinke,<sup>†</sup> Alejandro Vidal-Moya,<sup>§</sup> Antonio Fernandez,<sup>\*,‡</sup> Richard E. P. Winpenny,<sup>♣</sup> Antonio Doménech-Carbó,<sup>♦</sup> Antonio Leyva-Pérez,<sup>\*,§</sup> Donatella Armentano,<sup>\*,♣</sup> Emilio Pardo<sup>\*,†</sup> and Jesús Ferrando-Soria<sup>\*,†</sup>

<sup>§</sup>Instituto de Tecnología Química (UPV-CSIC), Universidad Politècnica de València-Consejo Superior de Investigaciones Científicas, Avda. de los Naranjos s/n, 46022 Valencia, Spain.

<sup>†</sup>Departamento de Química Inorgánica, Instituto de Ciencia Molecular (ICMol), Catedrático José Beltrán Martínez, 2, Universidad de Valencia, 46980 Paterna, Valencia, Spain.

<sup>♣</sup>Chemistry Department, Sir David Davies Building, Loughborough University, Loughborough LE11 3TU, United Kingdom.

<sup>♦</sup>School of Chemistry and Photon Science Institute, The University of Manchester, Oxford Road, Manchester M13 9PL, United Kingdom.

<sup>◇</sup>Departament de Química Analítica, Universitat de València, Dr. Moliner, 50, 46100 Burjassot, València, Spain.

<sup>\*</sup>Dipartimento di Chimica e Tecnologie Chimiche (CTC), Università della Calabria, via P. Bucci, 12, Rende 87036, Cosenza, Italy.

<sup>◇</sup>These authors equally contributed to the work.

---

**ABSTRACT:** Supramolecular Coordination Compounds (SCCs) represent the power of Coordination Chemistry methodologies to self-assemble discrete architectures with targeted properties. SCCs are generally synthesised in solution, with isolated fully-coordinated metal atoms as structural nodes, thus severely limited as metal-based catalysts. Metal-Organic Frameworks (MOFs) show unique features to act as chemical nanoreactors for the *in-situ* synthesis and stabilization of otherwise not accessible functional species. Here, we present the self-assembly of Pd<sup>II</sup> SCCs within the confined space of a preformed MOF (SCCs@MOF) and its post-assembly metalation to give a Pd<sup>II</sup>-Au<sup>III</sup> supramolecular assembly, crystallography underpinned. These SCCs@MOF catalyse the coupling of boronic acids and/or alkynes, representative multisite metallic-catalysed reactions in which traditional SCCs tend to decompose, and retain its structural integrity as consequence of the synergetic hybridization between SCCs and MOF. These results open new avenues in both the synthesis of novel SCCs and their use on heterogeneous metal-based Supramolecular Catalysis.

---

## INTRODUCTION

Supramolecular chemistry methodologies have demonstrated its ability to self-assemble supramolecular coordination compounds (SCCs) with targeted properties.<sup>1-8</sup> An elegant exponent is catalysis within the unique confined environment of SCCs. Initially, it was inspired by nature with enzyme-mimicking approaches, and then, it expanded its interest into abiotic catalytic process merging environment catalysis with traditional homogeneous organotransition metal catalyst.<sup>9-13</sup> However, despite the remarkable results obtained, we consider that Supramolecular Catalysis has not yet developed with all its potential strength. This is, to some extent, directly related to the fact that the self-assembly of SCCs is done in homogenous chemistry in solution. This synthetic approach inherently induces the formation of SCCs with isolated fully-coordinated metal atoms as structural nodes, which hampers any activation of external reagents on the metal sites without destroying the assembly,

thus severely limiting their use in metal-based Supramolecular Catalysis. This is exemplified by the few reactions reported with the archetypal roughly spherical polyhedra of general formula Pd<sub>n</sub>L<sub>2n</sub>, in catalytic amounts,<sup>14-17</sup> as well as by the need to build up ensembles with already known catalytically-active metalloligands as linkers.<sup>18-20</sup> Thus, a new avenue of research may be opened by finding ways to exploit the metal-catalysis of the pivotal metal atoms building the SCCs. The implementation of such a challenging task is two-fold relevant: (*i*) unprecedented functional SCCs could be developed, otherwise not accessible, which may represent a deep impact on other related research areas; and (*ii*) the catalytic potential of pivotal metal atoms could be fully unleashed, which would widen the scope of Supramolecular Catalysis.<sup>21-23</sup>

Metal-organic frameworks (MOFs)<sup>24-29</sup> have been proved as excellent platforms for a wide range of applications. This is mainly a direct consequence of two unique features of MOFs: (*i*) a rich host-guest chemistry, which can be tailored

by a fine control over the size, shape and functionality of MOFs channels,<sup>30–35</sup> and (ii) the possibility to use single-crystal X-ray crystallography as a definitive characterization tool, which offers the unique possibility –among porous materials– to contrast the success of synthetic methodologies, and even more important, to follow/understand what is actually happening within MOFs channels.<sup>36–40</sup> So far, this has been reflected on the considerable advances performed in such diverse fields as the adsorption and separation of guest gases<sup>41–45</sup> or small molecules,<sup>46–48</sup> and catalysis.<sup>49–54</sup> However, even if some advances have been recently done related with molecular recognition<sup>55,56</sup> and/or encapsulation of complex molecular systems,<sup>57–59</sup> there is still much work to be done in relation to the use of MOFs as chemical nanoreactors.<sup>60–63</sup> At this respect, only very few examples have been reported aiming at the MOF-driven formation of supramolecular complexes within MOFs channels, which, in addition, lack of a proper structural characterization and just models could be delivered.<sup>64,65</sup>

Here, we report the *in-situ* heterogeneous self-assembly, and structural characterization by single crystal X-ray diffraction (SCXRD), of three original mechanically-bonded SCCs within the unique confined space of MOF channels (SCCs@MOF). In particular, we report a novel Pd<sub>8</sub> square metal-organic polygon, a discrete Pd<sub>16</sub> supramolecular cage and a heterobimetallic Au<sup>III</sup>–Pd<sup>II</sup> cage. All these robust SCCs catalyse, heterogeneously, the homocoupling of boronic acids, alkynes, and the cross-coupling between them, with higher catalytic activity and selectivity than homogeneous Pd catalysts while retaining its structural integrity, in contrast to traditional coordination cages assembled in solution. This behaviour emerges from the synergetic hybridization between SCCs and MOFs, which enables both the formation of otherwise not accessible supramolecular assemblies and its stabilization under catalytic conditions by mechanical-bonds to exploit the metal-based catalysis of pivotal metal atoms.

## RESULTS AND DISCUSSION

Herein, we propose a unique template-directed strategy, involving the use of Post-Synthetic Methodologies (PSMs),<sup>66–69</sup> for the sequential synthesis of SCCs@MOF. Firstly, we selected as chemical nanoreactor a highly crystalline MOF, of formula  $[\text{Pd}^{\text{II}}(\text{NH}_3)_4][\text{Pd}^{\text{II}}_2(\mu\text{-O})(\text{NH}_3)_6](\text{NH}_4)_2]_{0.5}\{\text{Ni}^{\text{II}}_4[\text{Cu}^{\text{II}}_2(\text{Me}_3\text{mpba})_2]_3\} \cdot 52\text{H}_2\text{O}$  (**1**),<sup>61</sup> featuring large octagonal pores (virtual diameter of *ca.* 2.0 nm) which are occupied by Pd<sub>2</sub> dimers, stabilized and defined, with atomic precision, to reside on preferential positions of the channels (Figure 1 left and Figure 3a center). Then, after a careful analysis –*i.e.* the available void space, the distance between Pd<sub>2</sub> units and the amount of available Pd<sup>II</sup> ions– crystals of **1** were soaked with a solution of linear (L<sub>1</sub>) and bended (L<sub>2,3</sub>) ligands (Figure 1) to yield unprecedented MOF-templated *in-situ* heterogeneous self-assembled SCCs within channels. This was directly related to both, the unique confined environment provided by MOF channels, and also the presence of such uncommon dinuclear oxo-bridged palladium(II) entities in the MOFs pores.

In particular, a novel Pd<sub>8</sub> square metal-organic polygon of formula  $[\text{Pd}^{\text{II}}_2(\mu\text{-OH})_2(\text{NH}_3)_4]_{0.5}[\text{Pd}^{\text{II}}_8(\mu\text{-OH})_8(\text{NH}_3)_8(\text{L}_1)_4]_{0.125}\{\text{Ni}^{\text{II}}_4[\text{Cu}^{\text{II}}_2(\text{Me}_3\text{mpba})_2]_3\} \cdot 43\text{H}_2\text{O}$  (**2**)

was grown when using the linear ligand L<sub>1</sub> (Figures 2, 3a left and 3b), and with the tripodal bended ligand L<sub>2</sub> (Figures 3a right and 3c) a water-assisted Pd<sup>II</sup><sub>16</sub> supramolecular assembly of formula  $[\text{Pd}^{\text{II}}_{16}(\text{H}_2\text{O})_8(\text{NH}_3)_{24}(\mu\text{-OH})_4(\text{H}_2\text{O})_{24}(\text{L}_2)]_{0.125}\{\text{Ni}^{\text{II}}_4[\text{Cu}^{\text{II}}_2(\text{Me}_3\text{mpba})_2]_3\} \cdot 30\text{H}_2\text{O}$  (**3**) was obtained. Notice that L<sub>3</sub> has a thioether-functional group, which can act as a secondary point of coordination, once a SCC@MOF has been assembled. With L<sub>3</sub>, the consecutive self-assembly of the supramolecular complex within MOF channels and the post-assembly metalation of the preformed SCC@MOF (Figure 1b) lead to the formation of a heterobimetallic assembly of formula  $[\text{Au}^{\text{III}}_2(\mu\text{-OH})_2(\text{OH})_4]_{0.5}[\text{Au}^{\text{III}}_2\text{Cl}_6\text{Pd}^{\text{II}}_2(\text{NH}_3)_6(\text{L}_3)_2]_{0.5}[\text{Pd}^{\text{II}}_2(\mu\text{-OH})_2(\text{NH}_3)_6]_{0.5}\{\text{Ni}^{\text{II}}_4[\text{Cu}^{\text{II}}_2(\text{Me}_3\text{mpba})_2]_3\} \cdot 37\text{H}_2\text{O}$  (**4**) (Figures S8–S10).

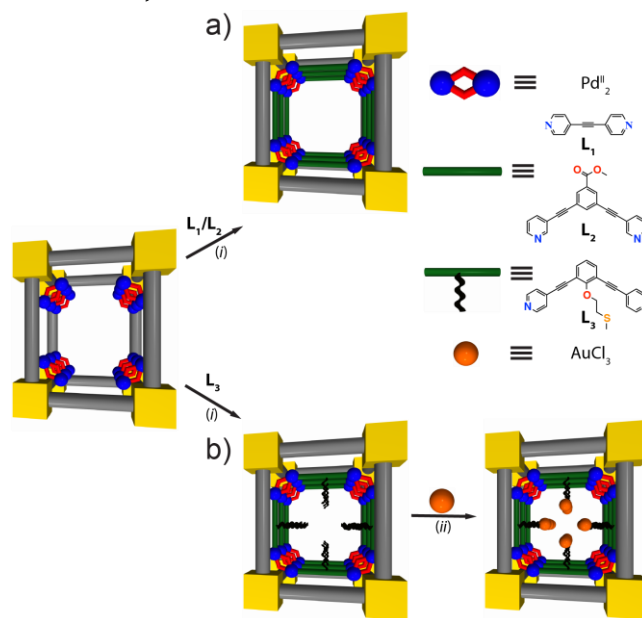


**Figure 1.** Template-directed strategy, involving the use of post-synthetic methodologies for the step-wise sequential synthesis of original homo- (a) and heterobimetallic (b) mechanically-bonded catalytically-active SCCs within the confined space of MOFs channels (SCCs@MOFs). (i) Incorporation of desired organic ligand with suitable encoded structural and coordination information and (ii) post-assembly metalation of preformed SCCs@MOFs.

The nature of **2–4** was established by the combination of a variety of different characterization techniques: inductively coupled plasma-mass spectrometry, elemental, thermo-gravimetric and powder X-Ray diffraction (PXRD) analyses, scanning electron microscopy (SEM), N<sub>2</sub> adsorption isotherm, Fourier transform infrared (FTIR), diffuse-reflectance (DR) UV-Vis and X-Ray photoelectron (XPS) spectroscopies (Figures S11–S17 and Table S1). Finally, the real crystal structures of **2** has been obtained by SCXRD. Even for **3** it was possible to refine a structural model which gives the most probably organization of entities self-assembled within pores. For **4**, the quality of the SCXRD data was not good enough for the complete structural resolution, but the crystallographic positions of the metal ions, building up the SCCs, and some ligand's fragments determined from Fourier maps, suggest precious insights about the most probable structure of the growth assemblies in the confined

space of **1**. This unprecedented result could be achieved thanks to both robustness and crystallinity of materials and application of cutting-edge X-ray crystallography techniques, providing, for the first time, a direct visualization of

the *in-situ* heterogeneous self-assembled SCCs within MOF channels (Figures 2–4, Figures S1–S10 and Table S2).

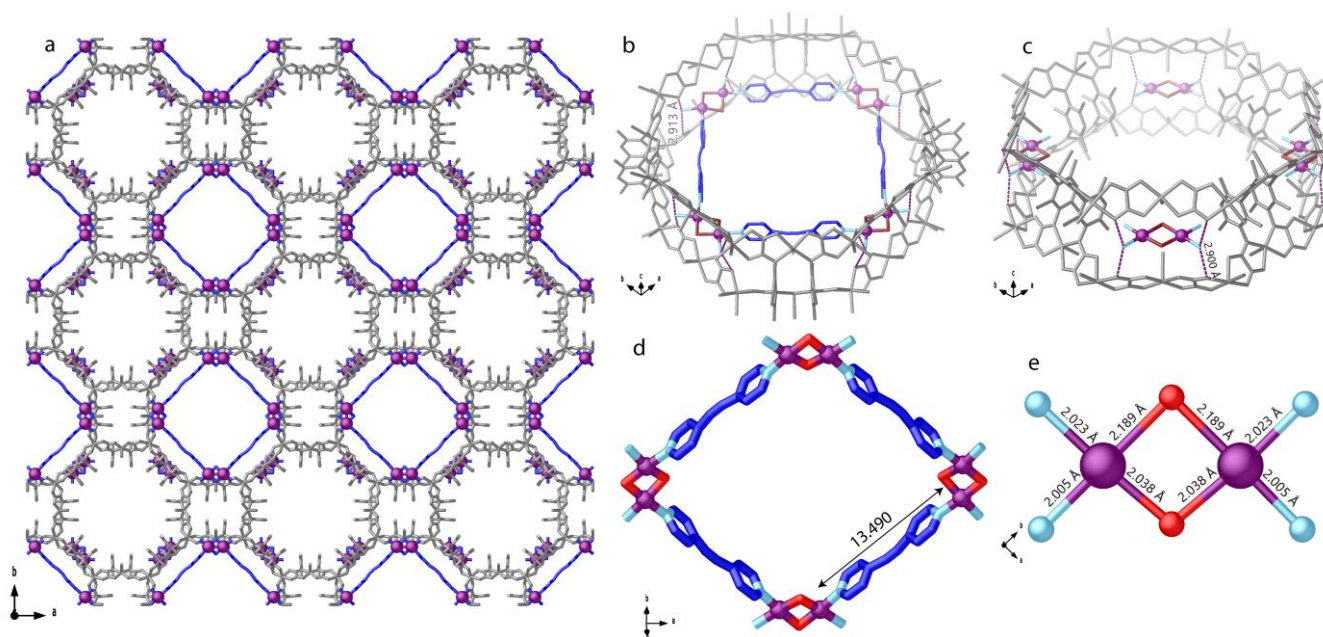


**Figure 2.** (a–e) Crystal structure, determined by synchrotron X-ray diffraction, of the Pd<sub>8</sub>@MOF **2**: (a) View along *c* crystallographic axis of crystal structure of **2** (a) featuring channels filled by [Pd<sup>II</sup><sub>8</sub>(μ-OH<sub>2</sub>)<sub>2</sub>(NH<sub>3</sub>)<sub>4</sub>]<sup>4+</sup> and [Pd<sup>II</sup><sub>8</sub>(μ-OH<sub>2</sub>)<sub>8</sub>(NH<sub>3</sub>)<sub>8</sub>(L<sub>1</sub>)<sub>4</sub>]<sup>16+</sup> SCCs [L<sub>1</sub> = 1,2-di(pyridn-4-yl)ethyne]. (b–c) Views of one single channel: Perspective views of a portion of single pores along the [111] direction showing the [Pd<sup>II</sup><sub>8</sub>(μ-OH<sub>2</sub>)<sub>8</sub>(NH<sub>3</sub>)<sub>8</sub>(L<sub>1</sub>)<sub>4</sub>]<sup>16+</sup> SCCs (b) and [Pd<sup>II</sup><sub>2</sub>(μ-OH<sub>2</sub>)(NH<sub>3</sub>)<sub>4</sub>]<sup>4+</sup> dimers (c) and related structural parameters, stabilized by symmetric NH<sub>3</sub> ⋯ O interactions. The heterobimetallic CuNi 3D anionic network is depicted as grey sticks. Pd(II) cations in the pores and ligands forming the squares and cages, are represented by purple spheres and blue sticks, respectively. Hydrogen-bonds are represented as purple dashed lines. (d–e) Details of [Pd<sup>II</sup><sub>8</sub>(μ-OH<sub>2</sub>)<sub>8</sub>(NH<sub>3</sub>)<sub>8</sub>(L<sub>1</sub>)<sub>4</sub>] and [Pd<sup>II</sup><sub>2</sub>(μ-OH<sub>2</sub>)<sub>2</sub>(NH<sub>3</sub>)<sub>4</sub>] structures built within pores. Palladium, oxygen, carbon and nitrogen atoms are represented as violet, red, blue and pastel cyan colors.

**Crystal structure.** The SCXRD data of **2–4** evidences that the 3D network remained crystalline during the MOF-templated *in-situ* heterogeneous self-assembled process. The anionic Ni<sup>II</sup><sub>4</sub>Cu<sup>I</sup><sub>6</sub> open-framework structure in **2–4** retains the known pillared square/octagonal layer architecture of **1** (Figure 2, 3 and Figures S1–S10). Both, the biggest hydrophobic octagonal channels and the square smallest pores, accommodate Pd(II) (**2–3**) and Pd(II)/Au(III) (**4**) complexes as result of L<sub>1</sub>–L<sub>3</sub> binding to either mononuclear, [Pd<sup>II</sup>(NH<sub>3</sub>)<sub>4</sub>]<sup>2+</sup>, or dinuclear complexes, [Pd<sup>II</sup><sub>2</sub>(μ-O)(NH<sub>3</sub>)<sub>6</sub>]<sup>2+</sup>, of **1** (Figures 2, 3 and Figures S1–S10). The confined assemblies in **2–4**, stabilized by mechanical-bonds with the MOF network, are strictly related to nature of the ligands (L) employed in terms of size, shape and imposed symmetry (see crystallographic section in Supplementary Information for structure refinement details and in-depth analysis of X-ray data).

In **2**, half of the Pd<sup>2+</sup> ions from the mononuclear and dinuclear entities in **1** are self-assembled by L<sub>1</sub> giving [Pd<sup>II</sup><sub>8</sub>(μ-OH<sub>2</sub>)<sub>8</sub>(NH<sub>3</sub>)<sub>8</sub>(L<sub>1</sub>)<sub>4</sub>]<sup>16+</sup> square polygons, with [Pd<sup>II</sup><sub>2</sub>(μ-OH<sub>2</sub>)<sub>2</sub>(NH<sub>3</sub>)<sub>4</sub>] dimers residing at the corners of the quadrangular SCC (Figures 2, 3a left, 3b and Figures S1–S5) and stabilized by H-bonds to the MOF. Each Pd(II) exhibits regular square planar geometry, with Pd–N [2.02(2) and 2.09(2) Å for Pd–N<sub>L1</sub> and Pd–NH<sub>3</sub>, respectively] and Pd–OH<sub>2</sub> [1.99(2)

and 2.05(2) Å] bond distances similar to those found in the literature.<sup>14–16,70</sup> The Pd(II) separations through H<sub>2</sub>O and L<sub>1</sub> bridges are 2.840(6) and 13.49(1) Å, respectively. Square polygons are regularly pillared along *c* crystallographic axes, with a Pd(II) ⋯ Pd(II) separation among adjacent polygons of 15.15(1) Å, being stabilized by mechanical-bonds with the walls of the net involving terminal NH<sub>3</sub> molecules and oxamate residues belonging to the net [H<sub>3</sub>N ⋯ O<sub>oxamate</sub> of 2.913(9) Å] (Figures S3 and S4). The synergic stabilizations ensured by hosting matrix strongly support the robustness of such assembled SCCs, with high activity in heterogeneous metal-based supramolecular catalysis (*vide infra*).

The different nature and symmetry of ligand L<sub>2</sub> imposes a totally different assembly in **3**, yielding a [Pd<sup>II</sup><sub>16</sub>(H<sub>2</sub>O)<sub>8</sub>(NH<sub>3</sub>)<sub>24</sub>(μ-OH<sub>2</sub>)<sub>4</sub>(H<sub>2</sub>O)<sub>24</sub>(L<sub>2</sub>)] supramolecular assembly, where [Pd<sup>II</sup><sub>2</sub>(NH<sub>3</sub>)<sub>6</sub>(L<sub>2</sub>)] dimers are linked by strong hydrogen bonds, through the carboxylate group of L<sub>2</sub> and H<sub>2</sub>O molecules, to [Pd<sup>II</sup><sub>2</sub>(μ-OH<sub>2</sub>)<sub>4</sub>(H<sub>2</sub>O)<sub>6</sub>] dimers for which not all waters have been found from density maps (see Supplementary Information) [O ⋯ O of 2.89(4) and 2.89(3) Å for –COO ⋯ O<sub>water</sub> and O<sub>water</sub> ⋯ O<sub>water</sub>, respectively] (Figures 3a right, 3c and Figures S6 and S7). Despite thermal and positional disorder detected for L<sub>2</sub> ligand –that clearly does not fit the space group of hosting matrix (see Figure S7 and refinement details)– the crystal structure of

SCC was solved, where Pd(II) ions exist in distorted square planar geometries with Pd-N in the  $[\text{Pd}^{\text{II}}_2(\text{NH}_3)_6(\text{L}_2)]$  dimers and Pd-OH<sub>2</sub> distances of the  $[\text{Pd}^{\text{II}}_2(\mu\text{-OH}_2)_4(\text{H}_2\text{O})_6]$  moieties falling in the expected values [1.99(1) and 2.00(1) Å for Pd-N<sub>L2</sub> and Pd-NH<sub>3</sub>, respectively, and Pd-OH<sub>2</sub> of 2.05(3) and 2.47(3) Å].<sup>14-16,70</sup> The Pd(II)⋯Pd(II) separation within  $[\text{Pd}^{\text{II}}_2(\text{NH}_3)_6(\text{L}_2)]$  dimers is of 6.1 Å whereas 8.3 Å is the

shortest Pd(II)⋯Pd(II) distance detected in Pd<sub>16</sub> assemblies. The strength of H-bonds observed in Pd<sub>16</sub> assembly of **3**, together with its stabilization by mechanical-bonds with the network, underpins the role of supramolecular interactions in *nanosolvated* space, which should be most likely able to preserve Pd<sub>16</sub> aggregates during catalysis as well.

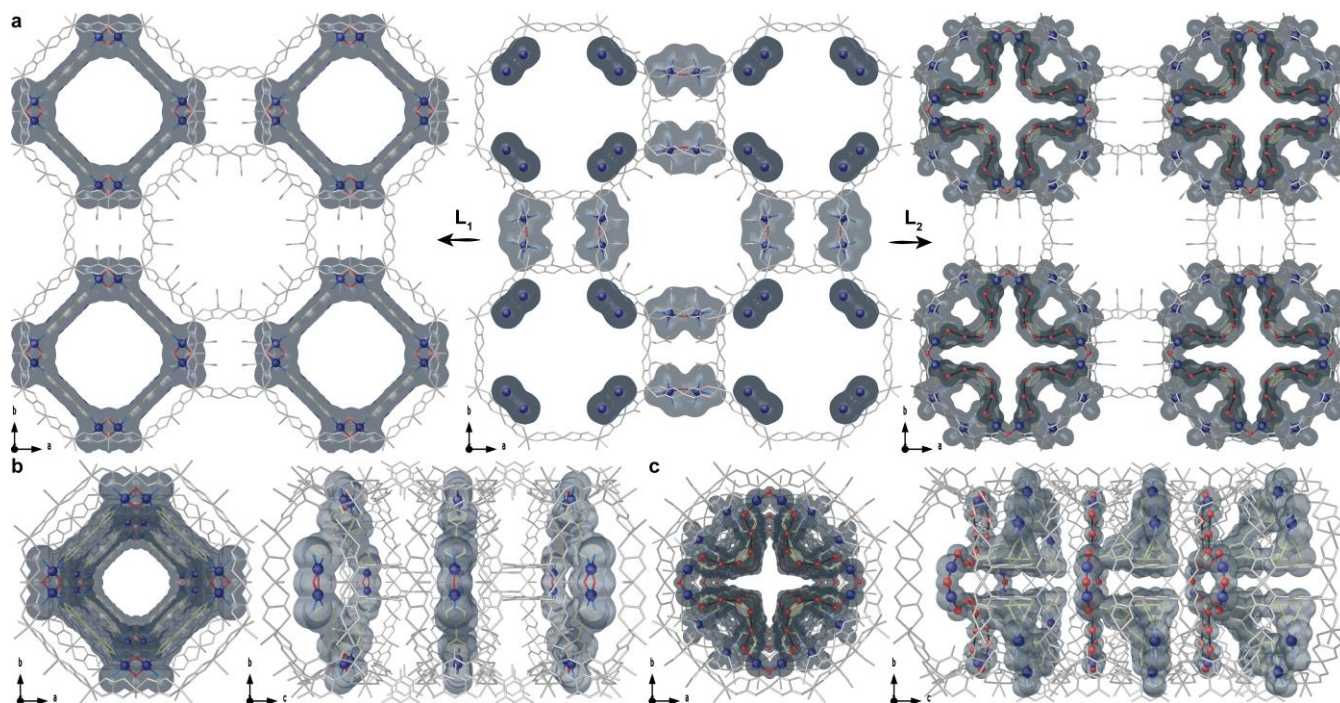


**Figure 3.** (a-c) Views of the crystal structures, determined by synchrotron X-ray diffraction, of the Pd<sub>8</sub>@MOF **2** (left) and the Pd<sub>16</sub>@MOF **3** (right) prepared from the *in-situ* reaction of the dipalladium(II)-containing MOF **1** (center) with the aromatic dipyridine ligands L<sub>1</sub> and L<sub>2</sub>, respectively [L<sub>1</sub> = 1,2-di(pyridin-4-yl)ethyne and L<sub>2</sub> = methyl 3,5-bis(pyridine-4-ylethynyl)benzoate]. Views of one single channel of **2** (b) and **3** (c) in the *ab* (left) and *bc* (right) crystallographic planes. The heterobimetallic CuNi 3D anionic network is depicted as grey sticks. Pd(II) cations in the pores of **1-3** and ligands forming the squares and cages in **2** and **3**, are represented by blue spheres and gold sticks, respectively. Hydrogen-bonds that form the water-assisted Pd<sup>II</sup><sub>16</sub> supramolecular assembly in **3** are represented as black dotted lines. Surfaces are used to highlight the SCCs within MOFs channels.

The quality of the SCXRD data did not allow the same precision for the complete visualization of SCCs' crystal structure of **4**. However, many local maxima attributable to Pd<sup>2+</sup> and Au<sup>3+</sup> metal ions in the channels together with few peaks related to L<sub>3</sub> ligand's fragments were located in the observed structure factor Fourier maps, providing evidence of the localization of the SCCs (Figures S8-S10 and refinement details in Supplementary Information). Looking at their disposition, it is rationale to hypothesize a self-assembly, in a similar manner as observed in **2**, producing  $[\text{Pd}^{\text{II}}_2(\text{NH}_3)_6(\text{L}_3)_2]$  dimers (for which no peaks related to the aromatic moiety has been found from electron density maps) remaining in big hydrophobic pores with Pd(II) in square planar geometry [average Pd-N of 2.10(2) Å]. The Pd⋯Pd and N<sub>L3</sub>⋯N<sub>L3</sub> separations within dimers of 11.36 and 13.97(1) Å fit very-well with those found for complexes constructed with similar ligands (*ca.* 14 Å).<sup>14-16</sup> These dimers further grasp AuCl<sub>3</sub> complexes exploiting the high affinity for soft metal ions of the thioether moiety<sup>71</sup> featured by L<sub>3</sub>, generating, finally, self-assembled heterometallic SCCs of the type  $[\text{Au}^{\text{III}}_2\text{Cl}_6\text{Pd}^{\text{II}}_2(\text{NH}_3)_6(\text{L}_3)_2]$  showing Pd⋯Au

and Au⋯Au separations of 13.50(1) and 11.89(1) Å, respectively (Figure S9). Interestingly the found position of Au(III) ions, consistent with L<sub>3</sub> symmetry, is displaced towards the centre of the big pores, suggesting a high accessibility for reactants. Furthermore, the solved crystal structure clearly evidences thioether fragments, allowing to unveil the Au-S distance of 2.34(1) Å.

**PXRD, TGA experiments and N<sub>2</sub> adsorption isotherms.** The experimental PXRD patterns of **2-4** are identical to the corresponding calculated ones (Figures S11-S12). This fact confirms the homogeneity of the bulk samples, which are isostructural to the crystals selected for single crystal X-ray diffraction. The solvent contents of **2-4** were established by thermogravimetric analysis (TGA) under dry N<sub>2</sub> atmosphere and compared to that of the ancestor compound **1** (Figure S13). Overall, it shows a fast mass loss for **1-4** from room temperature followed by a *pseudo* plateau until decomposition starts. Noteworthy, it is observed a greater thermal stability of **2-4** respect **1**, which further reinforce the beneficial synergetic hybridization in SCCs@MOFs. The observed weight losses of 25.72 (**1**), 21.73 (**2**), 16.47 (**3**)

and 15.73% (**4**), respectively, correspond to 52, 43, 30 and 37 water molecules, respectively, in line with that determined by CHN(S) analyses (see Supplementary Information). Figure S14 shows the N<sub>2</sub> adsorption isotherms of **1–4** at 77 K. They are consistent with the decrease in accessible void space in **2** and, more significantly, in **3** and **4**, suggested by the TGA analyses and the crystal structures, which is a direct consequence of the formation of largest supramolecular assemblies.

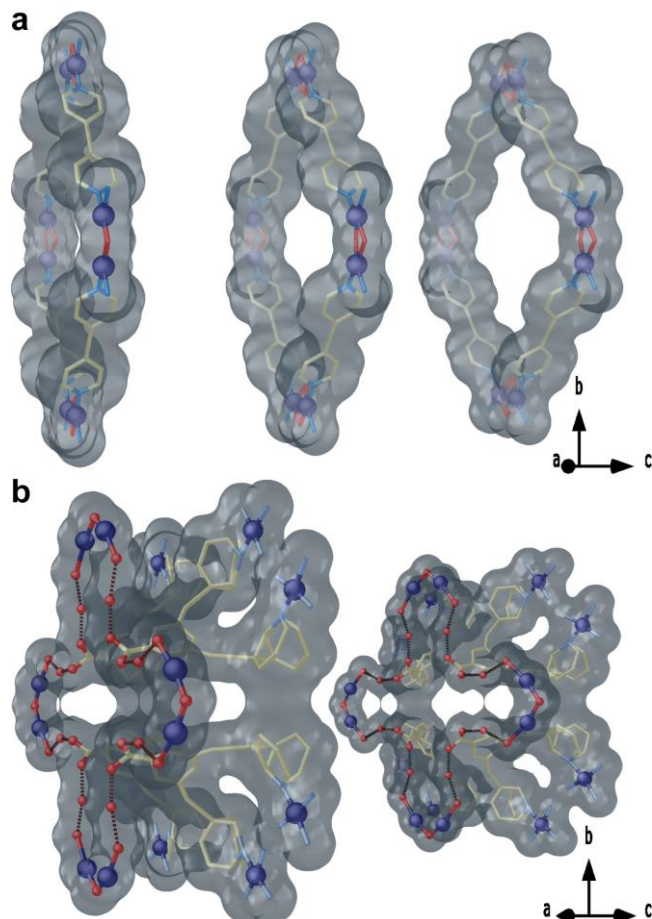


**Figure 4.** Supramolecular coordination compounds crystal structure. Perspective views of three Pd<sup>II</sup><sub>8</sub> squares (a) and two Pd<sup>II</sup><sub>16</sub> (b) supramolecular cages, unveiled by single crystal X-ray diffraction, formed within one single channel of the frameworks of **2** and **3**, respectively.

**MAS solid <sup>13</sup>C NMR, DR-UV-vis, FT-IR, Raman and XPS.** Figure S15 shows the magic angle spinning solid <sup>13</sup>C nuclear magnetic resonance (MAS solid <sup>13</sup>C NMR) of MOF **1** and SCCs@MOFs **2–4**. It can be clearly seen the appearance of new and sharper signals at 165, 150 and 90 ppm in **2**, which nicely fit the expected values for the L<sub>1</sub> ligand, together with the signals at -40, 40, 130 and 230 ppm corresponding to the framework amides, shifted and broadened by the paramagnetic action of the Cu<sup>II</sup> metal ions. Similar spectra were recorded for SCC@MOF **3** and **4**. Additionally, **4** spectrum shows a signal at 70 ppm fitting with the typical chemical shift expected for ether functionalities. Diffuse-reflectance

UV-visible measurements of **2–4** show the loss of the palladium(II) adsorption band at λ<sub>max</sub> = 320 nm observed in **1** and the appearance of three new bands at λ<sub>max</sub> = 270, 300 and 350 nm (Figure S16), which agree with both the formation of SCCs and the observed bands of a previously reported Pd<sup>II</sup><sub>4</sub>(L<sub>1</sub>)<sub>4</sub> square SCC in solution (see Figure S20).<sup>72</sup> Fourier-transformed infrared spectroscopy (FT-IR) further confirms the integrity of the structural organic parts of the SCCs@MOFs in **2–4** together with the appearance of new signals assignable to L<sub>1–3</sub> (Figure S17). Raman spectroscopy confirms the formation of the new Au-S bond by the appearance of typical bands for Au-S bonds between 200-300 and 550 cm<sup>-1</sup> (Figure S18) when exciting with a 514 nm laser light.<sup>73</sup> X-ray photoelectron spectroscopy (XPS) shows that the Pd3d<sub>5/2</sub> peak of the Pd<sup>II</sup> atoms (338.6 eV) in **1** slightly shifts for **2–4** (338.3, 338.5 and 338.1 eV, respectively), as expected by the action of the L<sub>1–3</sub> ligands (Figure S19).<sup>74</sup> These results perfectly agree with SCXRD and give us tools to follow catalysed reactions within the solids.

**Catalytic performance of SCCs@MOFs.** Oligo- and poly-thiophenes are well-known conducting molecules with applications in, for instance, solar cells.<sup>75</sup> Their synthesis relies on the Pd-catalysed homocoupling of thienylboronic acids, a challenging C-C bond-forming reaction that requires strong bases and oxidants in the presence of a poisoning sulphur group.<sup>76</sup> Figure 5 shows the results for the homocoupling of two different thienylboronic acids -**5a** and **5b**- with a representative Pd(II) complex catalyst,<sup>77</sup> the soluble SCC Pd<sup>II</sup><sub>4</sub>(L<sub>1</sub>)<sub>4</sub>,<sup>72</sup> **1–3** (Tables S3–S4 and Figures S20–21). SCCs@MOFs catalysts show much better activity and selectivity to **6a** than the homogeneous Pd catalysts and MOF **1**, with good recyclability and, in addition, are able to catalyse the homocoupling of other boronic acids (Figure S22). PXRD, DR UV-vis and MAS solid <sup>13</sup>C NMR measurements of **2** and **3** after reaction show identical spectra to the fresh samples, plus the signals corresponding to the polymeric product **6b** when starting from **5b** (Figure 5d, Figures S12 and S21). These results strongly support that the SCCs retain their structural integrity within the MOF during reaction and are true catalysts for homocoupling of boronic acids.

In order to better understand the stability of SCCs@MOFs under such challenging reaction conditions, mechanistic studies comparing them with their soluble counterpart Pd<sup>II</sup><sub>4</sub>(L<sub>1</sub>)<sub>4</sub> were performed. The kinetic equation rate is first order in all reagents for **2** and **3**, but half order respect to Pd and second order for benzoquinone for soluble Pd<sup>II</sup><sub>4</sub>(L<sub>1</sub>)<sub>4</sub> (Figure 6a, Figures S23–S27).<sup>76,78</sup> *In-situ* <sup>1</sup>H NMR measurements show the rapid degradation of soluble Pd<sup>II</sup><sub>4</sub>(L<sub>1</sub>)<sub>4</sub> after addition of **5a**, with release of free L<sub>1</sub> to the medium and coordination of benzoquinone to Pd<sup>II</sup> ions while the reaction occurs<sup>78</sup> (Figure 5e, Figure S28). Any attempt to re-assemble Pd<sup>II</sup><sub>4</sub>(L<sub>1</sub>)<sub>4</sub> produces a linear decrease of the initial rate (Figure S29) and O<sub>2</sub> is required as an oxidant (Tables S5 and S6),<sup>77,79</sup> which is not the case in the heterogeneous coupling. These results show that Pd<sup>II</sup><sub>4</sub>(L<sub>1</sub>)<sub>4</sub> is just a precursor of the Pd catalytic species while, in clear contrast, **2** and **3** remain untouched and catalytically active during the heterogeneous reaction.

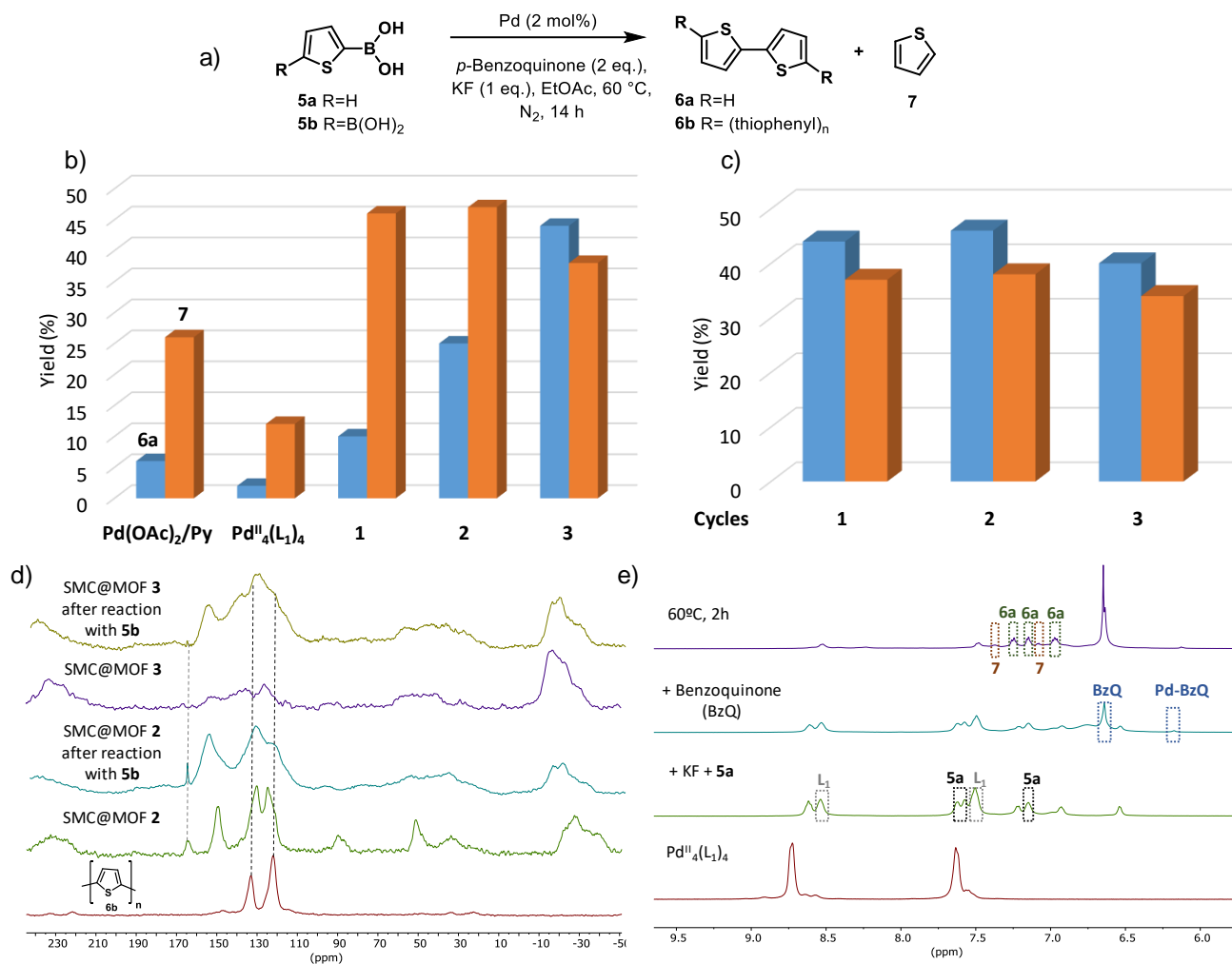


**Figure 5.** (a) Homocoupling of thienylboronic acids **5a** and **5b** in the presence of 2 mol % of Pd, **5a-b** (0.1 mmol), KF (0.1 mmol, 5.8 mg), *p*-benzoquinone (0.2 mmol, 21.6 mg), EtOAc (1.5 mL) and dodecane (10  $\mu$ L) as internal standard, under N<sub>2</sub>, at 60 $^{\circ}$ C, during 14h. (b) Yields of **6a** and **7** in the homocoupling of **5a** catalyzed by Pd(OAc)<sub>2</sub>/Py (1/1), Pd<sub>4</sub>(L<sub>1</sub>)<sub>4</sub>, MOF **1**, SCC@MOF **2** and **3**. (c) Reuses for SCC@MOF **3** in the homocoupling of **5a**. (d) From bottom to top: MAS solid <sup>13</sup>C NMR of polymer **6b**, SCC@MOF **2**, SCC@MOF **2** after reaction with **5b**, SCC@MOF **3** and SCC@MOF **3** after reaction with **5b**. (e) Aromatic area of Pd<sub>4</sub>(L<sub>1</sub>)<sub>4</sub> <sup>1</sup>H NMR spectra (CD<sub>3</sub>CN/D<sub>2</sub>O) after the sequential addition of KF (2 eq), **5a** (2 eq) and benzoquinone (2 eq) and the treatment of the mixture at 60  $^{\circ}$ C during 2 h.

XPS measurements after treating **2** and **3** inside the chamber with an O<sub>2</sub> atmosphere do not show any Pd<sup>IV</sup> signals (Figure 6b). Cyclic voltammetry of **3** during the reaction of **5a** shows that the cathodic signal assignable to the Pd<sup>II</sup> atoms of the SCC@MOF (C<sub>Pd(II)</sub>) evolves to a new signal corresponding to Pd<sup>I</sup> (C<sub>Pd(I)</sub>), significantly different to the signals of coupling product **6a**, redox active benzoquinone and uncatalysed product **7** (Figure 6c, for blank experiments see Figures S30 and S31). This bimetallic Pd<sup>I</sup>/Pd<sup>II</sup> redox manifold, without the involvement of Pd<sup>0</sup> or Pd<sup>IV</sup> species, avoids

extensive structural distortions in the mechanically-bonded assemblies and, hence, further contributes to retain their integrity during the coupling. Overall, the combined kinetic, spectroscopic and electrochemical results enable us to propose a mechanism for the homocoupling of boronic acids catalysed by **2** and **3** (Figure 6d), where the confined Pd<sup>II</sup><sub>2</sub> units catalyse the homocoupling reaction by a redox cooperative mechanism in which both Pd<sup>II</sup> metal ions reduce to Pd<sup>I</sup>, releasing **6**, and finally re-oxidize to the original form.

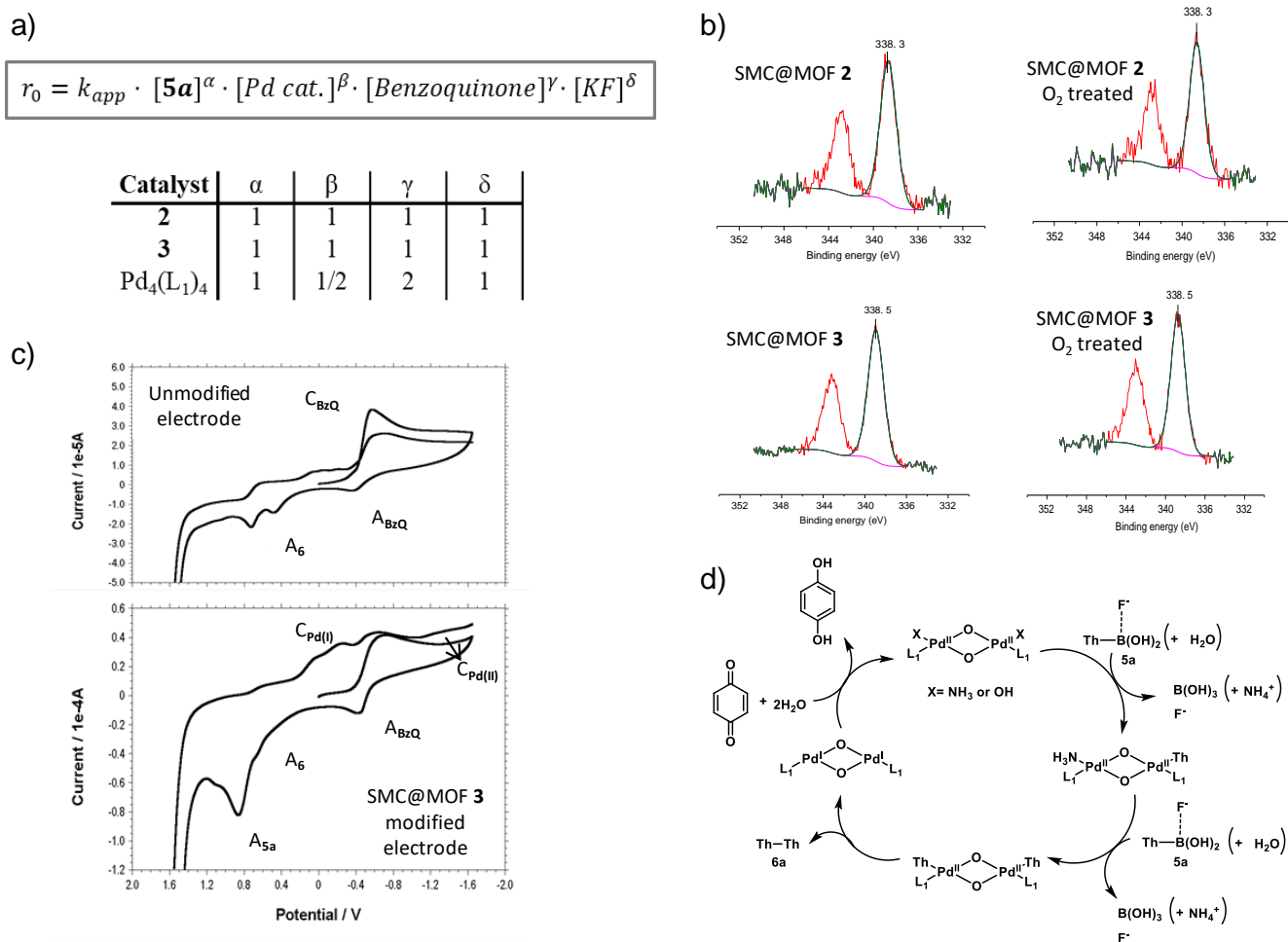


**Figure 6.** (a) Kinetic equation rate and kinetic  $\delta$  parameters for the homocoupling of thienylboronic acid **5a** calculated through initial rate values for **2**, **3** and  $Pd_4(L_1)_4$ . Reaction conditions: **5a** (0.4–0.8 mmol), KF (0–1.6 mmol), *p*-benzoquinone (0–1.6 mmol), catalyst (0–2 mol%), dodecane (40  $\mu$ L), EtOAc (6 mL) for SCC@MOF **2** and **3** or  $CH_3CN$  (6 mL) for  $Pd_4(L_1)_4$ ,  $N_2$ , 60 $^\circ$ C. (b) X-ray photoelectron spectroscopy (XPS) of SCCs@MOFs **2** (top) and **3** (bottom), before (left) and after (right), treatment in the chamber with  $O_2$  for 30 minutes. (c) *In-situ* cyclic voltammograms of a solution of **5a** (1 mM), KF (1 mM) and benzoquinone (1 mM) in 0.10 M  $Bu_4NPF_6/MeCN$  before (top) and after (bottom) modifying glassy carbon electrodes with SCC@MOF **3**, *A* stands by anodic signals and *C* stands by cathodic signals, potential scan rate was 50  $mV\ s^{-1}$ . (d) Postulated mechanism for the homocoupling of thienylboronic acid **5a** catalyzed by the  $Pd_2$  moieties in SCC@MOF **2**.

Following this mechanistic rationale, **2**, **3**, and also the heterobimetallic  $Au^{III}Pd^{II}$  **4** (Figure 7a, Tables S7 and S8), were tested as catalysts for the coupling of alkynes.<sup>80</sup> The three SCCs@MOFs were more active for homocoupling of phenylacetylene **8a** than the homogeneous Pd catalysts tested as well as than MOF **1**, with **4** affording the better selectivity to **9a**. Moreover, **4** proved its utility through the homocoupling of a series of alkynes **8b–e** and the cross coupling of phenylacetylene **8a** with **8f–h**, affording diynes **9b–h** with moderate to good yields (Figure 7d, Figures S32 and S33). Notice that a related MOF with supported thio-alkyl  $Au^{III}$  complexes, not containing Pd atoms, does not show any catalytic activity.<sup>71</sup> Kinetic and  $^1H$  NMR experiments (Figures S34–S40) confirm that, as occurs for homocoupling of **5a**: (i) homocoupling of **8a** is first order kinetics for **4** but  $\frac{1}{2}$  for  $Pd_4(L_1)_4$  (Figure 7b), (ii)  $Pd_4(L_1)_4$  readily decomposes after the addition of the reagents (Figure 7c, Figure S40), and (iii)  $O_2$  has more influence for the decomposed  $Pd_4(L_1)_4$  than for **4** (Figures S35 and S38).<sup>81</sup> Kinetic isotope

effect (KIE) for **8a** is 3.4(7) and 0.9(1) for catalysts **4** and  $Pd_4(L_1)_4$ , respectively (Figures S36 and S39), which nicely fits the observation that **8a** only intervenes in the equation rate of catalyst **4** and not of  $Pd_4(L_1)_4$ .<sup>82</sup> Following this, **2–4** were tested for the more challenging cross-coupling between boronic acid **5a** and alkyne **8a** (Figure 7e),<sup>83</sup> showing moderate conversions and selectivity, in any case higher than the homogeneous catalysts and the simpler MOF **1** (Figure 7e and Figure S41). In order to showcase the practical advantages of the SCCs@MOFs respect to other soluble and/or MOF catalysts, the homocoupling of **8a** was carried out in a fixed-bed tubular reactor with MOF **4** as a solid catalyst. The results (Figure S42) show that, indeed, alkyne **8a** transforms to the homocoupling product **9a** in flow, thus allowing to the production of diynes in continuous flow, a process difficult to achieve with other solid catalysts that make use of solid bases<sup>84</sup> or that, simply, are soluble and not solid.<sup>85</sup>

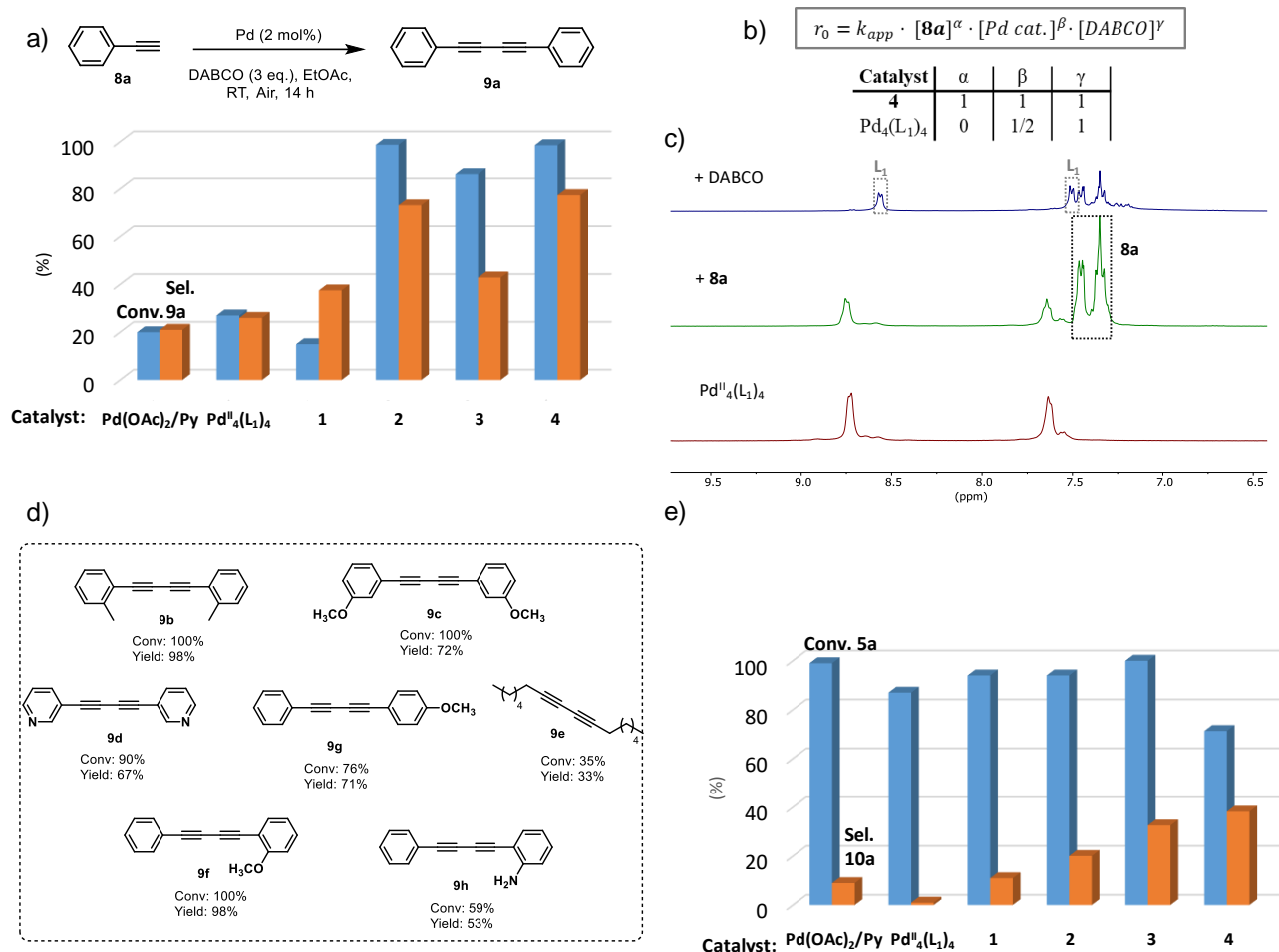


**Figure 7.** (a) Phenylacetylene **8a** conversion and diphenylbutadiyne **9a** yield for the homocoupling of **8a** catalyzed by  $Pd(OAc)_2/Py$  (1/1),  $Pd_4(L_1)_4$ , MOF **1** and SCC@MOF **2-4**. Reaction conditions: 2 mol % of Pd, **8a** (0.1 mmol, 10.1 mg), DABCO (0.3 mmol, 33.6 mg), EtOAc (1.5 mL) and dodecane (10  $\mu$ L) as an internal standard, under air atmosphere, at RT, during 14 h. (b) Kinetic equation rate and kinetic parameters for the homocoupling of phenylacetylene **8a** calculated through initial rate values for **4** and  $Pd_4(L_1)_4$ . Reaction conditions: **8a** (0.4–0.8 mmol), DABCO (0–2.4 mmol), catalyst (0–2 mol% Pd), dodecane (40  $\mu$ L), EtOAc (6 mL) for SCC@MOF **4** or  $CH_3CN$  (6 mL) for  $Pd_4(L_1)_4$ , air, 60  $^\circ$ C; (c) Aromatic area of  $Pd_4(L_1)_4$   $^1H$  NMR spectra ( $CD_3CN/D_2O$ ) after the sequential addition (from bottom to top) of **8a** (2 eq) and DABCO (2 eq); (d) Substrate scope for the homocoupling of alkynes **9b-e** and the cross coupling between phenylacetylene **8a** and alkynes **9f-h** catalyzed by SCC@MOF **4** (reaction conditions shown in the Supporting Information); (e) Thienylboronic acid **5a** conversion and **10a** yield for the cross coupling between **5a** and **8a** catalyzed by  $Pd(OAc)_2/Py$  (1/1),  $Pd_4(L_1)_4$ , MOF **1** and SCC@MOF **2-4**. Reaction conditions: 2 mol% of Pd, **5a** (0.1 mmol, 12.8mg), **8a** (0.3 mmol, 30.3 mg), KF (0.1 mmol, 5.8 mg), *p*-benzoquinone (0.2 mmol, 21.6 mg), DABCO (0.9 mmol, 100.9 mg), EtOAc (1.5 mL) and dodecane (10  $\mu$ L) as internal standard, under air atmosphere, at 60  $^\circ$ C, during 14 h.

## CONCLUSIONS

We report a unique synthetic strategy for the template-directed sequential construction of novel stable supramolecular complexes within a MOF channels, SCCs@MOF, taking advantage of the singular confined environment provided by MOF channels, and also the presence of such uncommon dinuclear Pd(II) entities in the MOFs pores. As proof-of-concept, we have synthesised and crystallographically characterized three original constructs mechanically-bonded to a MOF network, never obtained before outside the MOFs. In particular, we report a novel  $Pd_8$  square metal-organic polygon, fully characterized by SCXRD, a discrete  $Pd_{16}$  supramolecular cage and a heterobimetallic  $Au^{III}-Pd^{II}$

cage, underpinned by SCXRD. These solid SCCs catalyse the coupling of boronic acids and alkynes, while keeping the SCCs structure untouched, with better catalytic activity and selectivity than standard Pd catalysts and soluble  $Pd_4(L_1)_4$  squares, the latter readily decomposing under reaction conditions. Overall, this work, represents a general versatile approach, easily extendable to other metals and ligands, for the assembly of original supramolecular constructs with great potential in heterogeneous metal-based Supramolecular Catalysis.

## EXPERIMENTAL SECTION

**Materials.** 1,2-di(pyridin-4-yl)ethyne ( $L_1$ ), methyl 3,5-bis(pyridin-4-ylethynyl)benzoate ( $L_2$ ),  $\{[Pd^{II}(en)(L_1)]_4(NO_3)_8\}$  ( $Pd^{II}_4(L_1)_4$ )<sup>72</sup> and  $[Pd^{II}(NH_3)_4][Pd^{II}_2(\mu-H_2O)(NH_3)_6]_{0.5}\{Ni^{II}_4[Cu^{II}_2(Me_3mpba)_2\}_3\} \cdot 52H_2O$  (**1**)<sup>61</sup> were prepared according to literature procedure (see Supplementary Methods).

**Synthesis.** A detailed description for the synthesis 4,4'-(2-(2-(methylthio)ethoxy)-1,3-phenylene)bis(ethyne-2,1-diyl)dipyridine ( $L_3$ ) is given in the Supplementary Methods. For  $[Pd^{II}_2(\mu-OH_2)_2(NH_3)_4]_{0.5}[Pd^{II}_8(\mu-OH_2)_8(NH_3)_8(L_1)_4]_{0.125}\{Ni^{II}_4[Cu^{II}_2(Me_3mpba)_2\}_3\} \cdot 43H_2O$  (**2**). Well-formed deep green prisms of **2**, which were suitable for X-ray diffraction, were obtained by immersing crystals of **1** (ca. 36 mg, 0.010 mmol) in hot (50 °C) acetonitrile solutions of  $L_1$  (5 mL, 10 mM) for one week. Then, the supernatant solution was removed, and the crystals were washed with an acetonitrile solution (5 x 10 mL), isolated by filtration on paper and air-dried. Alternatively, large scale syntheses of **2**, were also carried out by using the same synthetic procedure but with stirring and with greater amounts of both, a powder sample of compound **1** (2 g, 0.55 mmol) and  $L_1$  (50 mL, 55 mM), with the same successful results. Finally, the product was collected by filtration, washed with a acetonitrile solution and air-dried. Elemental analysis [% calcd., % found for  $Cu_6Ni_4Pd_2C_{84}H_{163}N_{16}O_{81}$  (3522.17)]: C, 28.65; H, 4.67; N, 6.36%. Found: C, 28.75; H, 4.72; N, 6.31%. IR (KBr):  $\nu = 1603\text{ cm}^{-1}$  (C=O).

For  $[Pd^{II}_{16}(H_2O)_8(NH_3)_{24}(\mu-OH_2)_4(H_2O)_{24}(L_2)]_{0.125}\{Ni^{II}_4[Cu^{II}_2(Me_3mpba)_2\}_3\} \cdot 30H_2O$  (**3**). The compound **3** was prepared by an analogous procedure to that for **2** by using  $L_2$  as precursor instead of  $L_1$ . Elemental analysis [% calcd., % found for  $Cu_6Ni_4Pd_2C_{80.75}H_{139.75}N_{15.25}O_{70.75}$  (3285.2)]: C, 29.50; H, 4.25; N, 6.50%. Found: C, 29.39; H, 4.08; N, 6.23%. IR (KBr):  $\nu = 1601\text{ cm}^{-1}$  (C=O).

For  $[Au^{III}_2(\mu-OH)_2(OH)_4]_{0.5}[Au^{III}_2Cl_2Pd^{II}_2(NH_3)_6(L_3)_2]_{0.5}[Pd^{II}_2(\mu-OH_2)(NH_3)_6]_{0.5}\{Ni^{II}_4[Cu^{II}_2(Me_3mpba)_2\}_3\} \cdot 37H_2O$  (**4**). Well-shaped deep green prisms of **4**, were obtained by immersing crystals of **1** (ca. 36 mg, 0.010 mmol) in hot (50 °C) acetonitrile solutions of  $L_3$  (5 mL, 10 mM) for one week. After washing the crystals with additional acetonitrile (5 x 10 mL), they were immersed in a fresh  $H_2O/CH_3OH$  (1:1) solution. The solution was exchanged every three hours five times. Then, the crystals were treated in a  $H_2O/CH_3OH$  (1:1) solution of  $AuCl_3$  (3.0 mg, 0.010 mmol) for 12 hours. The process was repeated five more times to ensure that the maximum loading of possible gold atoms was achieved. This was monitored by ICP-MS and SEM/EDX. The gold-metallated crystals had the same size and shape as those of the starting SCC@MOF, ruling out a possible dissolution-recrystallization mechanism for this system and strongly suggesting a solid-state process in the formation of the heterobimetallic SCC@MOF. The crystals were washed with a  $H_2O/CH_3OH$  (1:1) solution (5 x 10 mL), isolated by filtration on paper and air-dried. Alternatively, large scale syntheses of **4**, were also carried out by using the same consecutive step-by-step synthetic procedure but with stirring and with greater amounts of precursors, a powder sample of compound **1** (2 g, 0.55 mmol),  $L_3$  (50 mL, 55 mM) and  $AuCl_3$  (0.17 g, 0.55

mmol) with the same successful results. The metalation of the preformed SCC@MOF was repeated five times. This was monitored by ICP-MS and SEM/EDX. Finally, the product was collected by filtration, washed with a  $H_2O/CH_3OH$  (1:1) solution and air-dried. Elemental analysis [% calcd., % found for  $Cu_6Ni_4Pd_2Au_2C_{101}H_{174}N_{20}O_{77.5}$  (4269.8)]: C, 28.39; H, 4.08; S, 0.75; N, 6.56%. Found: C, 28.85; H, 4.33; S, 0.90; N, 6.80%. IR (KBr):  $\nu = 1603\text{ cm}^{-1}$  (C=O).

**Single crystal X-ray diffraction.** Diffraction data for **2** and **4** were collected using synchrotron radiation at I19 beamline of the Diamond Light Source at  $\lambda = 0.6889\text{ \AA}$ , whereas for **3** on a Bruker-Nonius X8APEXII CCD area detector diffractometer using graphite-monochromated Mo- $K_\alpha$  radiation ( $\lambda = 0.71073\text{ \AA}$ ). Crystal data for **2-4**: tetragonal, space group  $P4/mmm$ ,  $T = 30(2)$  for **2** and  $90(2)$  K for **3**,  $Z = 4$ . **2**:  $C_{84}H_{163}Cu_6Ni_4O_{81}Pd_2$ ,  $a = 35.7158(2)\text{ \AA}$ ,  $c = 15.14950(10)\text{ \AA}$ ,  $V = 19325.0(3)\text{ \AA}^3$ ; **3**:  $C_{80.75}H_{139.75}Cu_6Ni_{15.25}Ni_4O_{70.75}Pd_2$ ,  $a = 35.258(10)\text{ \AA}$ ,  $c = 15.119(4)\text{ \AA}$ ,  $V = 18795(12)\text{ \AA}^3$ ; **4**:  $C_{101}H_{174}Cu_6N_{20}Ni_4O_{77.5}SPd_2Au_2Cl_3$ ,  $a = 35.725(2)\text{ \AA}$ ,  $c = 15.2666(8)\text{ \AA}$ ,  $V = 19485(2)\text{ \AA}^3$ . Further details can be found in the Supplementary Information.

CCDC 1892911, 1892912 and 1892914 for **2**, **3** and **4**, respectively contain the supplementary crystallographic data for this paper. These data can be obtained free of charge *via* [www.ccdc.cam.ac.uk/conts/retrieving.html](http://www.ccdc.cam.ac.uk/conts/retrieving.html) (or from the Cambridge Crystallographic Data Centre, 12 Union Road, Cambridge CB21EZ, UK; fax: (+44)1223-336-033; or [deposit@ccdc.cam.ac.uk](mailto:deposit@ccdc.cam.ac.uk)).

<sup>1</sup>H and <sup>13</sup>C NMR Spectroscopy, Magic Angle Spinning Solid <sup>13</sup>C NMR Spectroscopy, Diffuse-reflectance UV-Vis, Infrared Spectroscopy, Microscopy measurements, X-ray Powder Diffraction Measurements, X-ray photoelectron spectroscopy (XPS) measurements and Electrochemical Measurements. A detailed description of all the different characterization techniques used is given in the Supplementary Information.

**Catalytic Experiments.** A detailed description of all the catalytic experiments is given in the Supplementary Information.

## ASSOCIATED CONTENT

**Supporting Information Available.** Physical techniques. Crystallographic refinement and catalytic details. Figures S1–S42. Tables S1–S8. CCDC reference numbers: CCDC–1892911, 1892912 and 1892914. This material is available free of charge via the Internet at <http://pubs.acs.org>.

## AUTHOR INFORMATION

### Corresponding Author

\* To whom correspondence should be addressed. E-mail: [jesus.ferrando@uv.es](mailto:jesus.ferrando@uv.es); [anleyva@itq.upv.es](mailto:anleyva@itq.upv.es); [donatella.armentano@unical.it](mailto:donatella.armentano@unical.it); [a.fernandez-mato@lboro.ac.uk](mailto:a.fernandez-mato@lboro.ac.uk); [emilio.pardo@uv.es](mailto:emilio.pardo@uv.es).

### Notes

The authors declare no competing financial interests.

## ACKNOWLEDGMENT

This work was supported by the MINECO (Spain) (Projects CTQ2016–75671–P, 2017–86735–P and Excellence Units

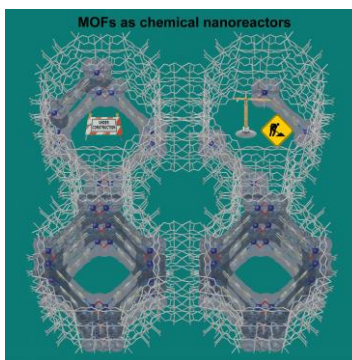
“Severo Ochoa” and “Maria de Maeztu” SEV-2016-0683 and MDM-2015-0538), the Ministero dell’Istruzione, dell’Università e della Ricerca (Italy) and the Engineering and Physical Sciences Research Council (UK). M.M. thanks the MINECO for a predoctoral contract. R.A. thanks UPV and R.G. thanks ITQ for the corresponding contracts. D.A. thanks the “Fondo per il finanziamento delle attività base di ricerca”. E.P. acknowledges the financial support of the European Research Council under the European Union’s Horizon 2020 research and innovation programme / ERC Grant Agreement No 814804, MOF-reactors. Thanks are also extended to the “Subprograma Atracció de Talent-Contractes Post-doctorals de la Universitat de Valencia” and the “2018 Leonardo Grant for Researchers and Cultural Creators, BBVA Foundation” (J.F.S.). We thank Diamond Light Source for awarded beamtime (proposal number MT18768) and provision of synchrotron radiation facility and Dr David Allan and Dr Sarah Barnett for their assistance at I19 beamline.

## REFERENCES

- Lehn, J.-M. *Supramolecular Chemistry: Concepts and Perspectives*; Wiley-VCH, Weinheim, **1995**.
- Steed, J. W.; Atwood, J. L. *Supramolecular Chemistry*; John Wiley & Sons, Chichester, **2000**.
- Chakrabarty, R.; Mukherjee, P. S.; Stang, P. J. Supramolecular Coordination: Self-Assembly of Finite Two- and Three-Dimensional Ensembles. *Chem. Rev.* **2011**, *111*, 6810–6918.
- Ward, M. D.; Raithby, P. R. Functional behaviour from controlled self-assembly: challenges and prospects. *Chem. Soc. Rev.* **2013**, *42*, 1619–1636.
- Roberts, D. A.; Pilgrim, B. S.; Nitschke, J. R. Covalent post-assembly modification in metallosupramolecular chemistry. *Chem. Soc. Rev.* **2018**, *47*, 626–644.
- Howlader, P.; Mondal, B.; Purba, P. C.; Zangrando, R.; Mukherjee, P. S. Self-Assembled Pd(II) Barrels as Containers for transient Merocyanine Form and Reverse Thermochromism of Spiropyran. *J. Am. Chem. Soc.* **2018**, *140*, 7952–7960.
- Chakraborty, S.; Newkome, G. R. Terpyridine-based metallosupramolecular constructs: tailored monomers to precise 2D-motifs and 3D-metallocages. *Chem. Soc. Rev.* **2018**, *47*, 3991–4016.
- Zhou, Z.; Chen, D.-G.; Saha, M. L.; Wang, H.; Li, X.; Chou, P.-T.; Stang, P. J. Designed Conformation and Fluorescence Properties of Self-Assembled Phenazine-Cored Platinum(II) Metal-lacycles. *J. Am. Chem. Soc.* **2019**, *141*, 5535–5543.
- Cullen, W.; Misuraca, M. C.; Hunter, C. A.; Williams, N. H.; Ward, M. D. Highly efficient catalysis of the Kemp elimination in the cavity of a cubic coordination cage. *Nat. Chem.* **2016**, *8*, 231–236.
- Howlader, P.; Das, P.; Zangrando, R.; Mukherjee, P. S. Urea-Functionalized Self-Assembled Molecular Prism for Heterogeneous Catalysis in Water. *J. Am. Chem. Soc.* **2016**, *138*, 1668–1676.
- Ueda, Y.; Ito, H.; Fujita, D.; Fujita, M. Permeable Self-Assembled Molecular Containers for Catalyst Isolation Enabling Two-Step Cascade Reactions. *J. Am. Chem. Soc.* **2017**, *139*, 6090–6093.
- Pilgrim, B. S.; Roberts, D. A.; Lohr, T. G.; Ronson, T. K.; Nitschke, J. R. Signal transduction in a covalent post-assembly modification cascade. *Nat. Chem.* **2017**, *9*, 1276–1281.
- Hong, C. M.; Bergman, R. G.; Raymond, K. N.; Toste, F. D. Self-Assembled Tetrahedral Hosts as Supramolecular Catalysts. *Acc. Chem. Res.* **2018**, *51*, 2447–2455.
- Tominaga, M.; Suzuki, K.; Kawano, M.; Kusukawa, T.; Ozeki, T.; Sakamoto, S.; Yamaguchi, K.; Fujita, M. Finite, spherical coordination networks that self-organize from 36 small components. *Angew. Chem. Int. Ed.* **2004**, *43*, 5621–5625.
- Sun, Q.-F.; Iwasa, J.; Ogawa, D.; Ishido, Y.; Sato, S.; Ozeki, T.; Sei, Y.; Yamaguchi, K.; Fujita, M. Self-Assembled  $M_{24}L_{48}$  Polyhedra and Their Sharp Structural Switch upon Subtle Ligand Variation. *Science*, **2010**, *328*, 1144–1147.
- Fujita, D.; Ueda, Y.; Sato, S.; Mizuno, N.; Kumasaka, T.; Fujita, M. Self-assembly of tetravalent Goldberg polyhedra from 144 small components. *Nature* **2016**, *540*, 563–566.
- Pradhan, S.; John, R. P. Self-assembled  $Pd_6L_4$  cage and  $Pd_4L_4$  square using hydrazide-based ligands: synthesis, characterization and catalytic activity in Suzuki-Miyaura coupling reactions. *RSC Adv.* **2016**, *6*, 12453–12460.
- Lee, S. J.; Cho, S.-H.; Mulfort, K. L.; Tiede, D. M.; Hupp, J. T.; Nguyen, S. T. Cavity-Tailored, Self-Sorting Supramolecular Catalytic Boxes for Selective Oxidation. *J. Am. Chem. Soc.* **2008**, *130*, 16828–16829.
- Li, H.; Han, Y.-F.; Lin, Y.-J.; Guo, Z.-W.; Jin, G.-X. Stepwise Construction of Discrete Heterometallic Coordination Cages Based on Self-Sorting Strategy. *J. Am. Chem. Soc.* **2014**, *136*, 2982–2985.
- Jiao, J.; Tan, C.; Li, Z.; Liu, Y.; Han, X.; Cui, Y. Design and Assembly of Chiral Coordination Cages for Asymmetric Sequential Reactions. *J. Am. Chem. Soc.* **2018**, *140*, 2251–2259.
- van Leeuwen, P. W. N. M. *Supramolecular Catalysis*; John Wiley & Sons, **2008**.
- Leenders, S. H. A. M.; Gramage-Doria, R.; de Bruin, B.; Reek, J. N. H. Transition metal catalysis in confined spaces. *Chem. Soc. Rev.* **2015**, *44*, 433–448.
- Bolliger, J. L. *Self-Assembled Coordination Cages and Organic Capsules as Catalytic Supramolecular Reaction Vessels*; Springer International Publishing, Cham, **2017**, 17–48. In *Effects of Nanoconfinement in Catalysis* (ed. Poli, R.)
- Furukawa, H.; Cordova, K. E.; O’Keeffe, M.; Yaghi, O. M. The chemistry and applications of metal-organic frameworks. *Science* **2013**, *341*, 974.
- Maurin, G.; Serre, C.; Cooper, A.; Férey, G. The new age of MOFs and of their porous-related solids. *Chem. Soc. Rev.* **2017**, *46*, 3104–3107.
- Yuan, S.; Feng, L.; Wang, K.; Pang, J.; Bosch, M.; Lollar, C.; Sun, Y.; Qin, J.; Yang, X.; Zhang, P.; Wang, Q.; Zou, L.; Zhang, Y.; Zhang, L.; Fang, Y.; Li, J.; Zhou, H.-C. Stable Metal-Organic Frameworks: Design, Synthesis, and Applications. *Adv. Mater.* **2018**, 1704303.
- Majewski, M. B.; Peters, A. W.; Wasielewski, M. R.; Hupp, J. T.; Farha, O. K., Metal-Organic Frameworks as Platforms Materials for Solar Fuels Catalysis. *ACS Energy Letters* **2018**, *3*, 598–611.
- He, Y.; Chen, F.; Li, B.; Qian, G.; Zhou, W.; Chen, B. Porous metal-organic frameworks for fuel storage. *Coord. Chem. Rev.* **2018**, *373*, 167–198.
- Hosono, N.; Kitagawa, S. Modular Design of Porous Soft Materials via Self-Organization of Metal-Organic Cages. *Acc. Chem. Res.* **2018**, *51*, 2437–2446.
- Deng, H.; Grunder, S.; Cordova, K. E.; Valente, C.; Furukawa, H.; Hmadeh, M.; Gándara, F.; Whalley, A. C.; Liu, Z.; Asahina, S.; Kazumori, H.; O’Keeffe, M.; Terasaki, O.; Stoddart, J. F.; Yaghi, O. M. Large-pore apertures in a series of metal-organic frameworks. *Science*. **2012**, *336*, 1018–1023.
- Fracaroli, A. M.; Furukawa, H.; Suzuki, M.; Dodd, M.; Okajima, S.; Gándara, F.; Reimer, J. A.; Yaghi, O. M. Metal-Organic Frameworks with Precisely Designed Interior for Carbon Dioxide Capture in the Presence of Water. *J. Am. Chem. Soc.* **2014**, *136*, 8863–8866.
- Bin, W.; Lv, X.-L.; Feng, D.; Xie, L.-H.; Zhang, J.; Li, M.; Xie, Y.; Li, J.-R.; Zhou, H.-C. Highly Stable Zr(IV)-Based Metal-Organic Frameworks for the Detection and Removal of Antibiotics and Organics Explosives in Water. *J. Am. Chem. Soc.* **2016**, *138*, 6204–6216.
- Li, P.; Chen, Q.; Wang, T. C.; Vermeulen, N. A.; Mehdi, B. L.; Dohnalkova, A.; Browning, N. D.; Shen, D.; Anderson, R.; Gómez-Gualdrón, D. A.; Cetin, F. M.; Jagiello, J.; Asiri, A. M.; Stoddart, J. F.; Farha, O. K. Hierarchically Engineered Mesoporous Metal-Organic Frameworks Toward Cell-free Immobilized Enzyme Systems. *Chem* **2018**, *4*, 1022–1034.
- Jiang, H.; Jia, J.; Shkurenko, A.; Chen, Z.; Adil, K.; Belmabkhout, Y.; Weselinski, L. J.; Assen, A. H.; Xue, D.-X.; O’Keeffe, M.; Ed-daoudi, M. Enriching the Reticular Chemistry Repertoire: Merged Nets Approach for the Rational Design of Intricate Mixed-Linker Metal-Organic Framework Platforms. *J. Am.*

- Chem. Soc.* **2018**, *140*, 8858–8867.
- (35) Guillerm, V.; Grancha, T.; Imaz, I.; Juanhuix, J.; Maspoch, D. Zig-zag Ligands for Transversal Design in Reticular Chemistry: Unveiling New Structural Opportunities for Metal-Organic Frameworks. *J. Am. Chem. Soc.* **2018**, *140*, 10153–10157.
- (36) Ferguson, A.; Liu, L.; Tapperwijn, S. J.; Perl, D.; Coudert, F.-X.; Cleuvenbergen, S. V.; Verbiest, T.; van der Veen, M. A.; Telfer, S. G. Controlled partial interpenetration in metal-organic frameworks. *Nat. Chem.* **2016**, *8*, 250–257.
- (37) Burgun, A.; Coghlan, C. J.; Huang, D. M.; Chen, W.; Horike, S.; Kitagawa, S.; Alvino, J. F.; Metha, G. F.; Sumbly, C. J.; Doonan, C. J. Mapping-Out Catalytic Processes in a Metal-Organic Framework with Single-Crystal X-ray Crystallography. *Angew. Chem. Int. Ed.* **2017**, *129*, 8532–8536.
- (38) Li, P.; Vermeulen, N. A.; Malliakas, C. D.; Gómez-Gualdrón, D. A.; Howarth, A. J.; Mehdi, B. L.; Dohnalkova, A.; Browning, N. D.; O’Keeffe, M.; Farha, O. K. Bottom-up construction of a superstructure in a porous uranium-organic crystal. *Science* **2017**, *356*, 624–627.
- (39) Lee, S.; Bürgi, H.-B.; Alshimiri, S. S.; Yaghi, O. M. Impact of Disordered Guest-Framework Interactions on the Crystallography of Metal-Organic Frameworks. *J. Am. Chem. Soc.* **2018**, *140*, 8958–8964.
- (40) Albalad, J.; Xu, H.; Gándara, F.; Haouas, M.; Martineau-Corcoss, C.; Mas-Ballesté, R.; Barnett, S. A.; Juanhuix, J.; Imaz, I.; Maspoch, D. Single-Crystal-to-Single-Crystal Postsynthetic Modification of a Metal-Organic Framework via Ozonolysis. *J. Am. Chem. Soc.* **2018**, *140*, 2028–2031.
- (41) Cadiou, A.; Adil, K.; Bhatt, P. H.; Belmabkhout, Y.; Eddaoudi, M. A metal-organic framework-based splitter for separating propylene form propane. *Science* **2016**, *353*, 137–140.
- (42) Schoedel, A.; Ji, Z.; Yaghi, O. M. The role of metal-organic frameworks in a carbon-neutral energy cycle. *Nature Energy*, **2016**, *1*, 16034.
- (43) Cadiou, A.; Belmabkhout, Y.; Adil, K.; Bhatt, P. M.; Pillai, R. S.; Shkurenko, A.; Martineau-Corcoss, C.; Maurin, G.; Eddaoudi, M. Hydrolytically stable fluorinated metal-organic frameworks for energy-efficient dehydration. *Science* **2017**, *356*, 731–735.
- (44) Han, X.; Godfrey, H. G. W.; Briggs, L.; Davies, A. J.; Cheng, Y.; Daemen, L. L.; Sheveleva, A. M.; Tuna, F.; McInnes, E. J. L.; Sun, J.; Drathen, C.; George, M. W.; Ramirez-Cuesta, A. J.; Thomas, M.; Yang, S.; Schröder, M. Reversible adsorption of nitrogen dioxide within a robust porous metal-organic framework. *Nat. Mater.* **2018**, *17*, 691–696.
- (45) Chen, Z.; Li, P.; Zhang, X.; Li, P.; Wasson, M. C.; Islamoglu, T.; Stoddart, J. F.; Farha, O. K. *J. Am. Chem. Soc.* **2019**, *141*, 2900–2905.
- (46) Mon, M.; Lloret, F.; Ferrando-Soria, J.; Martí-Gastaldo, C.; Armentano, D.; Pardo, E. Selective and Efficient Removal of Mercury from Aqueous Media with the Highly Flexible Arms of a BioMOF. *Angew. Chemie Int. Ed.* **2016**, *55*, 11167–11172.
- (47) Navarro-Sanchez, J.; Argente-Garcia, A. I.; Moliner-Martinez, Y.; Roca-Sanjuan, D.; Antypov, D.; Campins-Falco, P.; Rosseinsky, M. J.; Marti-Gastaldo, C. Peptide Metal-Organic Frameworks for Enantioselective Separation of Chiral Drugs. *J. Am. Chem. Soc.* **2017**, *139*, 4294–4297.
- (48) Zhao, X.; Wang, Y.; Li, D. S.; Bu, X.; Feng, P. Metal-organic frameworks for separation. *Adv. Mater.* **2018**, *30*, 1705189.
- (49) Dhakshinamoorthy, A.; Asiri, A. M.; Garcia, H. Metal-organic frameworks catalyzed C–C and C–heteroatom coupling reactions. *Chem. Soc. Rev.* **2015**, *44*, 1922–1947.
- (50) Zhang, T.; Manna, K.; Lin, W. Metal-Organic Frameworks Stabilize Solution-Inaccessible Cobalt Catalysts for Highly Efficient Broad-Scope Organic Transformations. *J. Am. Chem. Soc.* **2016**, *138*, 3241–3249.
- (51) Ly Thi, H.; Fu, G.; Kondinski, A.; Bueken, B.; De Vos, D.; Vogt, T. Superactivity of MOF-808 toward Peptide Bond Hydrolysis. *J. Am. Chem. Soc.* **2018**, *140*, 6325–6335.
- (52) Lan, G.; Zhu, Y.-Y.; Veroneau, S. S.; Xu, Z.; Micheroni, D.; Lin, W. Electron Injection from Photoexcited Metal-Organic Framework Ligands to Ru<sub>2</sub> Secondary Building Units for Visible-Light-Driven Hydrogen Evolution. *J. Am. Chem. Soc.* **2018**, *140*, 5326–5329.
- (53) Zhang, X.; Huang, Z.; Ferrandon, M.; Yang, D.; Robinson, L.; Li, P.; Wang, T. C.; Delferro, M.; Farha, O. K. Catalytic chemoselective functionalization of methane on a metal-organic framework. *Nature Catalysis* **2018**, *1*, 356–362.
- (54) Shen, K.; Zhang, L.; Chen, X.; Liu, L.; Zhang, D.; Han, Y.; Chen, J.; Long, J.; Luque, R.; Li, Y.; Chen, B. Ordered macro-microporous metal-organic framework single crystals. *Science* **2018**, *359*, 206–210.
- (55) Dong, Z.; Sun, Y.; Chu, J.; Zhang, X.; Deng, H. Multivariate Metal-Organic Frameworks for Dialing-in the Binding and Programming the Release of Drug Molecules. *J. Am. Chem. Soc.* **2017**, *139*, 14209–14216.
- (56) Mon, M.; Bruno, R.; Ferrando-Soria, J.; Bartella, L.; Di Donna, L.; Talia, M.; Lappano, R.; Maggolini, M.; Armentano, D.; Pardo, E. Crystallographic snapshots of host-guest interactions in drugs@metal-organic frameworks: towards mimicking molecular recognition processes. *Mater. Horiz.* **2018**, *5*, 683–690.
- (57) Yoshioka, S.; Inokuma, Y.; Duplan, V.; Dubey, R.; Fujita, M. X-ray Structure Analysis of Ozonides by the Crystalline Sponge Method. *J. Am. Chem. Soc.* **2016**, *138*, 10140–10142.
- (58) Rissanen, K. Crystallography of encapsulated molecules. *Chem. Soc. Rev.* **2017**, *46*, 2638–2648.
- (59) Wada, N.; Kersten, R. D.; Iwai, T.; Lee, S.; Sakurai, F.; Kikuchi, T.; Fujita, D.; Fujita, M.; Weng, J.-K. Crystalline-Sponge-Based Structural Analysis of Crude Natural Product Extracts. *Angew. Chem. Int. Ed.* **2018**, *57*, 3671–3675.
- (60) Aguilera-Sigalat, J.; Bradshaw, D. Synthesis and applications of metal-organic framework-quantum dot (QD@MOF) composites. *Coord. Chem. Rev.* **2016**, *307*, 267–291.
- (61) Fortea-Pérez, F. R.; Mon, M.; Ferrando-Soria, J.; Boronat, M.; Leyva-Pérez, A.; Corma, A.; Herrera, J. M.; Osadchii, D.; Gascon, J.; Armentano, D.; Pardo, E. The MOF-driven synthesis of supported palladium clusters with catalytic activity for carbene-mediated chemistry. *Nat. Mater.* **2017**, *16*, 760–766.
- (62) Kitao, T.; Zhang, Y.; Kitagawa, S.; Wang, B.; Uemura, T. Hybridization of MOFs and polymers. *Chem Soc. Rev.* **2017**, *46*, 3108–3133.
- (63) Mon, M.; Rivero-Crespo, M. A.; Ferrando-Soria, J.; Vidal-Moya, A.; Boronat, M.; Leyva-Pérez, A.; Corma, A.; Hernández-Garrido, J. C.; López-Haro, M.; Calvino, J. J.; Ragazzon, G.; Credi, A.; Armentano, D.; Pardo, E. Synthesis of Densely Packaged, Ultrasmall Pt<sup>0</sup><sub>2</sub> Clusters within a Thioether-Functionalized MOF: Catalytic Activity in Industrial Reactions at Low Temperature. *Angew. Chem. Int. Ed.* **2018**, *57*, 6186–6191.
- (64) Li, B.; Zhang, Y.; Ma, D.; Ma, T.; Shi, Z.; Ma, S. Metal-Cation-Directed *de Novo* Assembly of a Functionalized Guest Molecule in the Nanospace of a Metal-Organic Framework. *J. Am. Chem. Soc.* **2014**, *136*, 1202–1205.
- (65) Qiu, X.; Zhong, W.; Bai, C.; Li, Y. Encapsulation of a Metal-Organic Polyhedral in the Pores of a Metal-Organic Framework. *J. Am. Chem. Soc.* **2016**, *138*, 1138–1141.
- (66) Cohen, S. The Postsynthetic Renaissance in Porous Solids. *J. Am. Chem. Soc.* **2017**, *139*, 2855–2863.
- (67) Islamoglu, T.; Goswami, S.; Li, Z.; Howarth, A. J.; Farha, O. K.; Hupp, J. T. Postsynthetic Tuning of Metal-Organic Frameworks for Targeted Applications. *Acc. Chem. Res.* **2017**, *50*, 805–813.
- (68) Zhang, L.; Yuan, S.; Feng, L.; Guo, B.; Qin, J.-S.; Xu, B.; Lollar, C.; Sun, D.; Zhou, H.-C. Pore-Environment Engineering with Multiple Metal sites in Rare-Earth Porphyrinic Metal-Organic Frameworks. *Angew. Chem. Int. Ed.* **2018**, *57*, 5095–5099.
- (69) Zhang, X.; Frey, B. L.; Chen, Y.-S.; Zhang, J. Topology-guided Stepwise Insertion of Three Secondary Linkers on Zirconium Metal-Organic Frameworks. *J. Am. Chem. Soc.* **2018**, *140*, 7710–7715.
- (70) Martinez, C.; Muñoz, K. Defined Palladium–Phthalimidato Catalysts for Improved Oxidative Amination. *Chem.-Eur. J.* **2016**, *22*, 7367–7370.
- (71) Mon, M.; Ferrando-Soria, J.; Grancha, T.; Fortea-Pérez, F. R.; Gascon, J.; Leyva-Pérez, A.; Armentano, D.; Pardo, E. Selective gold recovery and catalysis in a highly flexible methionine-decorated metal-organic framework. *J. Am. Chem. Soc.* **2016**, *138*, 7864–7867.

- (72) Fujita, M.; Sasaki, O.; Mitsuhashi, T.; Fujita, T.; Yazaki, J.; Yamaguchi, K.; Ogura, K. On the structure of transition-metal-linked molecular squares. *Chem. Commun.* **1996**, *0*, 1535–1536.
- (73) Varnholt, B.; Oulevey, P.; Lubert, S.; Kumara, C.; Dass, A.; Bürgi, T. Structural Information on the Au–S Interface of Thiolate-Protected Gold Clusters: A Raman Spectroscopy Study. *J. Phys. Chem. C* **2014**, *118*, 9604–9611.
- (74) Gao, S.; Huang, Y.; Cao, M.; Liu, T.-f.; Cao, R. The fabrication of palladium–pyridyl complex multilayers and their application as a catalyst for the Heck reaction. *J. Mater. Chem.* **2011**, *21*, 16467–16472.
- (75) Huynh, W. U.; Dittmer, J. J.; Alivisatos, A. P. Hybrid Nanorod-Polymer Solar Cells. *Science* **2002**, *295*, 2425–2427.
- (76) Adamo, C.; Amatore, C.; Ciofini, I.; Jutand, A.; Lakmini, H. Mechanism of the Pd-Catalyzed Homocoupling of Arylboronic Acids: Key Involvement of a Pd Peroxo Complex. *J. Am. Chem. Soc.* **2006**, *128*, 6829–6836.
- (77) Steinhoff, B. A.; Guzei, I. A.; Stahl, S. S. Mechanistic Characterization of Aerobic Alcohol Oxidation Catalyzed by Pd(OAc)<sub>2</sub>/Pyridine Including Identification of the Catalyst Resting State and the Origin of Nonlinear [Catalyst] Dependence. *J. Am. Chem. Soc.* **2004**, *126*, 11268–11278.
- (78) Hull, K. L.; Sanford, M. S. Mechanism of Benzoquinone-Promoted Palladium-Catalyzed Oxidative Cross-Coupling Reactions. *J. Am. Chem. Soc.* **2009**, *131*, 9651–9653.
- (79) Iwasawa, T.; Tokunaga, M.; Obora, Y.; Tsuji, Y. Homogeneous Palladium Catalyst Suppressing Pd Black Formation in Air Oxidation of Alcohols. *J. Am. Chem. Soc.* **2004**, *126*, 6554–6555.
- (80) Leyva-Pérez, A.; Doménech-Carbó, A.; Corma, A. Unique distal size selectivity with a digold catalyst during alkyne homocoupling. *Nat. Commun.* **2015**, *6*, 6703.
- (81) White, P. B.; Jaworski, J. N.; Zhu, G. H.; Stahl, S. S. Diazafluorenone-Promoted Oxidation Catalysis: Insights into the Role of Bidentate Ligands in Pd-Catalyzed Aerobic Aza-Wacker Reactions. *ACS Catal.* **2016**, *6*, 3340–3348.
- (82) Toledo, A.; Funes, I.; Maseras, F.; Carmen Albeniz, A. Palladium-Catalyzed Aerobic Homocoupling of Alkynes: Full Mechanistic Characterization of a More Complex Oxidase-type Behavior. *ACS Catal.* **2018**, *8*, 7495–7506.
- (83) Natte, K.; Chen, J.; Neumann, H.; Beller, M.; Wu, X. Palladium-catalyzed oxidative carbonylative coupling of arylboronic acids with terminal alkynes to alkynones. *Org. Biomol. Chem.* **2014**, *12*, 5590–5593.
- (84) Devarajan, N.; Karthik, M.; Suresh, P. Copper catalyzed oxidative homocoupling of terminal alkynes to 1,3-diyne: a Cu<sub>3</sub>(BTC)<sub>2</sub> MOF as an efficient and ligand free catalyst for Glaser–Hay coupling. *Org. Biomol. Chem.* **2017**, *15*, 9191–9199.
- (85) Zhou, Z.; Liu, M.; Wu, X.; Yu, H.; Xu, G.; Xie, Y. Amine-bridged bis(phenol) ligands for efficient Pd-catalyzed aqueous C–C coupling reactions. *Appl. Organometal. Chem.* **2013**, *27*, 562–569.



## Supplementary Information

# Self-Assembly of Catalytically-Active Supramolecular Coordination Compounds within Metal-Organic Frameworks

Rosa Adam<sup>1,†</sup> Marta Mon,<sup>2,†</sup> Rossella Greco,<sup>1</sup> Lucas H. G. Kalinke,<sup>2</sup> Alejandro Vidal-Moya,<sup>1</sup> Antonio Fernandez,<sup>3\*</sup> Richard E. P. Winpenny,<sup>4</sup> Antonio Doménech–Carbó,<sup>5</sup> Antonio Leyva–Pérez<sup>1\*</sup>, Donatella Armentano<sup>6\*</sup>, Emilio Pardo<sup>2\*</sup> and Jesús Ferrando-Soria<sup>2\*</sup>

<sup>1</sup>Dr. R. Adam, R. Greco, Dr. A. Vidal-Moya, Dr. A. Leyva–Pérez.  
Instituto de Tecnología Química (UPV–CSIC). Universidad Politècnica de València–Consejo Superior de Investigaciones Científicas. Avda. de los Naranjos s/n.  
46022, València, Spain.  
E-mail: anleyva@itq.upv.es

<sup>2</sup>M. Mon, L. H. G. Kalinke, Dr. E. Pardo, Dr. J. Ferrando-Soria  
Departamento de Química Inorgánica, Instituto de Ciencia Molecular (ICMOL). Universitat de València Catedrático Jose Beltrán Martínez, 2.  
46980, Paterna (Valencia), Spain.  
E-mail: jesus.ferrando@uv.es; emilio.pardo@uv.es

<sup>3</sup>Dr. A. Fernandez.  
Chemistry Department, Sir David Davies Building, Loughborough University.  
Loughborough LE11 3TU, United Kingdom.  
E-mail: a.fernandez-mato@lboro.ac.uk

<sup>4</sup>Prof. R. E. P. Winpenny.  
School of Chemistry and Photon Science Institute, The University of Manchester, Oxford Road.  
M13 9PL, Manchester, United Kingdom.

<sup>5</sup>Prof. A. Doménech–Carbó.  
Departamento de Química Analítica. Universitat de València. Dr. Moliner, 50.  
46100, Burjassot (València), Spain.

<sup>6</sup>Prof. D. Armentano.  
Dipartimento di Chimica e Tecnologie Chimiche. Università della Calabria. Via Pietro Bucci, 12c.  
87030, Rende (Cosenza), Italy.  
E-mail: donatella.armentano@unical.it

<sup>†</sup>These authors contributed equally to this work

**Supplementary Methods**

<b><i>Materials</i></b>	S1
<b><i>Preparation of compounds</i></b>	S1
Organic ligand L <sub>3</sub>	S1
[Pd <sup>II</sup> <sub>2</sub> (μ-OH) <sub>2</sub> (NH <sub>3</sub> ) <sub>4</sub> ] <sub>0.5</sub> [Pd <sup>II</sup> <sub>8</sub> (μ-OH) <sub>8</sub> (NH <sub>3</sub> ) <sub>8</sub> (L <sub>1</sub> ) <sub>4</sub> ] <sub>0.125</sub> {Ni <sup>II</sup> <sub>4</sub> [Cu <sup>II</sup> <sub>2</sub> (Me <sub>3</sub> mpba) <sub>2</sub> ] <sub>3</sub> } · 43H <sub>2</sub> O ( <b>2</b> )	S1
[Pd <sup>II</sup> <sub>16</sub> (H <sub>2</sub> O) <sub>8</sub> (NH <sub>3</sub> ) <sub>24</sub> (μ-OH) <sub>4</sub> (H <sub>2</sub> O) <sub>24</sub> (L <sub>2</sub> )] <sub>0.125</sub> {Ni <sup>II</sup> <sub>4</sub> [Cu <sup>II</sup> <sub>2</sub> (Me <sub>3</sub> mpba) <sub>2</sub> ] <sub>3</sub> } · 30H <sub>2</sub> O ( <b>3</b> )	S2
[Au <sup>III</sup> <sub>2</sub> (μ-OH) <sub>2</sub> (OH) <sub>4</sub> ] <sub>0.5</sub> [Au <sup>III</sup> <sub>2</sub> Cl <sub>6</sub> Pd <sup>II</sup> <sub>2</sub> (NH <sub>3</sub> ) <sub>6</sub> (L <sub>3</sub> ) <sub>2</sub> ] <sub>0.5</sub> [Pd <sup>II</sup> <sub>2</sub> (μ-OH) <sub>2</sub> (NH <sub>3</sub> ) <sub>6</sub> ] <sub>0.5</sub> {Ni <sup>II</sup> <sub>4</sub> [Cu <sup>II</sup> <sub>2</sub> (Me <sub>3</sub> mpba) <sub>2</sub> ] <sub>3</sub> } · 37H <sub>2</sub> O ( <b>4</b> )	S2
Table S1	S3
<b><i>X-Ray crystallographic data collection and structure refinement</i></b>	S3
<b><i>Structural details and in-depth analysis of X-ray data</i></b>	S6
Table S2 (Summary of crystallographic data for <b>2–4</b> )	S9
Figure S1 (View of crystal structures of <b>2</b> and <b>3</b> )	S10
Figure S2 (Perspective views of <b>2</b> )	S11
Figure S3 (A portion of crystal structures of <b>2</b> )	S12
Figure S4 (Perspective views of a portion of a pore of <b>2</b> )	S13
Figure S5 (Further details of crystal structure of <b>2</b> )	S14
Figure S6 (A portion of crystal structures of <b>3</b> )	S15
Figure S7 (Crystal structure of Pd <sup>II</sup> <sub>16</sub> SCCs in <b>3</b> )	S16
Figure S8 (View of crystal structures of <b>4</b> )	S17
Figure S9 (Details of crystal structure of <b>4</b> )	S18
Figure S10 (Perspective view of crystal structure of <b>4</b> )	S19
<b><i>Physical techniques</i></b>	S20
Figure S11 (PXRD patterns)	S22
Figure S12 (PXRD patterns after catalysis)	S23
Figure S13 (TGA analyses)	S24
Figure S14 (N <sub>2</sub> isotherms)	S25
Figure S15 (MAS-solid <sup>13</sup> C NMR spectrum)	S26

Figure S16 (DR UV-vis)	S27
Figure S17 (FT-IR spectroscopy)	S28
Figure S18 (Raman spectroscopy)	S29
Figure S19 (XPS)	S30
<b><i>Catalytic experiments</i></b>	S31
General procedures	S31
Characterization of isolated compounds	S33
NMR copies of isolated compounds	S35
Table S3	S45
Table S4	S46
Table S5	S47
Table S6	S48
Figure S20 (Schematic representation and <sup>1</sup> H NMR spectrum of Pd <sub>4</sub> (L <sub>1</sub> ) <sub>4</sub> )	S49
Figure S21 (DR-UV-Vis spectra of <b>2</b> and <b>3</b> before and after catalysis)	S50
Figure S22 (Catalytic results for <b>5c-f</b> )	S51
Figure S23 (Initial rates vs [reagents] for <b>2</b> )	S52
Figure S24 (Initial rates vs [reagents] for <b>3</b> )	S53
Figure S25 (Initial rates vs [reagents] for Pd <sub>4</sub> (L <sub>1</sub> ) <sub>4</sub> )	S54
Figure S26 (Initial rates vs [(Pd <sub>2</sub> )])	S55
Figure S27 (Initial rates vs [Pd <sub>4</sub> (L <sub>1</sub> ) <sub>4</sub> ])	S56
Figure S28 ( <sup>1</sup> H NMR spectra for homocoupling of <b>5a</b> by Pd <sub>4</sub> (L <sub>1</sub> ) <sub>4</sub> )	S57
Figure S29 (Initial rates vs [L <sub>1</sub> ] and [eda] for Pd <sub>4</sub> (L <sub>1</sub> ) <sub>4</sub> )	S58
Figure S30 (Cyclic Voltammograms)	S59
Figure S31 (Cyclic Voltammograms)	S60
Table S7	S61
Table S8	S62
Figure S32 (Catalytic results for homocoupling of <b>8b-d</b> by <b>4</b> )	S63
Figure S33 (Catalytic results for coupling of <b>8a</b> and <b>8f-h</b> by <b>4</b> )	S64
Figure S34 (Initial rates vs [reagents] for <b>4</b> )	S65

Figure S35 (Yield-time plot for <b>8a</b> homocoupling by <b>4</b> )	S66
Figure S36 (Yield-time plot for <b>8a</b> and <b>8a-d</b> homocoupling by <b>4</b> )	S67
Figure S37 (Initial rates vs [reagents] for Pd <sub>4</sub> (L <sub>1</sub> ) <sub>4</sub> )	S68
Figure S38 (Yield-time plot for <b>8a</b> homocoupling by Pd <sub>4</sub> (L <sub>1</sub> ) <sub>4</sub> )	S69
Figure S39 (Yield-time plot for <b>8a</b> and <b>8a-d</b> homocoupling by Pd <sub>4</sub> (L <sub>1</sub> ) <sub>4</sub> )	S70
Figure S40 ( <sup>1</sup> H NMR spectrum for homocoupling of <b>8a</b> by Pd <sub>4</sub> (L <sub>1</sub> ) <sub>4</sub> )	S71
Figure S41 (Catalytic results for cross-coupling by <b>4</b> )	S72
Figure S42 (Homocoupling of <b>8a</b> in flow)	S73
<i>Supplementary References</i>	S74

## Supplementary Methods

**Materials.** Unless stated otherwise, all chemicals were of reagent grade quality. They were purchased from commercial sources and used as received. 1,2-di(pyridin-4-yl)ethyne ( $L_1$ ),<sup>1</sup> methyl 3,5-bis(pyridin-4-ylethynyl)benzoate ( $L_2$ ),<sup>2</sup>  $\{[\text{Pd}^{\text{II}}(\text{en})(L_1)]_4(\text{NO}_3)_8\}$  ( $\text{Pd}^{\text{II}}_4(L_1)_4$ )<sup>3</sup> and  $[\text{Pd}^{\text{II}}(\text{NH}_3)_4][\text{Pd}^{\text{II}}_2(\mu\text{-H}_2\text{O})(\text{NH}_3)_6]_{0.5}\{\text{Ni}^{\text{II}}_4[\text{Cu}^{\text{II}}_2(\text{Me}_3\text{mpba})_2]_3\} \cdot 52\text{H}_2\text{O}$  (**1**)<sup>4</sup> were prepared according to literature procedure. Dry 1,4-dioxane was purchased from Acros Organics, and other anhydrous solvents were obtained from a resin-exchanger apparatus. Column chromatography was carried out using Silica 60 A (particle size 35-70  $\mu\text{m}$ , Fisher, UK) as the stationary phase, and TLC was performed on pre-coated silica gel plates (0.25 mm thick, 60 F<sub>254</sub>, Merck, Germany) and observed under UV light.

**4,4'-(2-(2-(methylthio)ethoxy)-1,3-phenylene)bis(ethyne-2,1-diyl)dipyridine ( $L_3$ ).** 1,3-dibromo-2-(2-methylsulfonylethoxy)benzene: To a solution of 2,6-dibromophenol (1 g, 3.98 mmol) in 40 mL of acetonitrile,  $\text{K}_2\text{CO}_3$  (1.64 g, 11.9 mmol) was added and the reaction mixture was refluxed for 1 h. After cooling down to room temperature, 1-bromo-2-methylsulfonylethane (0.61 g, 3.98 mmol) in 10 mL of acetonitrile was added and the reaction mixture was refluxed for 6 h. The mixture was cooled down, filtered and the volatiles were removed by rotatory evaporation. The solid obtained was re-dissolved in chloroform, washed with water and the organic phase was separated, dried and concentrated using rotatory evaporation. The obtained solid was used without any further purification for the next synthetic step. Yield: 85 % (1.02 g). ESI-MS (sample dissolved in MeOH, run in MeOH):  $m/z = 310$   $[\text{M}+\text{H}]^+$ . <sup>1</sup>H-NMR (400 MHz, 293K,  $\text{CDCl}_3$ ):  $\delta = 7.56$  (d,  $J = 8\text{Hz}$ , 2H), 6.82 (t,  $J = 8\text{Hz}$ , 1H), 4.23 (t,  $J = 6.8\text{Hz}$ , 2H), 2.91 (t,  $J = 6.8\text{Hz}$ , 2H), 2.16 (s, 3H).

A mixture of 1,3-dibromo-2-(2-methylsulfonylethoxy)benzene (1.02 g, 3.3 mmol), 4-ethynylpyridine hydrochloride (0.15 g, 1.37 mmol), copper(I) iodide (40 mg, 0.2 mmol) and bis(benzonitrile)palladium(II) dichloride (80 mg, 0.2 mmol) were added to a 100 mL round bottom flask. After several cycles of pumped under vacuum and refilled with argon, degassed anhydrous 1,4-dioxane (50 mL), diisopropylamine (3.4 mL, 4.8 mmol) and tri(*t*-butyl)phosphine (0.5 g, 2.47 mmol) were added through a canula and the dark green suspension was stirred at 50 °C for 20 hours. After cooling to room temperature, the dark mixture was filtered, and the solvent removed under reduced pressure. The resulting residue was purified by column chromatography using dichloromethane as first eluent and then a mixture of 1:1 dichloromethane:ethyl acetate was used obtaining  $L_3$  as pure product (0.93 g, 80 %). ESI-MS (sample dissolved in MeOH, run in MeOH):  $m/z = 355$   $[\text{M}+\text{H}]^+$ . <sup>1</sup>H NMR (400 MHz, 293K,  $\text{CDCl}_3$ ):  $\delta = 2.12$  (s, 3H), 2.92 (t,  $J = 6.8\text{Hz}$ , 2H), 4.52 (t,  $J = 6.8\text{Hz}$ , 2H), 7.16 (t,  $J = 7.7\text{Hz}$ , 1H), 7.42 (d,  $J = 6\text{Hz}$ , 4H), 7.52 (d,  $J = 7.7\text{Hz}$ , 2H), 8.62 (d,  $J = 6\text{Hz}$ , 4H). <sup>13</sup>C NMR (75 MHz, 293K,  $\text{CDCl}_3$ ):  $\delta = 52.71$ ; 87.64; 90.55; 123.6; 131.13; 132.6; 138.6; 149.12; 152.3; 165.5.

$[\text{Pd}^{\text{II}}_2(\mu\text{-OH})_2(\text{NH}_3)_4]_{0.5}[\text{Pd}^{\text{II}}_8(\mu\text{-OH})_8(\text{NH}_3)_8(L_1)_4]_{0.125}\{\text{Ni}^{\text{II}}_4[\text{Cu}^{\text{II}}_2(\text{Me}_3\text{mpba})_2]_3\} \cdot 43\text{H}_2\text{O}$  (**2**).

Well-formed deep green prisms of **2**, which were suitable for X-ray diffraction, were obtained by immersing crystals of **1** (ca. 36 mg, 0.010 mmol) in hot (50 °C) acetonitrile/water (2:1) solutions of  $L_1$  (5 mL, 10 mM) for one week. Then, the supernatant solution was removed, and the crystals were washed with an acetonitrile solution (5 x 10 mL), isolated by filtration on paper and air-dried.

Alternatively, large scale syntheses of **2**, were also carried out by using the same synthetic procedure but with stirring and with greater amounts of both, a powder sample of compound **1** (2 g, 0.55 mmol) and L<sub>1</sub> (50 mL, 55 mM), with the same successful results. Finally, the product was collected by filtration, washed with an acetonitrile solution and air-dried. Elemental analysis [% calcd., % found for Cu<sub>6</sub>Ni<sub>4</sub>Pd<sub>2</sub>C<sub>84</sub>H<sub>163</sub>N<sub>16</sub>O<sub>81</sub> (3522.17)]: C, 28.65; H, 4.67; N, 6.36%. Found: C, 28.75; H, 4.72; N, 6.31%. IR (KBr):  $\nu = 1603 \text{ cm}^{-1}$  (C=O).

$[\text{Pd}^{\text{II}}_{16}(\text{H}_2\text{O})_8(\text{NH}_3)_{24}(\mu\text{-OH}_2)_4(\text{H}_2\text{O})_{24}(\text{L}_2)]_{0.125}\{\text{Ni}^{\text{II}}_4[\text{Cu}^{\text{II}}_2(\text{Me}_3\text{mpba})_2]_3\} \cdot 30\text{H}_2\text{O}$  (**3**). The compound **3** was prepared by an analogous procedure to that for **2** by using L<sub>2</sub> as precursor instead of L<sub>1</sub>. Elemental analysis [% calcd., % found for Cu<sub>6</sub>Ni<sub>4</sub>Pd<sub>2</sub>C<sub>80.75</sub>H<sub>139.75</sub>N<sub>15.25</sub>O<sub>70.75</sub> (3285.2)]: C, 29.50; H, 4.25; N, 6.50%. Found: C, 29.39; H, 4.08; N, 6.23%. IR (KBr):  $\nu = 1601 \text{ cm}^{-1}$  (C=O).

$[\text{Au}^{\text{III}}_2(\mu\text{-OH})_2(\text{OH})_4]_{0.5}[\text{Au}^{\text{III}}_2\text{Cl}_6\text{Pd}^{\text{II}}_2(\text{NH}_3)_6(\text{L}_3)_2]_{0.5}[\text{Pd}^{\text{II}}_2(\mu\text{-OH}_2)(\text{NH}_3)_6]_{0.5}\{\text{Ni}^{\text{II}}_4[\text{Cu}^{\text{II}}_2(\text{Me}_3\text{mpba})_2]_3\} \cdot 37\text{H}_2\text{O}$  (**4**). Well-shaped deep green prisms of **4**, were obtained by immersing crystals of **1** (*ca.* 36 mg, 0.010 mmol) in hot (50 °C) acetonitrile/water (2:1) solutions of L<sub>3</sub> (5 mL, 10 mM) for one week. After washing the crystals with additional acetonitrile (5 x 10 mL), they were immersed in a fresh H<sub>2</sub>O/CH<sub>3</sub>OH (1:1) solution. The solution was exchanged every three hours five times. Then, the crystals were treated in a H<sub>2</sub>O/CH<sub>3</sub>OH (1:1) solution of AuCl<sub>3</sub> (3.0 mg, 0.010 mmol) for 12 hours. The process was repeated five more times to ensure that the maximum loading of possible gold atoms was achieved. This was monitored by ICP-MS and SEM/EDX. The gold-metallated crystals had the same size and shape as those of the starting SCC@MOF, ruling out a possible dissolution-recrystallization mechanism for this system and strongly suggesting a solid-state process in the formation of the heterobimetallic SCC@MOF. The crystals were washed with a H<sub>2</sub>O/CH<sub>3</sub>OH (1:1) solution (5 x 10 mL), isolated by filtration on paper and air-dried.

Alternatively, large scale syntheses of **4**, were also carried out by using the same consecutive step-by-step synthetic procedure but with stirring and with greater amounts of precursors, a powder sample of compound **1** (2 g, 0.55 mmol), L<sub>3</sub> (50 mL, 55 mM) and AuCl<sub>3</sub> (0.17 g, 0.55 mmol) with the same successful results. The metalation of the preformed SCC@MOF was repeated five times. This was monitored by ICP-MS and SEM/EDX. Finally, the product was collected by filtration, washed with a H<sub>2</sub>O/CH<sub>3</sub>OH (1:1) solution and air-dried. Elemental analysis [% calcd., % found for Cu<sub>6</sub>Ni<sub>4</sub>Pd<sub>2</sub>Au<sub>2</sub>C<sub>101</sub>H<sub>174</sub>N<sub>20</sub>O<sub>77.5</sub>Cl<sub>3</sub>S (4269.8)]: C, 28.39; H, 4.08; S, 0.75; N, 6.56%. Found: C, 28.85; H, 4.33; S, 0.90; N, 6.80%. IR (KBr):  $\nu = 1603 \text{ cm}^{-1}$  (C=O).

**Table S1.** Selected data from the ICP–MS<sup>a</sup> and SEM/EDX<sup>b</sup> analyses for **1–4**.

<b>Compound 1</b>				
<b>Metal</b>	<i>% mass<sup>a</sup></i>	<i>Metal stoichiometry<sup>a</sup></i>	<i>% mass<sup>b</sup></i>	<i>Metal stoichiometry<sup>b</sup></i>
<b>Cu</b>	10.571	6.00	10.43	5.92
<b>Ni</b>	6.518	4.01	6.47	3.98
<b>Pd</b>	5.892	1.99	5.77	1.95
<b>Compound 2</b>				
<b>Metal</b>	<i>% mass<sup>a</sup></i>	<i>Metal stoichiometry<sup>a</sup></i>	<i>% mass<sup>b</sup></i>	<i>Metal stoichiometry<sup>b</sup></i>
<b>Cu</b>	10.661	5.98	10.68	5.99
<b>Ni</b>	6.584	4.00	6.63	4.03
<b>Pd</b>	5.922	1.98	5.87	1.97
<b>Compound 3</b>				
<b>Metal</b>	<i>% mass<sup>a</sup></i>	<i>Metal stoichiometry<sup>a</sup></i>	<i>% mass<sup>b</sup></i>	<i>Metal stoichiometry<sup>b</sup></i>
<b>Cu</b>	11.603	6.00	11.68	6.03
<b>Ni</b>	7.134	3.99	7.23	4.05
<b>Pd</b>	6.493	2.00	6.54	2.02
<b>Compound 4</b>				
<b>Metal</b>	<i>% mass<sup>a</sup></i>	<i>Metal stoichiometry<sup>a</sup></i>	<i>% mass<sup>b</sup></i>	<i>Metal stoichiometry<sup>b</sup></i>
<b>Cu</b>	8.932	6.00	8.98	6.03
<b>Ni</b>	5.573	4.05	5.56	4.04
<b>Pd</b>	4.935	1.98	4.99	2.00
<b>Au</b>	9.159	1.99	9.25	2.00

Solid samples were digested with 0.5 mL of HNO<sub>3</sub> 69% at 60°C for 4 hours followed by the addition of 0.5 mL of HCl 37% and digestion 80°C for 1 hour. Metal stoichiometric is given according to formula unit.

**X-Ray crystallographic data collection and structure refinement.** Crystals of **2–4** with 0.08 x 0.07 x 0.07, 0.14 x 0.12 x 0.12, and 0.06 x 0.05 x 0.05 as dimensions were selected and mounted on a MiTeGen MicroMount in Paratone oil and very quickly placed on a liquid helium (**2**) or nitrogen (**3–4**) stream cooled at 30 K for **2** and **4** and 90 K for **3**, to avoid the possible degradation upon dehydration. Diffraction data for **2** and **4** were collected using synchrotron radiation at I19 beamline of the Diamond Light Source at  $\lambda = 0.6889 \text{ \AA}$ , whereas for **3** on a Bruker-Nonius X8APEXII CCD area detector diffractometer using graphite-monochromated Mo-K $\alpha$  radiation ( $\lambda = 0.71073 \text{ \AA}$ ). The data were processed through xia2<sup>5</sup> (**2** and **4**), or SAINT<sup>6</sup> reduction and SADABS<sup>7</sup> multi-scan absorption (**3**) software. The structures were solved with the SHELXS structure solution program, using the Patterson method. The model was

refined with version 2013/4 or 2018/3 (for sample **3**) of SHELXL against  $F^2$  on all data by full-matrix least squares.<sup>8</sup>

The highly robustness and crystallinity of these materials, together with the application of cutting-edge X-ray crystallography technique allowed the complete resolution of the crystal structure of **2**. Even for **3** hybrid material it was possible to refine a structural model which gives an in-depth insight about the most probably organization of entities self-assembled within pores. Crystals were suitable for X-ray diffraction, even though more than one crystal-to-crystal transformation have been performed to synthesise them (see synthetic experimental section). However, for these reasons, it is reasonable to observe a diffraction pattern sometimes affected by unavoidable internal imperfections of the crystals. For sample **4**, the quality of the SCXRD data was not good enough for the complete structural resolution of **4**. However, the crystallographic positions of the metal ions, building up the SCCs, and some ligand's fragments could be determined from Fourier maps, giving precious insights about the most probable structure of assemblies growth in the confined space of a metal organic framework.

It is worth to note that the presented structural characterization goes one step further than what have been observed in nanospace so far. It allows, for the first-time, direct visualization of the *in-situ* heterogeneous self-assembled SCCs within MOF channels. For that reasons, it is worth to underline that structural parameters such as thermal factors are sometimes high due to disorder related to the high degrees of freedom in self-assembly of *bricks* in nanospace (see explanation below).

In all samples (**2–4**) all non-hydrogen atoms of the net were refined anisotropically. It is not the same for some highly dynamically disordered lattice water molecules atoms and atoms of *in-situ* assembled SCCs. All the hydrogen atoms of the net together with hydrogen atoms on the ligand  $L_1$  in **2**, were set in calculated positions and refined isotropically using the riding model. Hydrogen atoms on the bridging water molecules, terminal ammonia groups of Pd(II) complexes and of the lattice water molecules –found from Fourier maps– were neither found nor calculated in all three samples. The SCCs build up inside the channels are expected to be severely disordered, as a direct consequence of their high thermal motion and also statistical disorder. This is related to both symmetry of the ligands  $L_1–L_3$  –that does not fit the symmetries of the space group in which hosting matrix crystallizes– and size and shape of the final assemblies –that govern the degree of freedom of the hybrid systems. While in **2** the size and shape of  $Pd^{II}_8$  square polygons, and  $Pd^{II}_2$  dimers, permit them to reside at positions perfectly stabilized by supramolecular interactions with the net (see Figures S4 and S5) –ensuring an efficient anchoring of them in confined space, with a consequent less thermal disorder–, in **3** the different symmetry of the ligand  $L_2$  makes  $Pd^{II}_2L_2$  and  $Pd^{II}_2$  dimers less blocked by the hosting matrix, and thus, more disordered. Furthermore, the symmetry of Pd- $L_2$  assembly does not fit that of hosting framework space group, which imposes a mirror plane on oxygen atoms of carboxylate groups and results in statistical disorder of the final SCC. In fact, it is well known that a crystal structure is the *spatial average* of representing all molecules together with all their possible orientations averaged in the crystal *via* only one-unit cell. In all cases, as the present one, where obviously not all unit cells are identical and a variety of orientations are allowed, the description became even more challenging. Also, in **4**, the symmetry and chemical affinities of ligand  $L_3$  allows an arrangement of heterogeneous SCCs with conformation of the aromatic fragment pointing towards the centre of the biggest pores, and as consequence, severely disordered. Refinement of data collected at 30 K with

synchrotron radiation revealed no significant peaks of electron density attributable to aromatic side of L<sub>3</sub> in the channels, as it would be expected from their weak interaction due to thermal motion in a so large space. Where the interactions with the net increase, many local maxima were located in the observed structure factor Fourier maps, providing evidence of the localization of the SCC's fragments represented in Figure S9.

The occupancy factors of Pd and Au atoms have been refined in agreement with expected thermal factors, SEM and ICP-MS results [0.25 for both Pd1 ([Pd<sup>II</sup><sub>8</sub>(L<sub>1</sub>)<sub>4</sub>] square polygons population) and Pd2 (Pd<sup>II</sup><sub>2</sub> water bridged dimers population) in **2**, 0.25 for Pd1 (Pd<sup>II</sup><sub>2</sub>L<sub>2</sub> dimers population) and 0.25 for Pd2 (Pd<sup>II</sup><sub>2</sub> oxo-bridged dimers population) in **3**, whereas in **4** 0.25 for both Pd1 and Pd2 together with 0.25 for Au1 and Au2], as well as in agreement with their respectively asymmetric units and molecular cells contents. The occupancies of the ligands in the pores, have been defined by a combination of elemental (C,H,N,S) analyses, and thermal factors, and then often imposed as occupancy factors in structure refinement according to metal ions amount. We strongly believe that it is the more reliable way to accurately define loading, instead of taking into account merely thermal factors, which can be affected by a lot of issues above all severe disorder.

The use of some C-C, C-N, C-O and C-S bond lengths restraints of highly disordered atoms for both network and generated guest assemblies during the refinements in all crystal structures as well as Pd-N and Pd-O ones, has been reasonably imposed, as related to the expected and severe thermal motion, likely depending on the large size of the huge pores of the frameworks (DFIX, RIGU, SIMU, DELU and ISOR). All that is particularly marked in **3** and **4** (see discussion above). In summary, in all samples guest assemblies are severely disordered, especially for the fragments pointing towards the center of the pores where, undoubtedly, the degrees of freedom, related to diverse possible conformations, significantly increase. For that reasons in some cases we constrained even thermal factors. Moreover, in general for the two messy assemblies in **3** and **4**, NH<sub>3</sub> terminal molecules and some terminal fragments were not found from ΔF map.

In **2**, the oxygen atom O2H of bridging water exhibits positional disorder.

In **3**, as already reported, the whole [Pd<sup>II</sup><sub>16</sub>(H<sub>2</sub>O)<sub>8</sub>(NH<sub>3</sub>)<sub>24</sub>(μ-OH<sub>2</sub>)<sub>4</sub>(H<sub>2</sub>O)<sub>24</sub>(L<sub>2</sub>)] supramolecular assembly exhibits statistic disorder. In [Pd<sup>II</sup><sub>2</sub>(μ-OH<sub>2</sub>)<sub>4</sub>(H<sub>2</sub>O)<sub>6</sub>]<sup>4+</sup> dimers, not all waters have been found from ΔF maps.

In **4**, the overall aromatic fragment of the ligand L<sub>3</sub> were not found from Fourier maps (see Figure S4). In [Au<sup>III</sup><sub>2</sub>(μ-OH)<sub>2</sub>(OH)<sub>4</sub>] dimers, bridging water molecules O7W and O8W exhibit statistic disorder.

As a consequence of disorder, Alert A in the checkcif, also related to short intermolecular C...C of guests and net or equivalent positions generated by overlapping various geometry, are detected, but are unavoidable.

The solvent molecules were also highly disordered –some refined double positions are detected as Alerts A in the checkcif. Again, the quite large channels featured by the MOF likely account for that. However, even if not all ones have been detected by TGA analysis, they have been somehow modelled in all the crystal structures (Alert level B for **1**, related to mismatch in the ratio of given/expected molecular weight) **2–4**.

Overall the “Alert A” notifications found in the validation program CheckCIF are either related to intrinsic imperfections and disorder –as the presence of large outliers

in the data set, quite normal for crystals that suffered three post-synthetic steps—, or from short intermolecular contacts between water molecules and *in-situ* generated assemblies—which are unavoidable due to the expected severe disorder of both solvent and SCCs. The comments for the alerts are described in the CIFs using the validation reply form (vrf).

A summary of the crystallographic data and structure refinement for the three compounds is given in Table S1. CCDC reference numbers are 1892911, 1892912 and 1892914 for **2**, **3** and **4**, respectively.

The final geometrical calculations on free voids and the graphical manipulations were carried out with PLATON<sup>9</sup> implemented in WinGX,<sup>10</sup> and CRYSTAL MAKER<sup>11</sup> programs, respectively.

**Structural details and in-depth analysis of X-ray data.** As reported in the main text, the SCXRD data of **2–4** evidences that the 3D network remained crystalline during the MOF-templated *in-situ* heterogeneous self-assembled process. In **2** a well-solved structure of Pd<sup>II</sup><sub>8</sub> square metal-organic polygon mechanically-bonded to the MOF network was achieved (Figure 2, 3a left, 3b and Figures S1–S5). In contrast, the ligand counterpart from the SCCs guests in **3**, and markedly in **4**, were persistently disordered within the MOF host (Figures S1 and S6–S10). However, even in case of **4**, electron density maps and structural analyses clearly gave insights about the presence of [Au<sup>III</sup><sub>2</sub>(μ-OH)<sub>2</sub>(OH)<sub>4</sub>] dimers, [Au<sup>III</sup><sub>2</sub>Cl<sub>6</sub>Pd<sup>II</sup><sub>2</sub>(NH<sub>3</sub>)<sub>6</sub>(L<sub>3</sub>)<sub>2</sub>]<sup>4+</sup> heterobimetallic cationic assemblies and [Pd<sup>II</sup><sub>2</sub>(μ-OH<sub>2</sub>)(NH<sub>3</sub>)<sub>6</sub>]<sup>4+</sup> dimers within the 3D net channels (Figure S8–S10), whereby the L<sub>3</sub> ligands would possess a putative tripoidal geometry with detected thioether moieties acting as clamps to enlase gold(III) complexes. The anionic Ni<sup>II</sup><sub>4</sub>Cu<sup>II</sup><sub>6</sub> open-framework structure in **2–4** retains the known pillared square/octagonal layer architecture of **1**, where nickel(II) and copper(II) ions are located on the vertices and midpoints of the edges, respectively, together with Pd(II) cationic complexes homogeneously distributed within the pores, acting as a perfect platform to template SCCs self-assembly. It features three types of pores—a small almost square sized pores and two kinds of hydrophobic and hydrophilic octagonal pores with virtual diameters of *ca.* 0.4, 1.5 and 2.2 nm, respectively—propagating along the *c* axis and enfolding up to 56% of the total lattice volume (Figure 2, 3 and Figures S1–S10). Both, the biggest hydrophobic octagonal channels and the square smallest pores, accommodate Pd(II) (**2–3**) and Pd(II)/Au(III) (**4**) complexes as result of L<sub>1</sub>–L<sub>3</sub> binding to either mononuclear, [Pd<sup>II</sup>(NH<sub>3</sub>)<sub>4</sub>]<sup>2+</sup>, or dinuclear complexes of the type [Pd<sup>II</sup><sub>2</sub>(μ-O)(NH<sub>3</sub>)<sub>6</sub>]<sup>2+</sup> of **1** which can be self-assembled to give **2–4** (Figures 1–3 and Figures S1–S10). The arrangement of Pd<sup>2+</sup> SCCs in **2–3**, as well as Pd<sup>2+</sup> together with Au<sup>3+</sup> and Pd<sup>2+</sup>Au<sup>3+</sup> SCCs in **4**, confined into the channels and stabilized by mechanical-bonds with the MOF network, are strictly related to nature of the ligands (L) employed in terms of size, shape and imposed symmetry.

In **2**, half of the Pd<sup>2+</sup> ions from the mononuclear and dinuclear entities in **1** are self-assembled by ligand L<sub>1</sub> giving [Pd<sup>II</sup><sub>8</sub>(μ-OH<sub>2</sub>)<sub>8</sub>(NH<sub>3</sub>)<sub>8</sub>(L<sub>1</sub>)<sub>4</sub>]<sup>16+</sup> square polygons, with [Pd<sup>II</sup><sub>2</sub>(μ-OH<sub>2</sub>)<sub>2</sub>(NH<sub>3</sub>)<sub>2</sub>] dimers residing at the corners of the quadrangular SCC (Figures 2, 3a left, 3b and Figures S1–S5). Each Pd(II) exhibits regular square planar geometry, with Pd–N [2.02(2) and 2.09(2) Å for Pd–N<sub>L1</sub> and Pd–NH<sub>3</sub>, respectively] and Pd–OH<sub>2</sub> [1.99(2) and 2.05(2) Å] bond distances similar to those found in the literature.<sup>12–15</sup> The Pd(II) separations through H<sub>2</sub>O and L<sub>1</sub> bridges are 2.840(6) and 13.49(1) Å, respectively. *Free* [Pd<sup>II</sup><sub>2</sub>(μ-OH<sub>2</sub>)<sub>2</sub>(NH<sub>3</sub>)<sub>4</sub>]<sup>2+</sup> dimers are still present in smaller square pores, exhibiting Pd–NH<sub>3</sub> [2.00(1) and 2.02(1) Å] and Pd–OH<sub>2</sub> [2.039(9) and 2.19(1)

Å] bond distances in the expected ranges. Square polygons are regularly pillared along *c* crystallographic axes, with a Pd(II)⋯Pd(II) separation among adjacent polygons of 15.15(1) Å, being stabilized by mechanical-bonds with the walls of the net involving terminal NH<sub>3</sub> molecules and oxamate residues belonging to the net [H<sub>3</sub>N⋯O<sub>oxamate</sub> of 2.913(9) Å] (Figures S3 and S4). As for the [Pd<sup>II</sup><sub>8</sub>(μ-O H<sub>2</sub>)<sub>8</sub>(NH<sub>3</sub>)<sub>8</sub>(L<sub>1</sub>)<sub>4</sub>]<sup>16+</sup> squares, [Pd<sup>II</sup><sub>2</sub>(μ-OH<sub>2</sub>)<sub>2</sub>(NH<sub>3</sub>)<sub>4</sub>]<sup>2+</sup> dimers are perfectly *blocked* within pores by H-bonds established between ammonia ligands and oxamate moieties of the hosting matrix [H<sub>3</sub>N⋯O<sub>oxamate</sub> of 2.900(9) Å] (Figure S5). The synergic stabilizations ensured by hosting matrix strongly support the robustness of such assembled SCCs, with high activity in heterogeneous metal-based supramolecular catalysis (*vide infra*).

The different nature and symmetry of ligand L<sub>2</sub> imposes a totally different assembly of native [Pd<sup>II</sup>(NH<sub>3</sub>)<sub>4</sub>]<sup>2+</sup>, or dinuclear complexes of the type [Pd<sup>II</sup><sub>2</sub>(μ-O)(NH<sub>3</sub>)<sub>6</sub>]<sup>2+</sup> present in **1**. The substitution of ammonia by water and L<sub>2</sub> ligands, yields a [Pd<sup>II</sup><sub>16</sub>(H<sub>2</sub>O)<sub>8</sub>(NH<sub>3</sub>)<sub>24</sub>(μ-OH<sub>2</sub>)<sub>4</sub>(H<sub>2</sub>O)<sub>24</sub>(L<sub>2</sub>)] supramolecular assembly, where [Pd<sup>II</sup><sub>2</sub>(NH<sub>3</sub>)<sub>6</sub>(L<sub>2</sub>)] dimers are linked by strong hydrogen bonds, through the carboxylate group of L<sub>2</sub> and H<sub>2</sub>O molecules, to [Pd<sup>II</sup><sub>2</sub>(μ-OH<sub>2</sub>)<sub>4</sub>(H<sub>2</sub>O)<sub>6</sub>] dimers for which not all waters have been found from ΔF maps [O⋯O of 2.89(4) and 2.89(3) Å for -COO⋯O<sub>water</sub> and O<sub>water</sub>⋯O<sub>water</sub>, respectively] (Figures 3a right, 3c and Figures S6 and S7). These results definitely highlight how the interplay between hydrophilic channels and the resultant vastly solvated confined nanospace –in which water molecules are never innocent actors– is at the origin of [Pd<sup>II</sup><sub>16</sub>(H<sub>2</sub>O)<sub>8</sub>(NH<sub>3</sub>)<sub>24</sub>(μ-OH<sub>2</sub>)<sub>4</sub>(H<sub>2</sub>O)<sub>24</sub>(L<sub>2</sub>)]<sup>32+</sup> moieties stabilizations. Despite thermal and positional disorder detected for L<sub>2</sub> ligand – that clearly does not fit the space group of hosting matrix (see Supplementary Information and Figure S7)– has been possible to solve the crystal structure of SCC where Pd(II) ions exist in distorted square planar geometries with Pd-N in the [Pd<sup>II</sup><sub>2</sub>(NH<sub>3</sub>)<sub>6</sub>(L<sub>2</sub>)] dimers and Pd-OH<sub>2</sub> distances of the [Pd<sup>II</sup><sub>2</sub>(μ-OH<sub>2</sub>)<sub>4</sub>(H<sub>2</sub>O)<sub>6</sub>] moieties falling in the expected values [1.99(1) and 2.00(1) Å for Pd-N<sub>L2</sub> and Pd-NH<sub>3</sub>, respectively, and Pd-OH<sub>2</sub> of 2.05(3) and 2.47(3) Å].<sup>12–15</sup> The Pd(II)⋯Pd(II) separation within [Pd<sup>II</sup><sub>2</sub>(NH<sub>3</sub>)<sub>6</sub>(L<sub>2</sub>)] dimers is of 6.1 Å whereas 8.3 Å is the shortest Pd(II)⋯Pd(II) distance detected in Pd<sub>16</sub> assemblies. The strength of H-bonds observed in Pd<sub>16</sub> assembly of **3**, together with its stabilization by mechanical-bonds with the network, underpins the role of supramolecular interactions in *nanosolvated* space, which should be most likely able to preserve Pd<sub>16</sub> aggregates during catalysis as well.

The large accessible free voids even after SCCs assembly is calculated to be 50.8 and 47.9% of the total cell volume, for **2** (9823.1 Å<sup>3</sup> per Unit Cell Volume of 19325.0 Å<sup>3</sup>) and **3** (9007.2 Å<sup>3</sup> per Unit Cell Vol of 18795.0 Å<sup>3</sup>), respectively allow the guest to become more than an innocent bystander. That large pores ensure free access to reactant species.

Despite the impeccable resolution of the crystal structure achieved for SCCs in **2** and quite complete in **3**, the quality of the SCXRD data did not allow the same precision for the complete visualization of SCCs' crystal structure of **4**. However, many local maxima attributable to Pd<sup>2+</sup> and Au<sup>3+</sup> metal ions in the channels together with few peaks related to L<sub>3</sub> ligand's fragments were located in the observed structure factor Fourier maps, providing evidence of the localization of the SCCs (Figures S8–S10). Looking at their disposition, it is rationale to hypothesize a self-assembly of a half of native [Pd<sup>II</sup>(NH<sub>3</sub>)<sub>4</sub>]<sup>2+</sup>, or dinuclear complexes of the type [Pd<sup>II</sup><sub>2</sub>(μ-O)(NH<sub>3</sub>)<sub>6</sub>]<sup>2+</sup> present in **1**, which occurs first in a similar manner as observed in **2** producing [Pd<sup>II</sup><sub>2</sub>(NH<sub>3</sub>)<sub>6</sub>(L<sub>3</sub>)<sub>2</sub>] dimers (for which no peaks related to the aromatic moiety has been found from ΔF

maps) remaining in big hydrophobic pores with Pd(II) in square planar geometry [average Pd-N of 2.10(2) Å]. The Pd···Pd and N<sub>L3</sub>···N<sub>L3</sub> separations within dimers of 11.36 and 13.97(1) Å fit very-well with those found for complexes constructed with similar ligands (*ca.* 14 Å).<sup>12-14</sup> These dimers further grasp AuCl<sub>3</sub> complexes exploiting the high affinity for soft metal ions of the thioether moiety<sup>16</sup> featured by L<sub>3</sub>, generating, finally, self-assembled heterometallic SCCs of the type [Au<sup>III</sup><sub>2</sub>Cl<sub>6</sub>Pd<sup>II</sup><sub>2</sub>(NH<sub>3</sub>)<sub>6</sub>(L<sub>3</sub>)<sub>2</sub>] showing Pd···Au and Au···Au separations of 13.50(1) and 11.89(1) Å, respectively (Figure S9). Interestingly the found position of Au(III) ions, consistent with L<sub>3</sub> symmetry, is displaced towards the centre of the big pores, suggesting a high accessibility for reactants. Furthermore, the solved crystal structure clearly evidences either the thioether fragments [allowing to unveil the Au-S distance of 2.34(1) Å] or the persistent presence of MOF's stabilized [Pd<sup>II</sup><sub>2</sub>(μ-OH<sub>2</sub>)(NH<sub>3</sub>)<sub>6</sub>] dimers, again residing in the small square channels between hydrophobic and hydrophilic pores as observed for **3** [2.00(2) and 2.22(1) Å, for average Pd-NH<sub>3</sub> and Pd-OH<sub>2</sub>, respectively]. In addition, the crystal structure of **4** reveals [Au<sup>III</sup><sub>2</sub>(μ-OH)<sub>2</sub>(OH)<sub>4</sub>] dimers filling the small square pores featured by the MOF, with Au-O<sub>water</sub> bond lengths of 2.17(2), 2.00(2) and 2.32(5) Å and very short intradimer Au···Au separations of 2.20 Å in square planar geometry.

**Table S2.** Summary of crystallographic data for **2–4**.

Compound	<b>2</b>	<b>3</b>	<b>4</b>
Formula	C <sub>84</sub> H <sub>163</sub> Cu <sub>6</sub> N <sub>16</sub> Ni <sub>4</sub> O <sub>81</sub> Pd <sub>2</sub>	C <sub>80.75</sub> H <sub>139.75</sub> Cu <sub>6</sub> N <sub>15.25</sub> Ni <sub>4</sub> O <sub>70.75</sub> Pd <sub>2</sub>	C <sub>101</sub> H <sub>174</sub> Cu <sub>6</sub> N <sub>20</sub> Ni <sub>4</sub> O <sub>77.5</sub> SPd <sub>2</sub> Au <sub>2</sub> Cl <sub>3</sub>
<i>M</i> (g mol <sup>-1</sup> )	3522.17	3285.20	4269.80
$\lambda$ (Å)	0.6889	0.71073	0.6889
Crystal system	Tetragonal	Tetragonal	Tetragonal
Space group	<i>P4/mmm</i>	<i>P4/mmm</i>	<i>P4/mmm</i>
<i>a</i> (Å)	35.7158(2)	35.258(10)	35.725(2)
<i>c</i> (Å)	15.14950(10)	15.119(4)	15.2666(8)
<i>V</i> (Å <sup>3</sup> )	19325.0(3)	18795(12)	19485(2)
<i>Z</i>	4	4	4
$\rho_{\text{calc}}$ (g cm <sup>-3</sup> )	1.211	1.161	1.456
$\mu$ (mm <sup>-1</sup> )	1.125	1.313	2.506
<i>T</i> (K)	30(2)	90(2)	30(2)
$\theta$ range for data collection (°)	0.781 - 36.159	0.817 - 23.595	0.552 - 25.000
Completeness to $\theta = 23.0$	100	98.6	100
Completeness to $\theta = 25.0$	100	82	100
Measured reflections	427337	66503	244768
Unique reflections (Rint)	26486 (0.0579)	7708 (0.1218)	10377 (0.1736)
Observed reflections [ <i>I</i> > 2 $\sigma$ ( <i>I</i> )]	6413	3668	3377
Goof	1.036	1.175	1.911
<i>R</i> <sup>a</sup> [ <i>I</i> > 2 $\sigma$ ( <i>I</i> )] (all data)	0.1256 (0.2909)	0.1316 (0.2081)	0.3098 (0.4234)
<i>wR</i> <sup>b</sup> [ <i>I</i> > 2 $\sigma$ ( <i>I</i> )] (all data)	0.4038 (0.4428)	0.3549 (0.3857)	0.6579 (0.6865)
CCDC code	1892911	1892912	1892914

$$^a R = \sum(|F_o| - |F_c|) / \sum |F_o|, \quad ^b wR = [\sum w(|F_o| - |F_c|)^2 / \sum w |F_o|^2]^{1/2}.$$

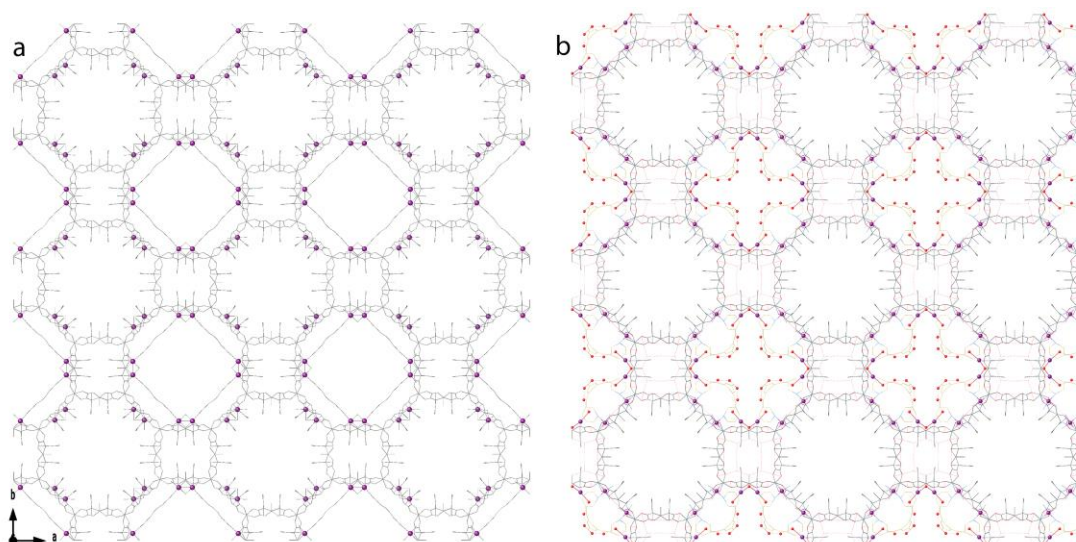


**Figure S1.** View along *c* crystallographic axis of crystal structures of **2** (a) and **3** (b) featuring channels filled by  $\{[\text{Pd}^{\text{II}}_2(\mu\text{-OH}_2)_2(\text{NH}_3)_4]\}^{4+}$  and  $[\text{Pd}^{\text{II}}_8(\mu\text{-OH}_2)_8(\text{NH}_3)_8(\text{L}_1)_4]^{16+}$  (**2**) or  $[\text{Pd}^{\text{II}}_{16}(\text{H}_2\text{O})_8(\text{NH}_3)_{24}(\mu\text{-OH}_2)_4(\text{H}_2\text{O})_{24}(\text{L}_2)]^{32+}$  SCCs (**3**). Lattice water molecules and hydrogen atoms have been omitted for clarity. Color scheme: palladium, violet sphere; oxygen, red spheres, ligand  $\text{L}_2$  in **3**, yellow sticks, ligands atoms and metal ions of the whole net have been depicted as grey sticks.

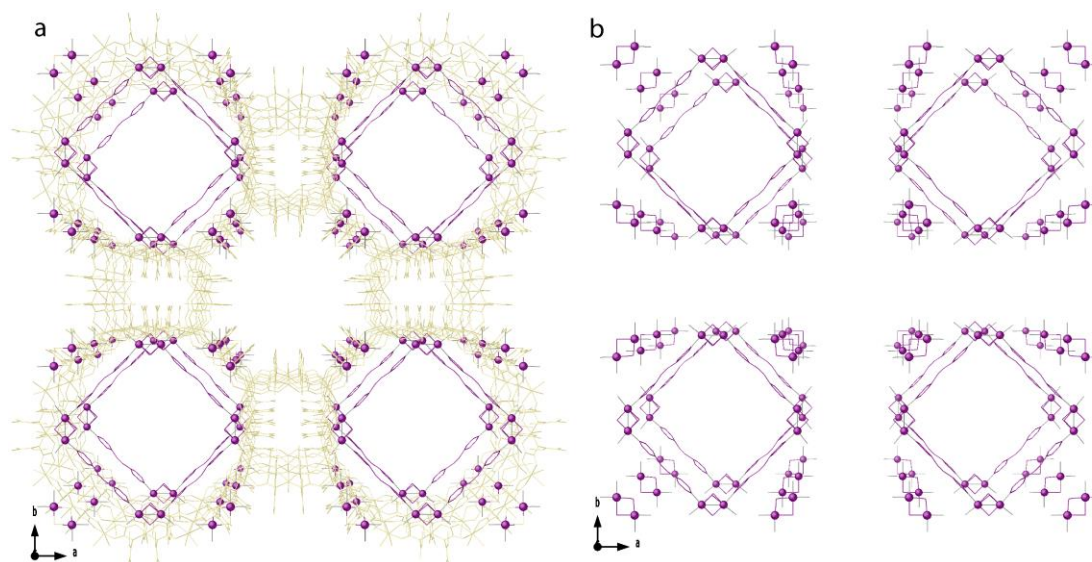


**Figure S2.** Perspective views showing details with and without the whole net (a and b, respectively) of distribution of Pd<sup>II</sup><sub>8</sub> squares SCCs filling hydrophilic channels and Pd<sup>II</sup><sub>2</sub> dimers residing in the boundaries within hydrophobic and hydrophilic pores in **2**. Color scheme: palladium, violet sphere; ligand, violet sticks, ligands atoms and metal ions of the whole net have been depicted as yellow sticks.

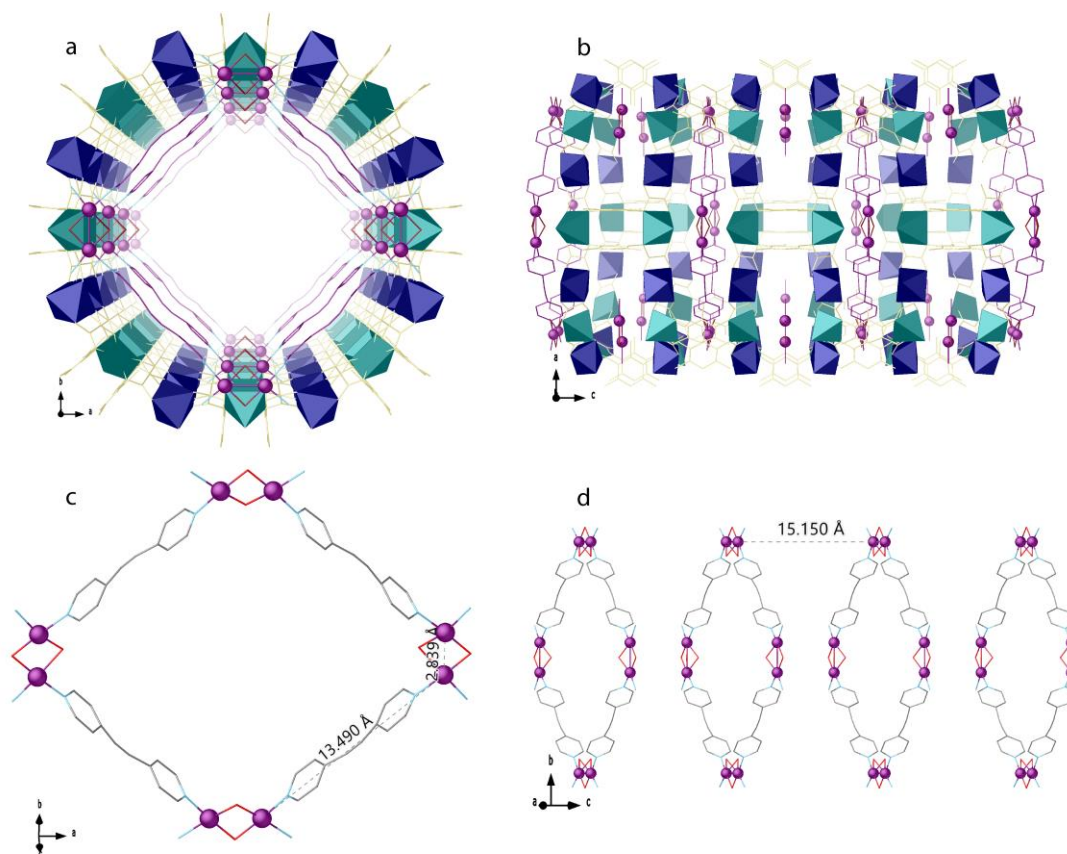


**Figure S3.** A portion of crystal structures of **2** obtained by SCXRD. (a-b) Perspective views of a channel of **2** along the *c* or *b* axes showing, in detail, the Pd<sup>II</sup><sub>8</sub> and Pd<sup>II</sup><sub>2</sub> complexes. (c) Perspective view of a Pd<sup>II</sup><sub>8</sub> SCC underlining the intra-assembly structural parameters related to Pd<sup>II</sup>...Pd<sup>II</sup> separations. (d) Perspective view of propagation within [101] direction of a single channel underlining the inter-assembly structural parameters related to Pd<sup>II</sup>...Pd<sup>II</sup> separations. Color scheme: Cu and Ni atoms from the network are represented by cyan and blue polyhedra, respectively, whereas organic ligands are depicted as yellow and purple sticks (in a-b) for ligand of the whole net and L<sub>1</sub> ligand, respectively. Purple spheres represent Pd<sup>2+</sup>, whereas red, blue and grey sticks represent oxygen, nitrogen and carbon atoms, respectively (in c-d).

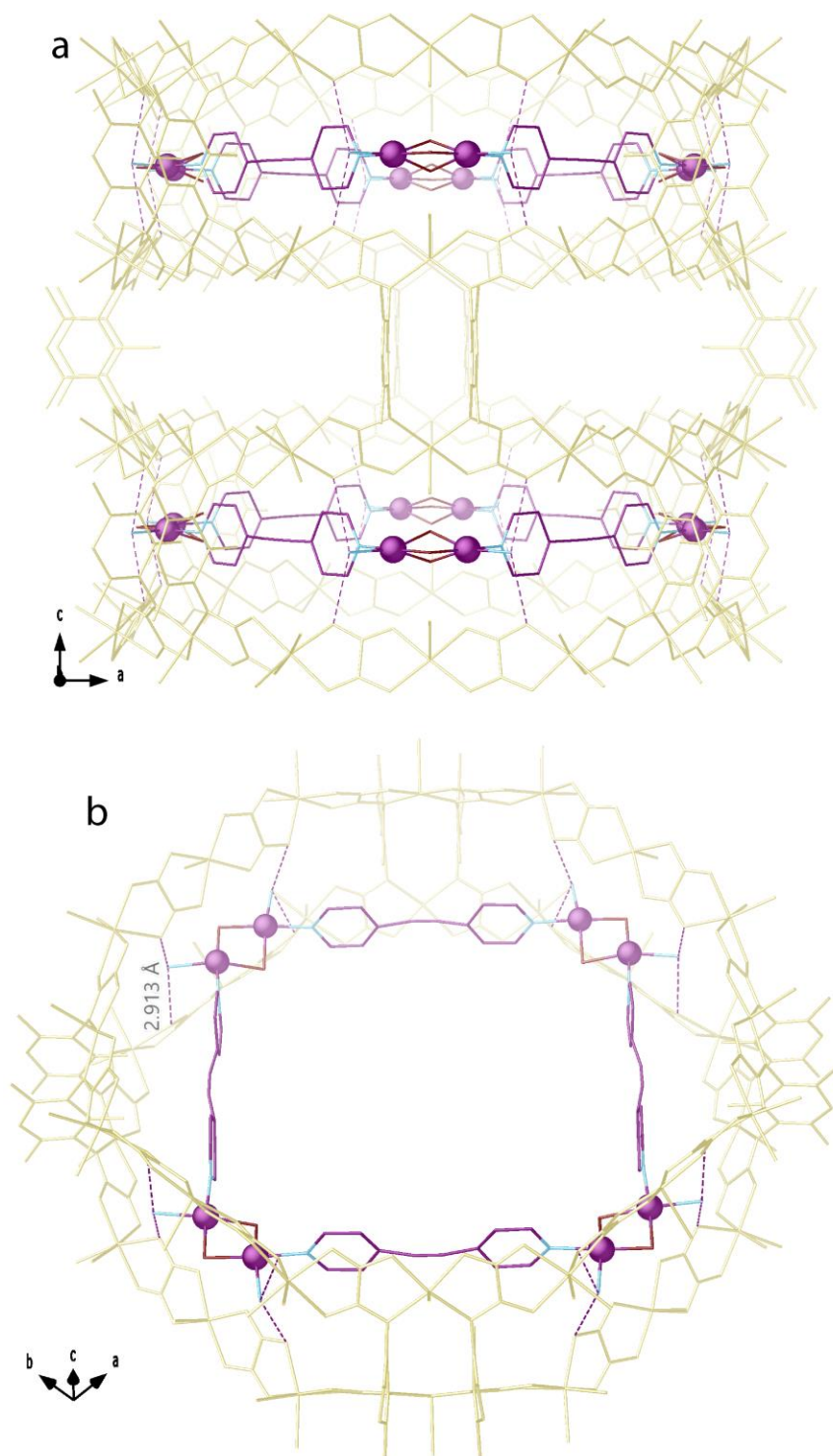


**Figure S4.** Perspective views of a portion of a pore of the crystal structure of **2** along the *b* axis and the [111] direction (a and b) showing the  $[\text{Pd}^{\text{II}}_8(\mu\text{-OH}_2)_8(\text{NH}_3)_8(\text{L}_1)_4]^{16+}$  SCCs and related structural parameters, stabilized by symmetric  $\text{NH}_3 \cdots \text{O}$  interactions [ $\text{H}_3\text{N} \cdots \text{O}_{\text{oxamate}}$  of 2.913(9) Å]. Color scheme: palladium, violet sphere; carbon and nitrogen atoms of the ligands  $\text{L}_1$  are depicted as purple and blue sticks, respectively; nitrogen atoms, blue sticks, whereas ligands atoms and metal ions of the whole net have been depicted as yellow sticks.

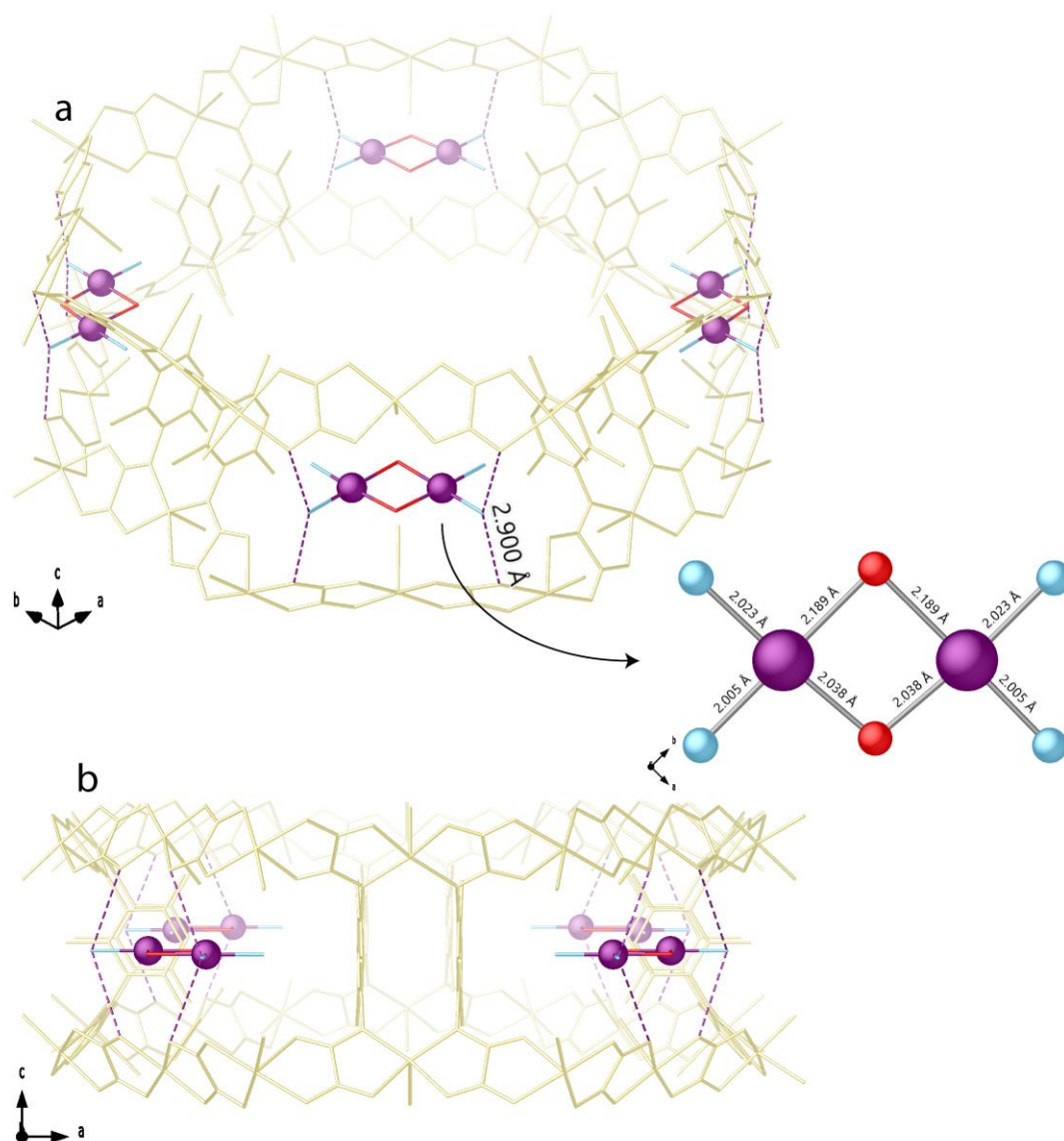


**Figure S5.** Further details of crystal structure of **2**. Perspective views of a portion of a pore along the [111] direction and the *b* axis (a and b) showing the  $[\text{Pd}^{\text{II}}_2(\mu\text{-OH}_2)(\text{NH}_3)_4]^{4+}$  dimers and related structural parameters, stabilized again by symmetric  $\text{NH}_3 \cdots \text{O}$  interactions [ $\text{H}_3\text{N} \cdots \text{O}_{\text{oxamate}}$  of 2.900(9) Å]. The inset shows the crystal structure of dimers within pores and its structural parameters; palladium, oxygen and nitrogen atoms are represented as violet, red and blue spheres. Color scheme: palladium, violet sphere; nitrogen and oxygen blue and red sticks, respectively, whereas ligands atoms and metal ions of the whole net have been depicted as yellow sticks.

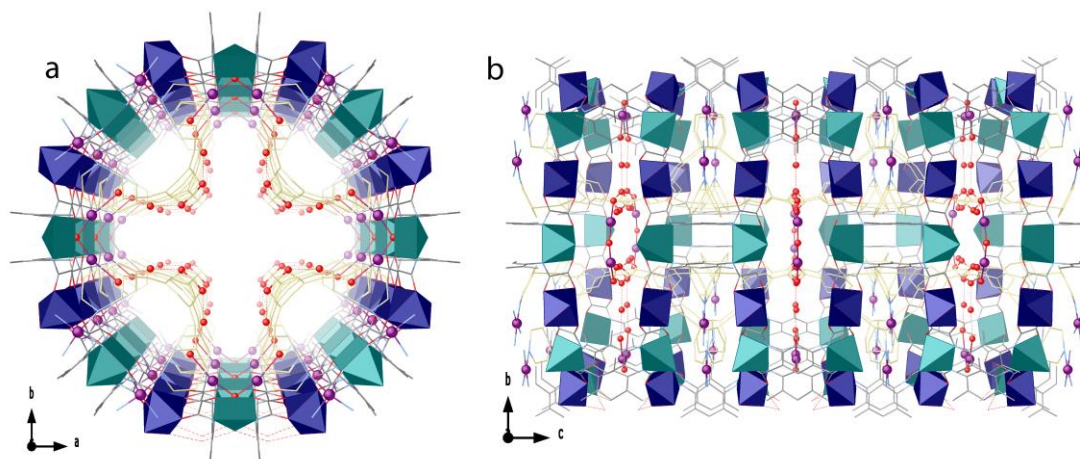


**Figure S6.** A portion of crystal structures of **3** obtained by SCXRD. (a-b) Perspective views of a channel of **3** along the *c* or *b* axes showing, the Pd<sup>II</sup><sub>16</sub> and Pd<sup>II</sup><sub>2</sub> complexes. Color scheme: Cu and Ni atoms from the network are represented by cyan and blue polyhedra, respectively, whereas organic ligands are depicted as grey and yellow sticks for ligand of the whole net and L<sub>2</sub> ligand, respectively. Purple spheres represent Pd<sup>2+</sup>, whereas red, blue and grey sticks represent oxygen, nitrogen and carbon atoms, respectively.

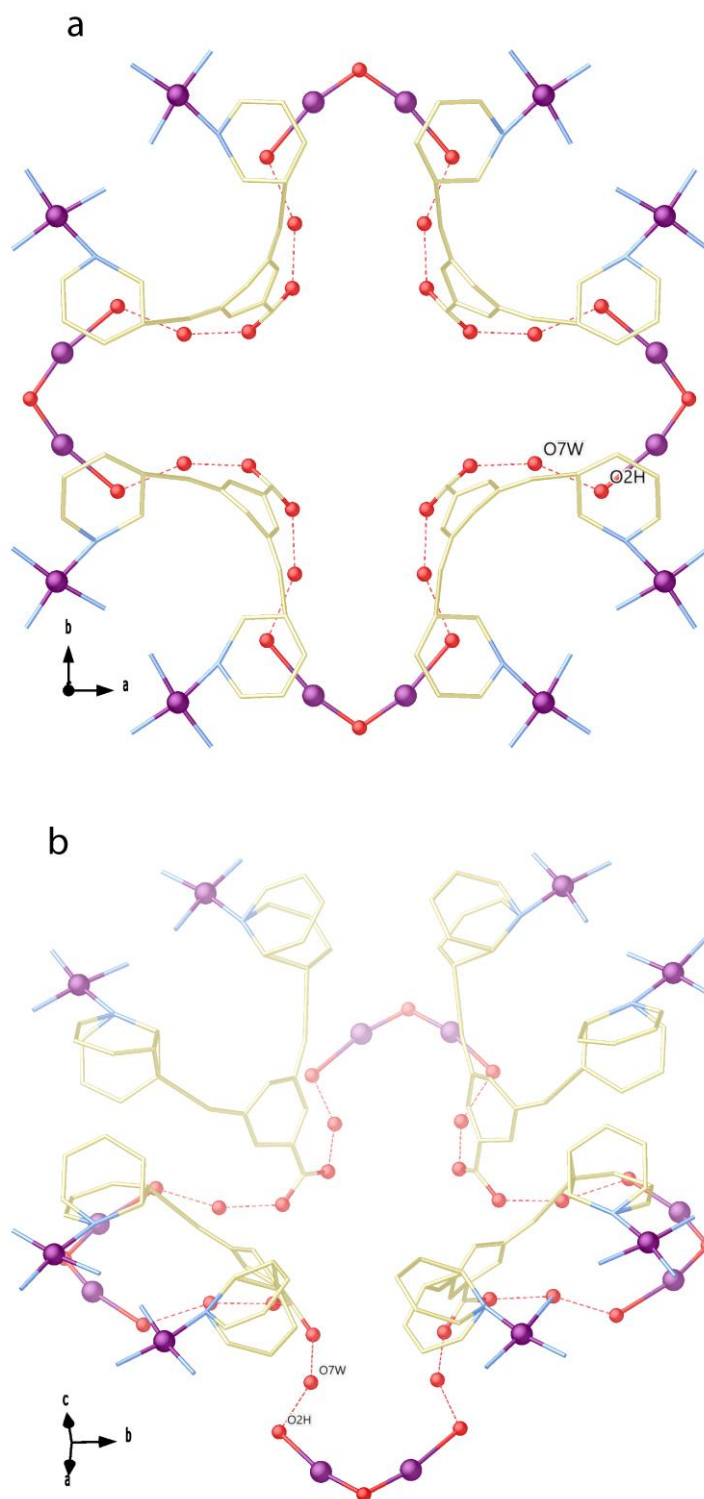


**Figure S7.** Crystal structure of Pd<sup>II</sup><sub>16</sub> SCCs in **3**. View along *c* crystallographic axis (a) and perspective view (b) of [Pd<sup>II</sup><sub>2</sub>(NH<sub>3</sub>)<sub>6</sub>(L<sub>2</sub>)] and [Pd<sup>II</sup><sub>2</sub>(μ-OH<sub>2</sub>)<sub>4</sub>(H<sub>2</sub>O)<sub>6</sub>] dimers, linked by water molecules, through strong hydrogen bonds [O⋯O of 2.89(4) and 2.89(3) Å for -COO⋯O<sub>water</sub> and O<sub>water</sub>⋯O<sub>water</sub>, respectively]. In [Pd<sup>II</sup><sub>2</sub>(μ-OH<sub>2</sub>)<sub>4</sub>(H<sub>2</sub>O)<sub>6</sub>] moieties not all waters have been found from ΔF maps. Color Scheme: Pd and O atoms are represented by purple and red spheres, respectively, whereas carbon and nitrogen atoms of the ligands L<sub>2</sub> are depicted as yellow and blue sticks, respectively. The overall positional disorder of phenyl rings of the ligand has not been removed from the representation.

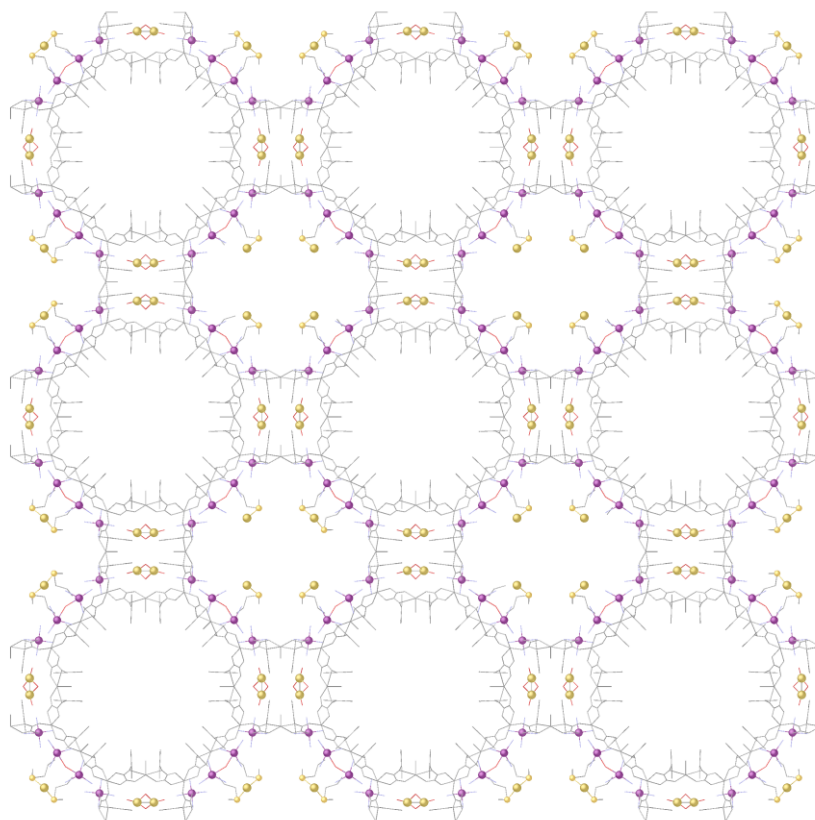


**Figure S8.** View along *c* crystallographic axis of crystal structure of **4** featuring hydrophilic channels filled by  $[\text{Pd}^{\text{II}}_2(\mu\text{-OH}_2)(\text{NH}_3)_6]$  dimers and  $[\text{Au}^{\text{III}}_2\text{Cl}_6\text{Pd}^{\text{II}}_2(\text{NH}_3)_6(\text{L}_3)_2]$  heterometallic SCCs (for which only a fragment has been detected, see Figure S9), together with  $[\text{Au}^{\text{III}}_2(\mu\text{-OH})_2(\text{OH})_4]$  dimers filling smallest square pores. Lattice water molecules and hydrogen atoms have been omitted for clarity. Color scheme: palladium, violet sphere; gold, gold spheres, oxygen and nitrogen, red and blue sticks, respectively. Ligands atoms and metal ions of the whole net have been depicted as grey sticks.

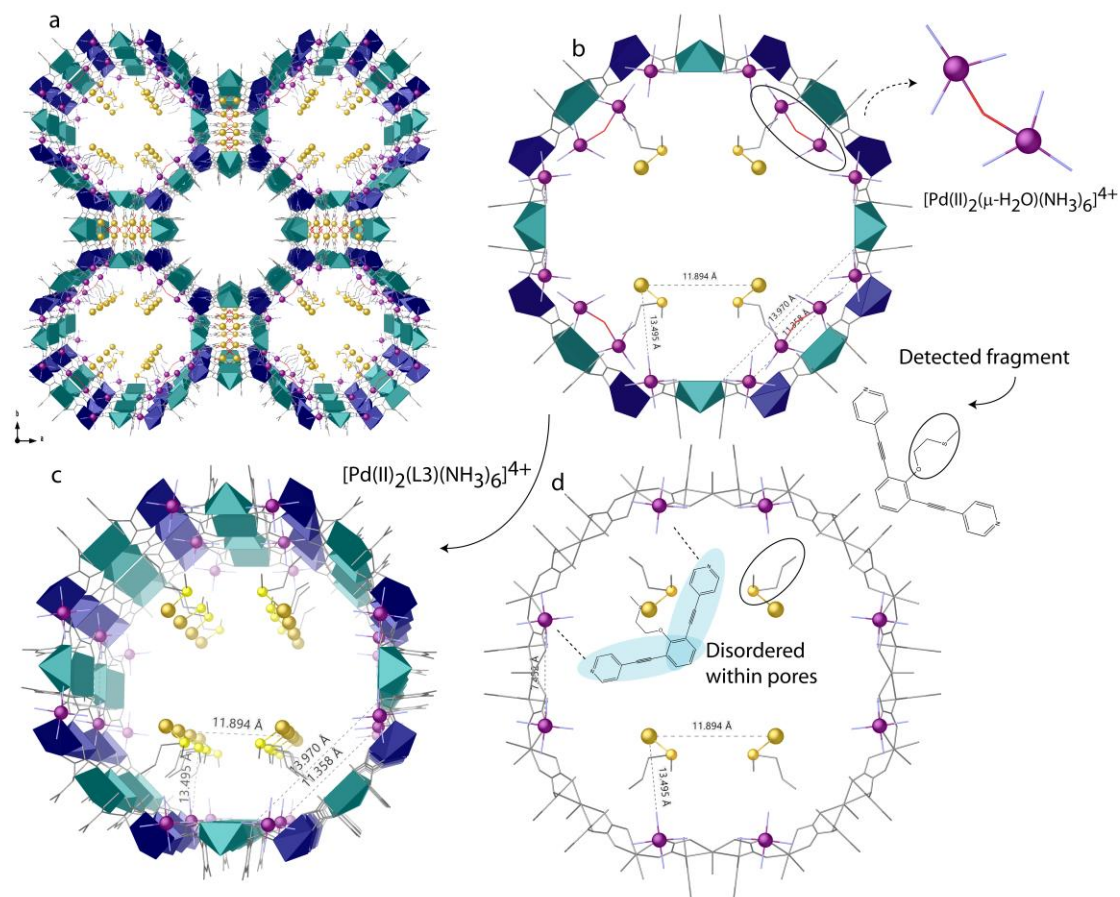


**Figure S9.** Details of crystal structure of **4**. (a) Perspective view along *c* crystallographic axis of the overall distribution of metal ions within pores. (b) Details of a single hydrophilic pore showing the detected fragments, by SCXRD, of  $[\text{Pd}^{\text{II}}_2(\mu\text{-OH}_2)(\text{NH}_3)_6]$  dimers and  $[\text{Au}^{\text{III}}_2\text{Cl}_6\text{Pd}^{\text{II}}_2(\text{NH}_3)_6(\text{L}_3)_2]$  heterometallic SCCs. (c-d) Views of a single pore along *c* axis representing only  $[\text{Au}^{\text{III}}_2\text{Cl}_6\text{Pd}^{\text{II}}_2(\text{NH}_3)_6(\text{L}_3)_2]$  fragments with parameters details related to Pd...Pd and Pd...Au separations and ligand scheme. Color scheme: Cu and Ni atoms from the network are represented by cyan and blue polyhedra, respectively, whereas organic ligands are depicted as grey sticks. Palladium, gold and sulfur, purple, gold and yellow spheres respectively, whereas red, blue and grey sticks represent oxygen, nitrogen and carbon atoms, respectively.

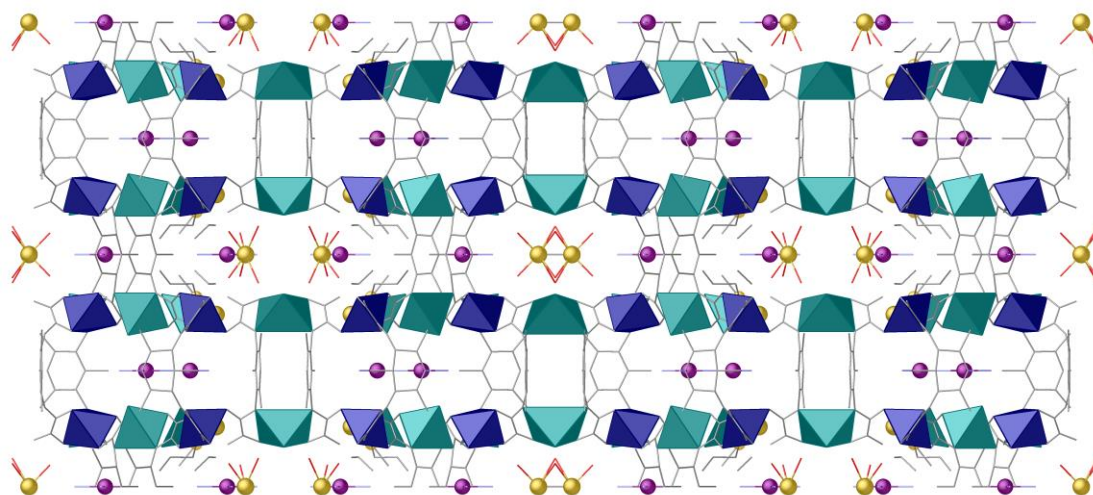


**Figure S10.** Perspective view of crystal structure of **4**, showing  $[\text{Au}^{\text{III}}_2(\mu\text{-OH})_2(\text{OH})_4]$  dimers (gold spheres) distributed within the square channels, and  $\text{Pd}^{\text{II}}\text{Au}^{\text{III}}$  complexes occupying the interlayer space of the wide octagonal channels most likely stabilized by the whole net, through interactions with the carboxylate- and/or carbonyl-oxygen atoms from the coordination network. Color scheme: Cu and Ni atoms from the network are represented by cyan and blue polyhedra, respectively, whereas organic ligands are depicted as grey sticks. Palladium, gold and sulfur, purple, gold and yellow spheres respectively, whereas red, blue and grey sticks represent oxygen, nitrogen and carbon atoms, respectively.

**<sup>1</sup>H and <sup>13</sup>C NMR Spectroscopy.** Spectra were recorded on Bruker DMX 500 instrument for L<sub>3</sub> in CDCl<sub>3</sub> and in a Bruker 300 MHz instrument using the appropriate solvent for the rest of the synthesized products. Chemical shifts are reported in parts per million (ppm) from low to high frequency and referenced to the residual solvent resonance.

**Magic Angle Spinning Solid <sup>13</sup>C NMR Spectroscopy.** <sup>13</sup>C solid-state NMR spectra were recorded at room temperature with a Bruker AVIII HD 400 WB spectrometer. The glass insert were fitted into 7 mm rotors and were spun at 5 kHz in a Bruker BL7 probe. <sup>13</sup>C CP/MAS NMR spectra were recorded with proton decoupling, with 1H 90° pulse length of 5 μs, and a recycle delay of 3s.

**Diffuse-reflectance UV-Vis.** Reflectance spectra in the region comprised between 190 and 1100 nm were recorded at room temperature on a spectrophotometer equipped with an integrating sphere. The mixture was contained in a quartz cell with 1 mm path length; the layer can therefore be regarded as infinitely thick, as required by the Kubelka-Munk theory. Absorbance values ( $A_\lambda$ ) were calculated from reflectance ones ( $R_\lambda$ ) according to the Kubelka-Munk transformation:  $A_\lambda = (1-R_\lambda)^2/2R_\lambda$ .

**Infrared Spectroscopy.** Fourier transform infrared (FT-IR) measurements were recorded on a Thermo Nicolet iS10 spectrophotometer after impregnating the window with a dichloromethane solution of the analyte, and then leaving to evaporate, or by previous mixture of the solid with KBr. Deconvolution of the IR spectra has been performed in the Origin software using Gaussian curves where the full width at half-maximum (fwhm) of the individual bands has been taken as constant. The peak areas are normalized to the sample weight.

**Raman spectroscopy.** Raman spectra were recorded at RT with a 514 nm laser excitation on a Renishaw Raman Spectrometer (“in via”) equipped with a CCD detector. The laser power on a sample of MOF 4 (with or without Au atoms) was 25 mW and a total of 20 acquisitions were taken for each spectrum.

**Microscopy measurements.** Scanning Electron Microscopy coupled with Energy Dispersive X-ray (SEM/EDX) was carried out with a XL 30 ESEM (PHILIPS) microscope equipped with a home-made EDX energy dispersive x-ray detector.

**X-ray Powder Diffraction Measurements.** Polycrystalline samples of 2–4, before and after catalysis, were introduced into 0.5 mm borosilicate capillaries prior to being mounted and aligned on a Empyrean PANalytical powder diffractometer, using Cu K $\alpha$  radiation ( $\lambda = 1.54056 \text{ \AA}$ ). For each sample, five repeated measurements were collected at room temperature ( $2\theta = 2\text{--}60^\circ$ ) and merged in a single diffractogram.

**X-ray photoelectron spectroscopy (XPS) measurements.** Samples were prepared by dropping a solid water suspension onto a molybdenum plate followed by air drying, and then measurements were performed on a SPECS spectrometer equipped with a Phoibos 150 MCD-9 analyzer using non-monochromatic Mg KR (1253.6 eV) X-ray source working at 50 W. As an internal reference for the peak positions in the XPS spectra, the C1s peak has been set at 284.5 eV.

**Electrochemical Measurements.** Voltammetric measurements were performed at glassy carbon working electrode in solutions of the different compounds and their mixtures in 0.10 M Bu<sub>4</sub>NPF<sub>6</sub>/MeCN. A CH I660 potentiostat was used in an electrochemical cell using Pt mesh auxiliary electrode and a Pt wire pseudo-reference electrode to avoid water contamination. The measured potentials can be passed to the

ferrocene/ferrocenium scale by subtracting 0.16 V. The solutions were optionally deaerated by bubbling Ar for 10 min.

Conventional solution-phase voltammetry was performed as previously described for studying homocoupling reaction.<sup>17</sup> The voltammetric and catalytic activity of the studied SCCs@MOFs was analyzed using microparticulate deposits of such compounds on glassy carbon electrode. Such deposits were prepared by evaporation on the electrode surface of a drop (50  $\mu\text{L}$ ) of a suspension (1 mg/mL) of the solid in ethanol.<sup>18</sup>

**Other techniques.** ESI mass spectrometry and elemental (C,H,N,S) analyses were performed by departmental services at The University of Manchester, the Universitat de València and the ITQ. Carbon, hydrogen, nitrogen and sulphur analysis was performed using a Flash 200 elemental analyser. Metal analysis was performed by Thermo iCap 6300 Inductively Coupled Plasma Optical Emission Spectroscopy (ICP-OES).

The thermogravimetric analysis was performed on crystalline samples under a dry  $\text{N}_2$  atmosphere with a Mettler Toledo TGA/STDA 851° thermobalance operating at a heating rate of 10  $^\circ\text{C min}^{-1}$ .

The  $\text{N}_2$  adsorption–desorption isotherms at 77 K were carried out on crystalline samples of **1–4** with a Micromeritics ASAP2020 instrument. Samples were evacuated at 80  $^\circ\text{C}$  during 16 hours under  $10^{-6}$  Torr prior to their analysis.

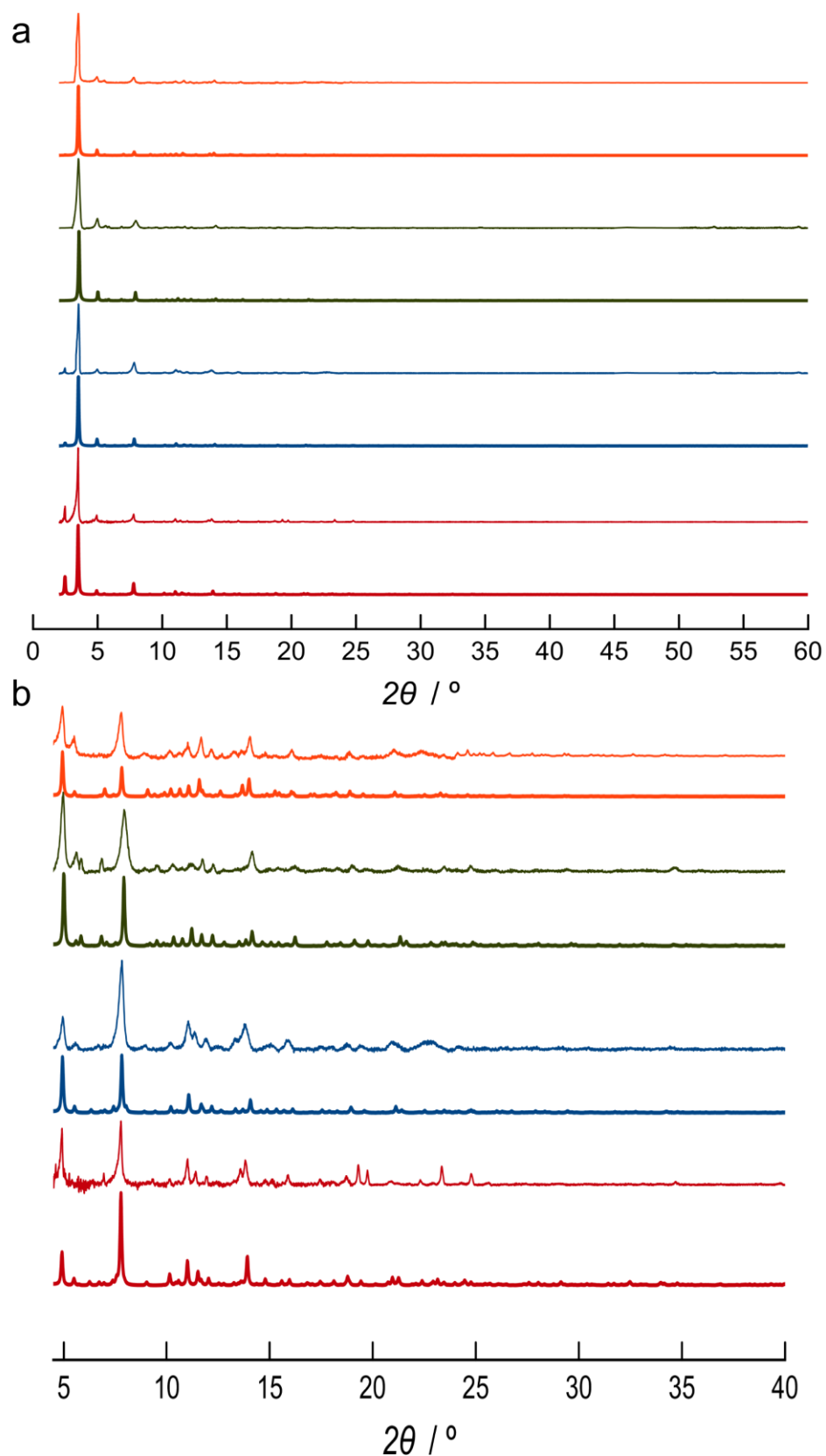


**Figure S11.** Calculated (bold lines) and experimental (solid lines) PXRD pattern profiles of **1** (red), **2** (blue), **3** (green) and **4** (orange) in the  $2\theta$  range  $2.0$ – $60.0^\circ$  (a) and enlarged image in the range  $4.5$ – $40.0^\circ$  (b).

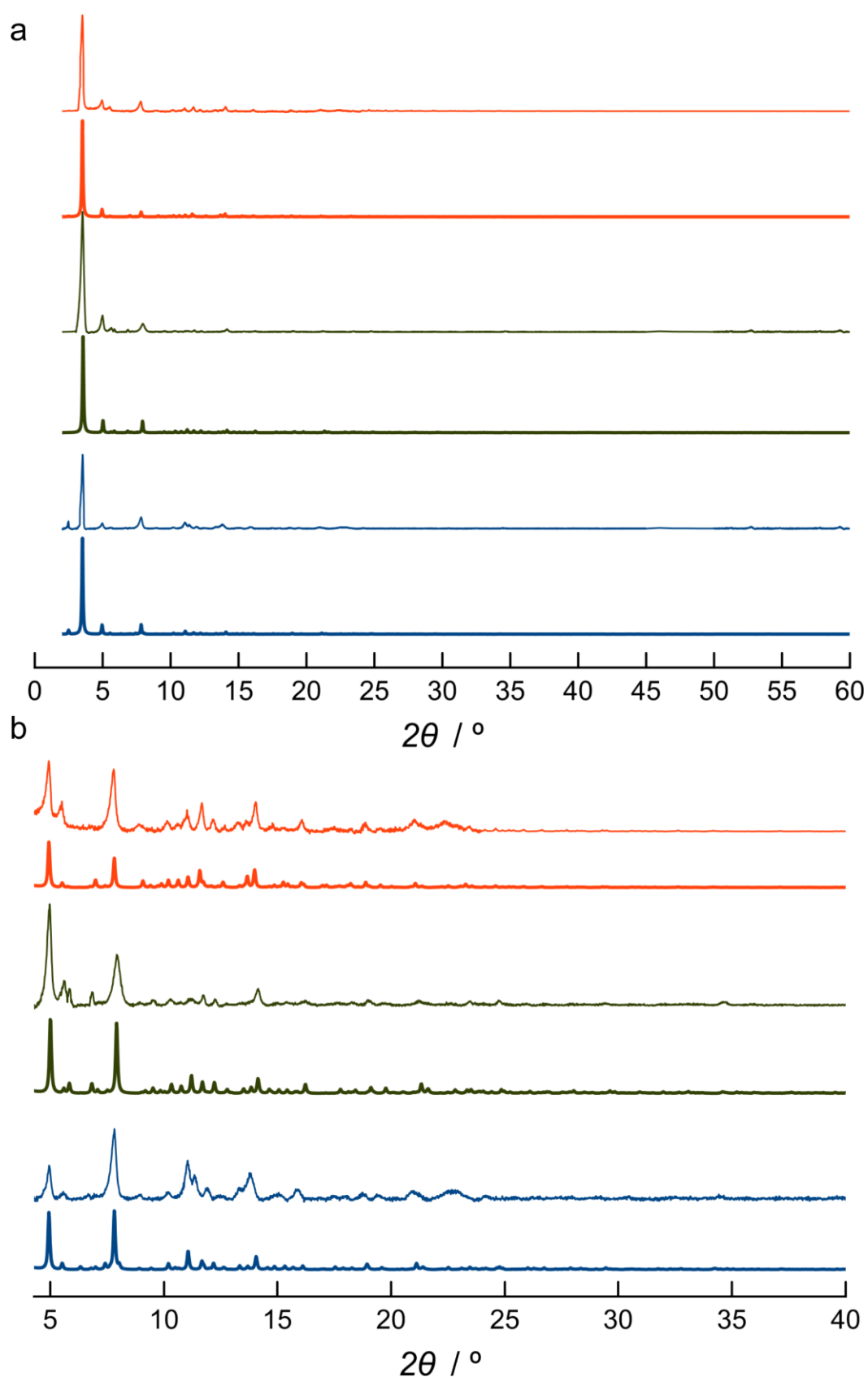


**Figure S12.** Calculated (bold lines) and experimental (solid lines) PXRD pattern profiles of **2** (blue), **3** (green) and **4** (orange) in the  $2\theta$  range  $2.0$ – $60.0^\circ$  after catalytic experiments (a) and enlarged image in the range  $4.5$ – $40.0^\circ$  (b).

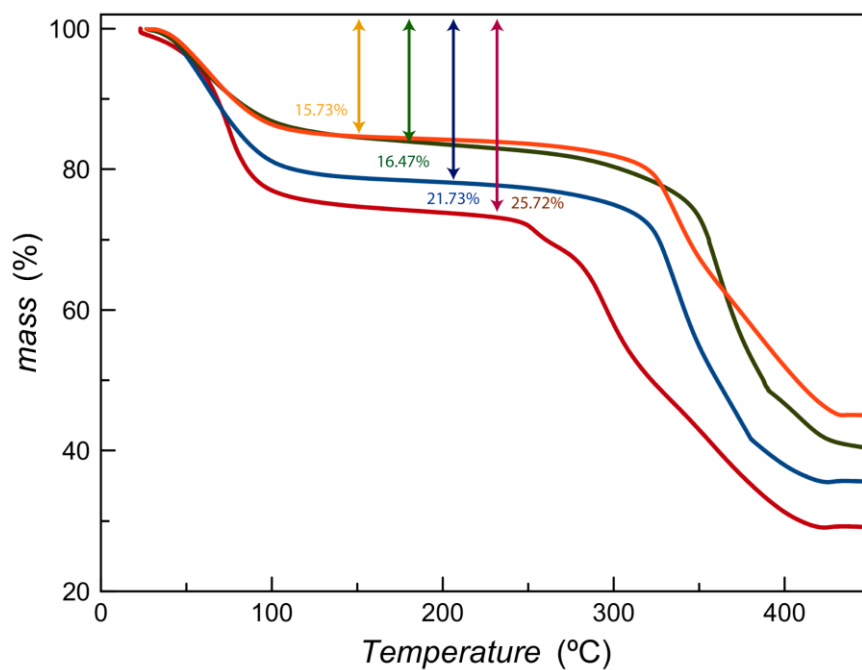


**Figure S13.** Thermo-Gravimetric Analyses (TGA) of **1** (red), **2** (blue), **3** (green) and **4** (gold) under dry N<sub>2</sub> atmosphere.

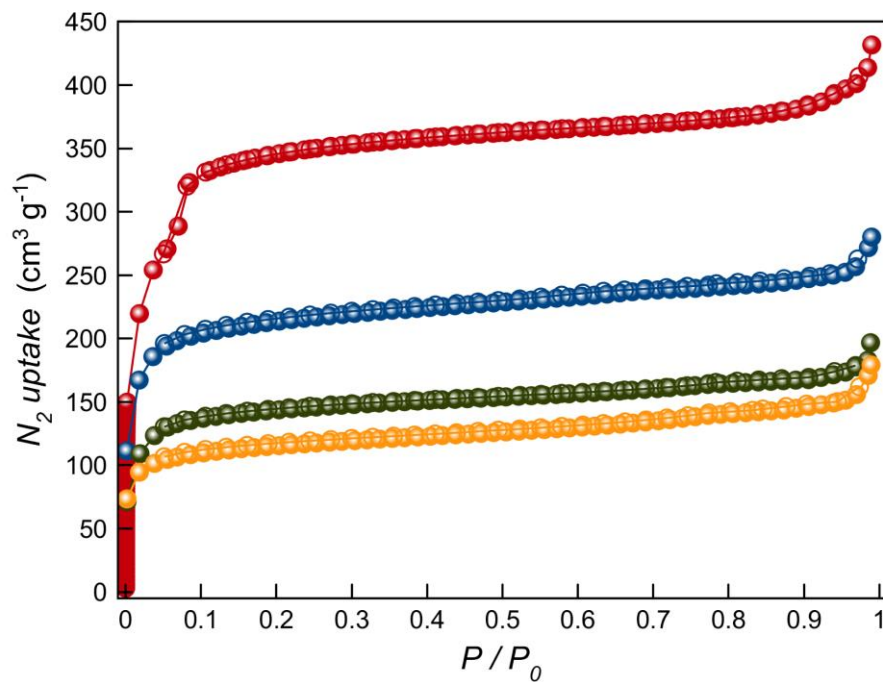


**Figure S14.**  $N_2$  (77 K) adsorption isotherm for the activated compounds **1** (red), **2** (blue), **3** (green) and **4** (gold). Filled and empty symbols indicate the adsorption and desorption isotherms, respectively. The sample was activated at 80 °C under reduced pressure for 16 h prior to carry out the sorption measurements.

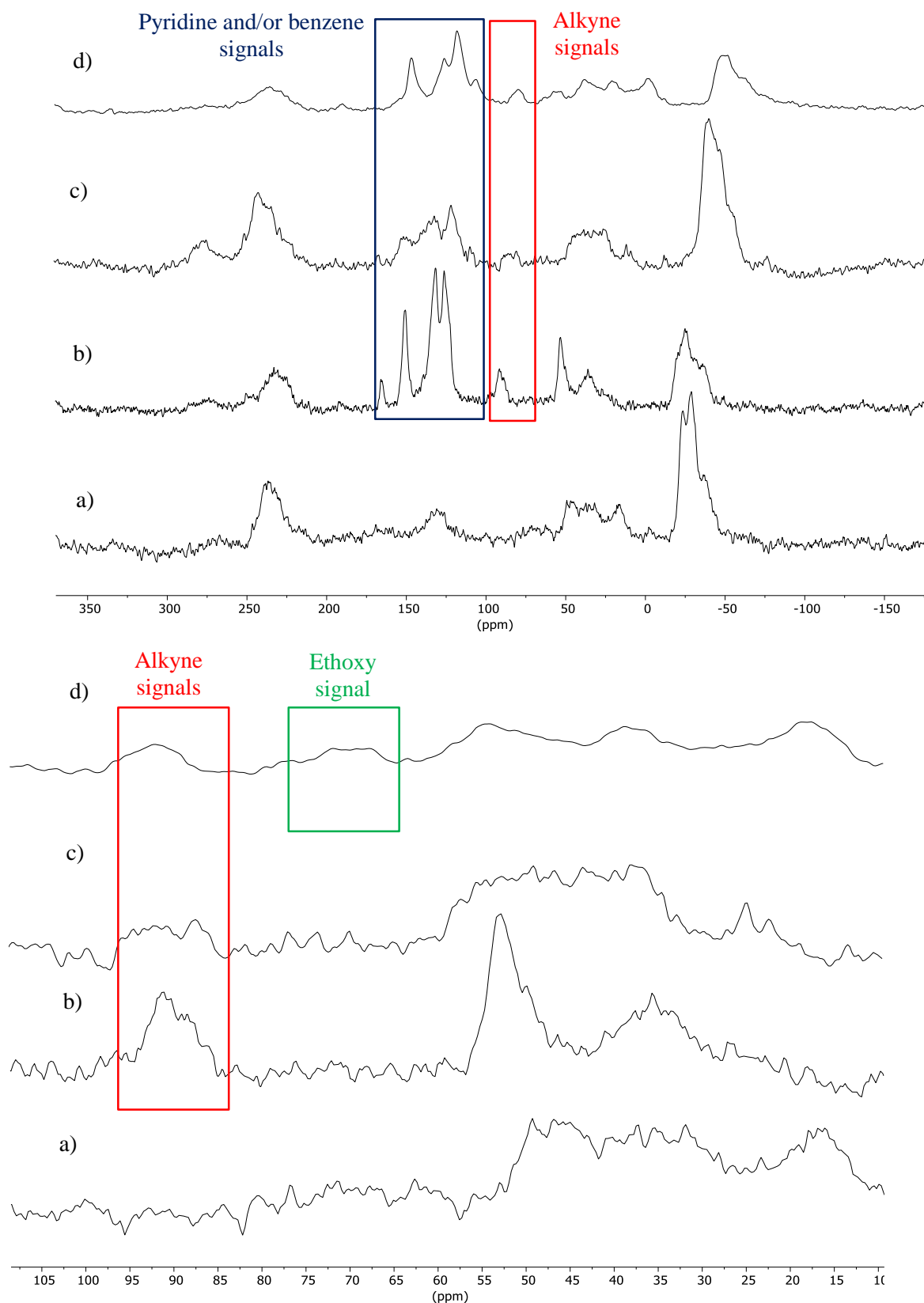


**Figure S15.** Full spectra (top) and 10–105 ppm region (bottom) of the magic-angle spinning solid  $^{13}\text{C}$  NMR of MOF 1 (a) and SCCs@MOFs 2 (b), 3 (c) and 4 (d).

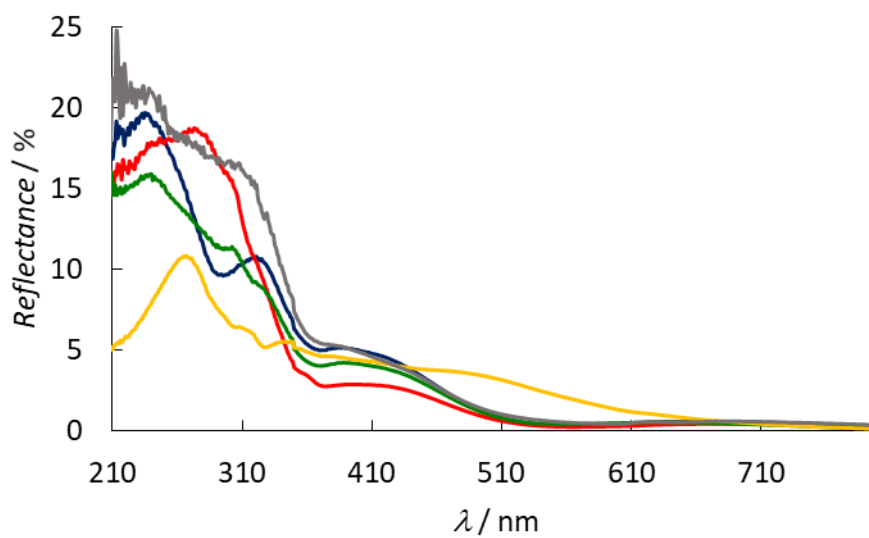


**Figure S16.** Diffuse-reflectance UV-vis spectrum of MOF **1** (blue solid lines), SCCs@MOFs **2** (red solid lines), **3** (green solid lines) and **4** (grey solid lines), and Pd<sub>4</sub>(L<sub>1</sub>)<sub>4</sub> (yellow solid lines) UV-vis spectrum in solution.

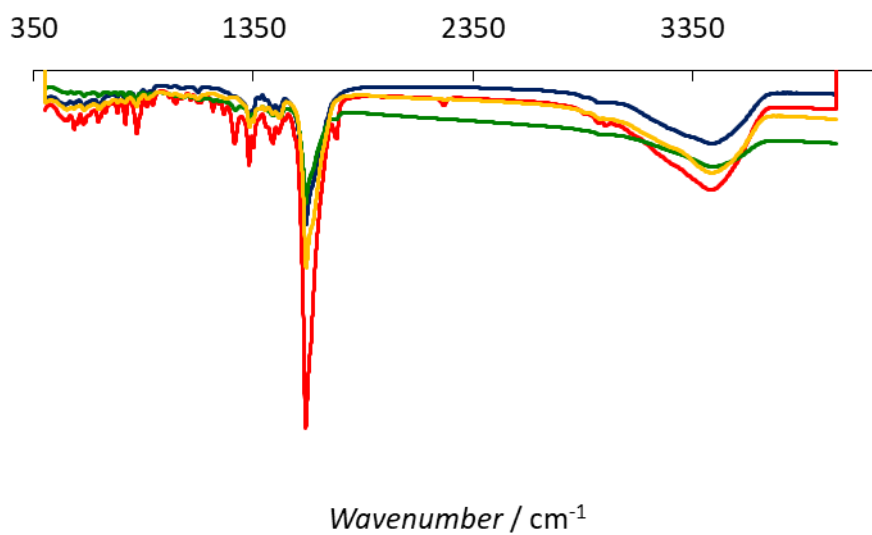


**Figure S17.** Fourier transform infrared spectrum of MOF **1** (blue solid lines), SCCs@MOFs **2** (red solid lines), **3** (green solid lines) and **4** (yellow solid lines).

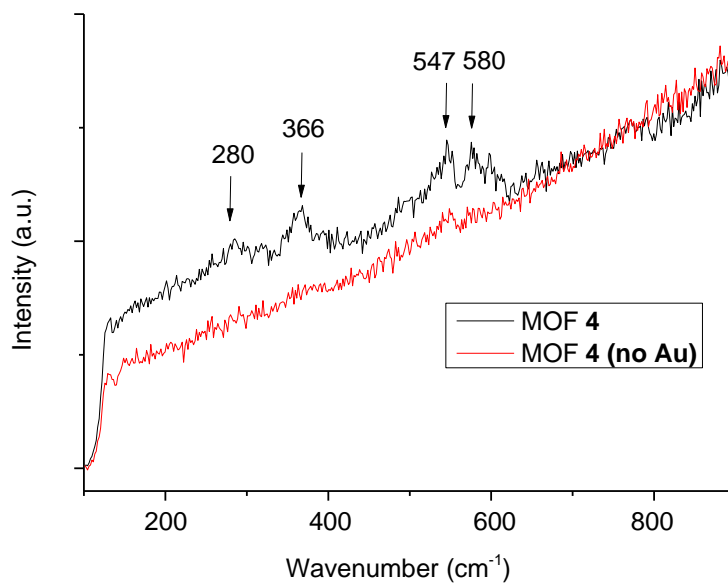


**Figure S18.** Raman spectra obtained after exciting MOF 4 before and after incorporating gold, with a laser light at 521 nm. Excitation with a laser light at 785 nm did not give significant results.

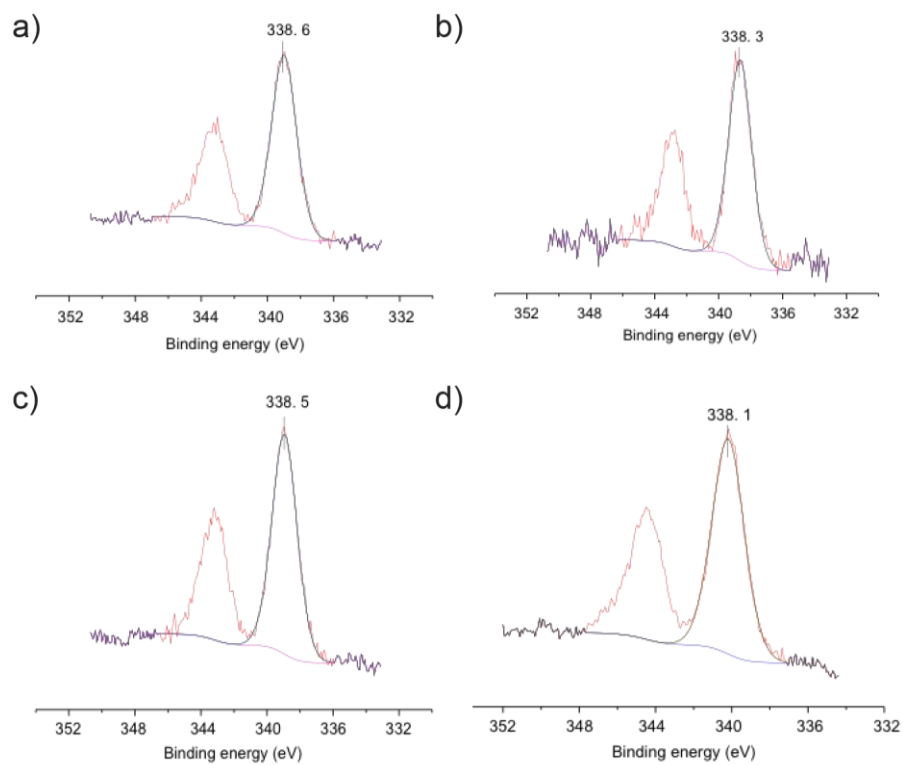


**Figure S19.** X-ray photoelectron spectroscopy (XPS) of MOF 1 (a), SCCs@MOFs 2 (b), 3 (c) and 4 (d).

## Catalytic experiments

**General reaction procedure for the homocoupling of boronic acids catalysed by 1–3.** In a 10 ml glass vial equipped with a stirring bar, the corresponding boronic acid (0.1 mmol), KF (0.1 mmol, 5.8 mg), *p*-benzoquinone (0.2 mmol, 21.6 mg) and dodecane as internal standard (10  $\mu$ L) were charged together with a 2 mol% of the corresponding palladium catalyst (3.5 mg for **2** and 3.3 mg for **3**) in 1.5 ml of ethyl acetate or *o*-xylene under a N<sub>2</sub> atmosphere. The vial was closed with a septum and the mixture was placed in a pre-heated oil bath at the required temperature and stirred for the indicated time. After the reaction time, the possible excess of boronic acid was quenched with neopentyl glycol and the mixture was analysed by GC and by GC-MS when necessary. The homocoupling products were isolated by preparative TLC using hexane as eluent.

**General reaction procedure for the homocoupling of boronic acids catalysed by Pd(OAc)<sub>2</sub>/Py or Pd<sub>4</sub>(L<sub>1</sub>)<sub>4</sub>.** In a 25 ml glass vial equipped with a stirring bar, the corresponding boronic acid (0.2 mmol), KF (0.2 mmol, 11.6 mg), *p*-benzoquinone (0.4 mmol, 43.2 mg) and dodecane as internal standard (20  $\mu$ L) were charged together with a 2 mol% of Pd(OAc)<sub>2</sub>/pyridine (0.9 mg/0.3 $\mu$ L) or Pd<sub>4</sub>(L<sub>1</sub>)<sub>4</sub> (1.37 mg) in 2 ml of ethyl acetate under a N<sub>2</sub> atmosphere. The vial was closed with a septum and the mixture was placed in a pre-heated oil bath at the required temperature and stirred for the indicated time. After the reaction time, the possible excess of boronic acid was quenched with neopentyl glycol and the mixture was analysed by GC and by GC-MS when necessary.

**General reaction procedure for the homocoupling of alkynes catalysed by 1–4.** In a 10 ml glass vial equipped with a stirring bar, the corresponding alkyne (0.1 mmol), DABCO (0.3 mmol, 33.6 mg) and dodecane as internal standard (10  $\mu$ L) were charged together with a 2 mol% of the corresponding palladium catalyst (3.5 mg for **1**, 3.5 mg for **2**, 3.3 mg for **3** and 4.2 mg for **4**) in 1.5 ml of ethyl acetate under air atmosphere. The vial was closed with a septum and the mixture was placed in a pre-heated oil bath at the required temperature and stirred for the indicated time. After the reaction time, mixture was analysed by GC and by GC-MS when necessary. The homocoupling products were isolated by preparative TLC using mixtures ethyl acetate/hexane as eluent. For the in-flow reaction, a similar reaction mixture for alkyne **8a** was passed at 0.01 ml·min<sup>-1</sup> through MOF **4** placed in a tubular (4 mm diameter) fixed-bed reactor externally at 60 °C, collecting samples each hour to be analysed by GC and GC-MS.

**General reaction procedure for the homocoupling of alkynes catalysed by the Pd(OAc)<sub>2</sub>/Py or Pd<sub>4</sub>(L<sub>1</sub>)<sub>4</sub>.** In a 25 ml glass vial equipped with a stirring bar, the corresponding alkyne (0.2 mmol), DABCO (0.6 mmol, 67.3 mg) and dodecane as internal standard (20  $\mu$ L) were charged together with a 2 mol% of Pd(OAc)<sub>2</sub>/pyridine (0.9 mg/0.3 $\mu$ L) or the the Pd<sub>4</sub>(L<sub>1</sub>)<sub>4</sub> (1.37 mg) in 2 ml of ethyl acetate under air atmosphere. The vial was closed with a septum and the mixture was placed in a pre-heated oil bath at the required temperature and stirred for the indicated time. After the reaction time, the mixture was analysed by GC and by GC-MS, when necessary.

**General reaction procedure for the cross-coupling of phenylacetylene **8a** with alkynes **8f-h** catalysed by **4**.** In a 10 ml glass vial equipped with a stirring bar, the corresponding alkyne **8f-h** (0.3 mmol), phenylacetylene **8a** (0.1 mmol, 10.2 mg), DABCO (0.3 mmol, 33.7 mg), and dodecane as internal standard (10  $\mu$ L) were charged together with a 2 mol% of **4** (4.2 mg) in 1.5 ml of ethyl acetate under air atmosphere.

The vial was closed with a septum and the mixture was placed in a pre-heated oil bath at the required temperature and stirred for the indicated time. After the reaction time, mixture was analysed by GC and by GC-MS when necessary.

**General reaction procedure for the cross-coupling of 2-thienylboronic acid **5a** with **8a** catalysed by **1-4**.** In a 10 ml glass vial equipped with a stirring bar, the corresponding alkyne (0.3 mmol), 2-thienylboronic acid **5a** (0.1 mmol, 12.8 mg), DABCO (0.9 mmol, 100.9 mg), KF (0.1 mmol, 5.8 mg), *p*-benzoquinone (0.1 mmol, 10.8 mg) and dodecane as internal standard (10  $\mu$ L) were charged together with a 2 mol% of the corresponding palladium catalyst (3.5 mg for **2**, 3.3 mg for **3** and 4.2 mg for **4**) in 1.5 ml of ethyl acetate under air atmosphere. The vial was closed with a septum and the mixture was placed in a pre-heated oil bath at the required temperature and stirred for the indicated time. After the reaction time, mixture was analysed by GC and by GC-MS when necessary. Attempts to isolate the cross-coupling products were done by preparative TLC using mixtures ethyl acetate/hexane as eluent, although only mixtures of compounds **10** and **9** were obtained.

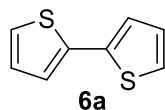
**General reaction procedure for the cross-coupling of 2-thienylboronic acid **5a** with **8a** catalysed by Pd(OAc)<sub>2</sub>/Py or Pd<sub>4</sub>(L<sub>1</sub>)<sub>4</sub>.** In a 25 ml glass vial equipped with a stirring bar, the corresponding alkyne (0.6 mmol), 2-thienylboronic acid **5a** (0.2 mmol, 25.6 mg), DABCO (1.8 mmol, 201.9 mg) and dodecane as internal standard (20  $\mu$ L) were charged together with a 2 mol% of Pd(OAc)<sub>2</sub>/pyridine (0.9 mg/0.3 $\mu$ L) or the Pd<sub>4</sub>(L<sub>1</sub>)<sub>4</sub> (1.37 mg) in 2 ml of ethyl acetate under air atmosphere. The vial was closed with a septum and the mixture was placed in a pre-heated oil bath at the required temperature and stirred for the indicated time. After the reaction time, the mixture was analysed by GC and by GC-MS, when necessary.

**Reuses.** The corresponding general reaction procedure above was followed for the corresponding SCCs@MOF catalyst in a ten-fold scale. After the reaction time, the solid catalyst was recovered by filtration and washed with ethyl acetate and water. After drying, the catalyst was weighted and the reagents and solvent added in proportional amounts to keep the initial relative molar ratios.

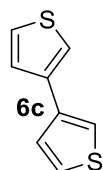
**Hot-filtration experiments.** Following the general reaction procedure above, the hot reaction mixture was filtered through a 0.25  $\mu$ m Teflon filter into a new vial equipped with a magnetic stirrer and placed at the reaction temperature, and the filtrates were periodically analysed by GC to compare with the results obtained with the solid catalyst still in.

**Synthesis of Phenylacetylene-*d* **8a-d**.**<sup>19</sup> An oven-dried schlenk flask equipped with a stir bar was charged with phenylacetylene (1.1 mL, 10 mmol, 1.0 equiv) and anhydrous THF (15 mL, 0.67 M). The solution was cooled to -78 °C and *n*BuLi (2.5 M in hexanes, 6 mL, 15 mmol, 1.5 equiv) was added in a dropwise fashion over 5 min. The solution was stirred at -78 °C for 20 min after which point it was warmed to RT and stirred for an additional 20 min. The mixture was then cooled to -78 °C and D<sub>2</sub>O (3 mL, excess) was added. Then, it was allowed to warm to RT and stirred for 20 min. The reaction was quenched with 3M HCl and extracted with diethyl ether (3x20 mL). The combined organic extracts were dried with MgSO<sub>4</sub>, filtered, and the solvent was carefully removed with use of a rotary evaporator (no heating, product is volatile) to give phenylacetylene-*d* as a clear oil (0.51 g, 50% yield). <sup>1</sup>H NMR spectra matched with those previously reported.

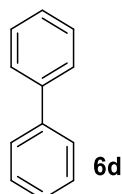
### Characterization of the isolated compounds:



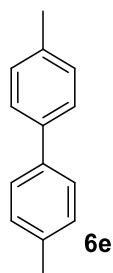
**2,2'-Bithiophene (6a).**<sup>20</sup> Yield: 54%. <sup>1</sup>H NMR (300 MHz, CDCl<sub>3</sub>)  $\delta$ : 7.22 (dd,  $J$  = 5.1, 1.0 Hz, 2H), 7.19 (dd,  $J$  = 3.6, 1.0 Hz, 2H), 7.03 (dd,  $J$  = 5.1, 3.6 Hz, 2H). <sup>13</sup>C NMR (75 MHz, CDCl<sub>3</sub>)  $\delta$ : 137.56, 127.90, 124.49, 123.91. IR ( $\nu$ , cm<sup>-1</sup>): 698, 743, 912, 1050, 1250, 1770, 2990. GC-MS ( $m/z$ , M<sup>+</sup> 287), major peaks found: 166 (100%), 121 (32%), 93 (5%), 69 (9%), 45 (7%).



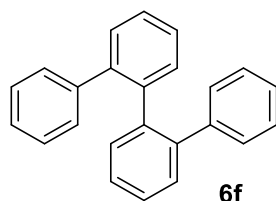
**3,3'-Bithiophene (6c).**<sup>21</sup> Yield: 57%. <sup>1</sup>H NMR (300 MHz, CDCl<sub>3</sub>)  $\delta$ : 7.39 – 7.36 (m, 2H), 7.36 – 7.32 (m, 4H). IR ( $\nu$ , cm<sup>-1</sup>): 1089, 1468, 1410, 3411. GC-MS ( $m/z$ , M<sup>+</sup> 287), major peaks found: 166 (100%), 121 (33%), 95 (4%), 69 (7%), 45 (10%).



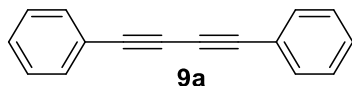
**1,1'-Biphenyl (6d).**<sup>22</sup> Yield: 38%. <sup>1</sup>H NMR (300 MHz, CDCl<sub>3</sub>)  $\delta$ : 7.65 (d,  $J$  = 7.3 Hz, 4H), 7.49 (dd,  $J$  = 7.5, 7.5 Hz, 1H), 7.44 – 7.36 (m, 2H). <sup>13</sup>C NMR (75 MHz, CDCl<sub>3</sub>)  $\delta$ : 141.40, 128.89, 127.39, 127.31. IR ( $\nu$ , cm<sup>-1</sup>): 697, 728, 1250, 1770, 2990. GC-MS ( $m/z$ , M<sup>+</sup> 287), major peaks found: 154 (100%), 128 (5%), 102 (4%), 76 (11%), 51 (6%), 28 (4%).



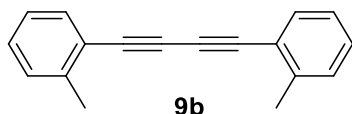
**4,4'-Dimethyl-1,1'-biphenyl (6e).**<sup>23</sup> Yield: 18%. <sup>1</sup>H NMR (300 MHz, CDCl<sub>3</sub>)  $\delta$ : 7.55 (d,  $J$  = 8.1 Hz, 4H), 7.29 (t,  $J$  = 7.8 Hz, 4H), 2.46 (s, 6H). <sup>13</sup>C NMR (75 MHz, CDCl<sub>3</sub>)  $\delta$ : 138.44, 136.80, 129.57, 126.94, 21.19. IR ( $\nu$ , cm<sup>-1</sup>): 803, 1250, 1770, 2990. GC-MS ( $m/z$ , M<sup>+</sup> 287), major peaks found: 182 (100%), 168 (44%), 152 (10%), 115 (8%), 90 (12%), 28 (8%).



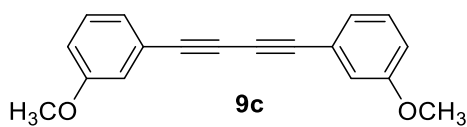
**1,1':2',1'':2'',1'''-Quaterphenyl (6f).**<sup>24</sup> Yield: 50%. <sup>1</sup>H NMR (300 MHz, CDCl<sub>3</sub>)  $\delta$ : 7.44 – 7.38 (m, 2H), 7.37 – 7.29 (m, 4H), 7.21 – 7.13 (m, 2H), 7.08 (dd,  $J = 7.2, 7.2$  Hz, 2H), 6.99 (dd,  $J = 7.3, 7.3$  Hz, 4H), 6.61 (d,  $J = 7.0$  Hz, 4H). IR ( $\nu$ , cm<sup>-1</sup>): 698, 742, 1430, 1470, 2920, 3050. GC-MS ( $m/z$ , M<sup>+</sup> 287), major peaks found: 306 (100%), 276 (7%), 228 (33%), 202 (7%), 145 (22%), 77 (5%).



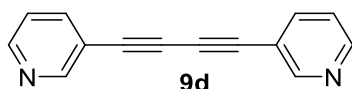
**1,4-Diphenylbuta-1,3-diyne (9a).**<sup>25</sup> Yield: 92%. <sup>1</sup>H NMR (300 MHz, CDCl<sub>3</sub>)  $\delta$ : 7.60 – 7.49 (m, 4H), 7.43 – 7.30 (m, 6H). <sup>13</sup>C NMR (75 MHz, CDCl<sub>3</sub>)  $\delta$ : 132.65, 129.35, 128.58, 121.97, 81.71, 74.08. IR ( $\nu$ , cm<sup>-1</sup>): 687, 755, 915, 1440, 1480, 1590, 2150, 3050.



**1,4-Di-*o*-tolylbuta-1,3-diyne (9b).**<sup>26</sup> Yield: 98%. <sup>1</sup>H NMR (300 MHz, CDCl<sub>3</sub>)  $\delta$ : 7.50 (d,  $J = 7.6$  Hz, 2H), 7.32 – 7.10 (m, 6H), 2.50 (s, 6H). <sup>13</sup>C NMR (75 MHz, CDCl<sub>3</sub>)  $\delta$ : 141.78, 133.07, 129.72, 129.24, 125.80, 121.90, 81.30, 77.69, 20.86. IR ( $\nu$ , cm<sup>-1</sup>): 712, 754, 1040, 1110, 1460, 1480, 2140, 2920, 3060. GC-MS ( $m/z$ , M<sup>+</sup> 230), major peaks found: 230 (100%), 202 (20%), 115 (61%).



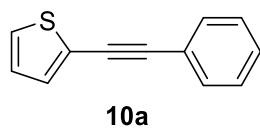
**1,4-Bis(3-methoxyphenyl)buta-1,3-diyne (9c).**<sup>25</sup> Yield: 72%. <sup>1</sup>H NMR (300 MHz, CDCl<sub>3</sub>)  $\delta$ : 7.25 (dd,  $J = 7.9, 7.9$  Hz, 1H), 7.13 (d,  $J = 7.5$  Hz, 1H), 7.05 (s, 1H), 6.94 (d,  $J = 8.4$  Hz, 1H), 3.81 (s, 6H). <sup>13</sup>C NMR (75 MHz, CDCl<sub>3</sub>)  $\delta$ : 159.48, 129.68, 125.23, 122.87, 117.27, 116.19, 81.67, 73.82, 55.45. IR ( $\nu$ , cm<sup>-1</sup>): 683, 779, 1050, 1150, 1220, 1290, 1460, 1490, 1590, 2150, 2830, 2940, 2960. GC-MS ( $m/z$ , M<sup>+</sup> 262), major peaks found: 262 (100%), 219 (20%), 176 (20%), 150 (9%).



**1,4-Di(pyridin-3-yl)buta-1,3-diyne (9d).**<sup>25</sup> Yield: 67%. <sup>1</sup>H NMR (300 MHz, CDCl<sub>3</sub>)  $\delta$ : 8.77 (d,  $J = 2.2$  Hz, 1H), 8.60 (dd,  $J = 4.9, 1.7$  Hz, 1H), 7.82 (ddd,  $J = 7.9, 2.0, 2.0$  Hz, 1H), 7.30 (dd,  $J = 4.9, 7.9$  Hz, 1H). <sup>13</sup>C NMR (75 MHz, CDCl<sub>3</sub>)  $\delta$ : 153.31, 149.65, 139.54, 123.24, 119.03, 79.32, 77.36. IR ( $\nu$ , cm<sup>-1</sup>): 696, 802, 1410, 2920. GC-MS ( $m/z$ , M<sup>+</sup> 204), major peaks found: 204 (100%), 176 (9%), 151 (20%), 122 (8%), 98 (20%), 74 (9%).

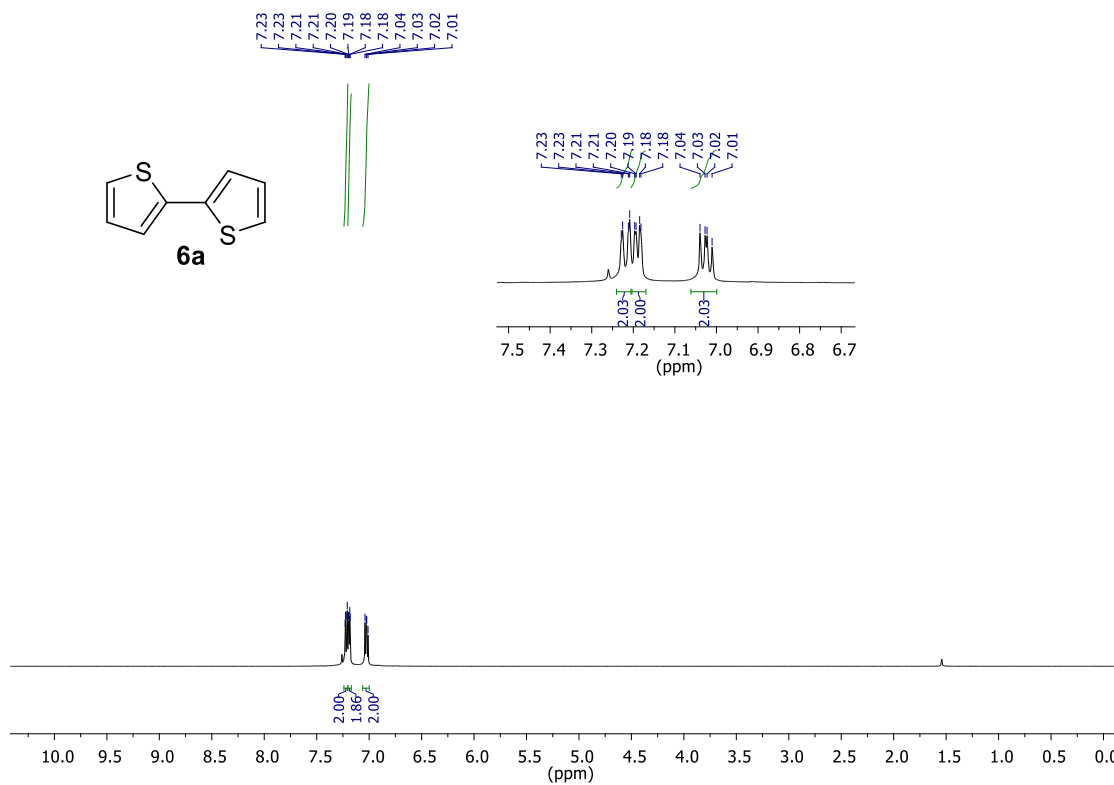


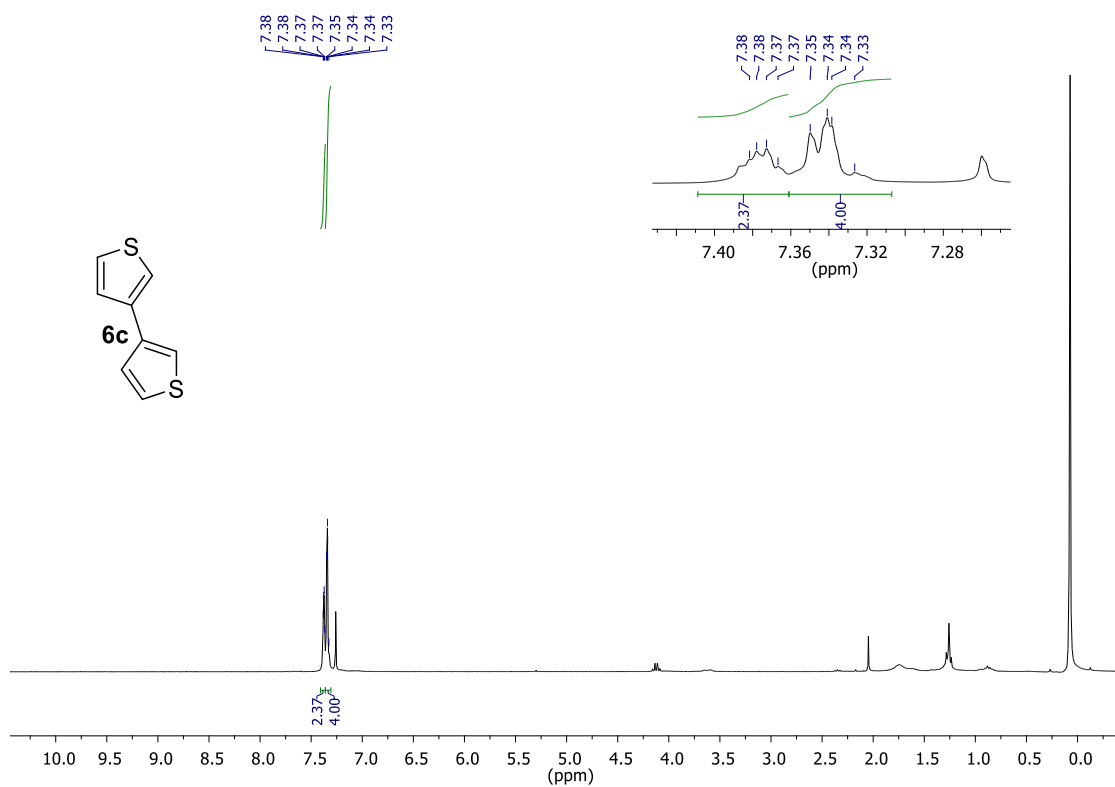
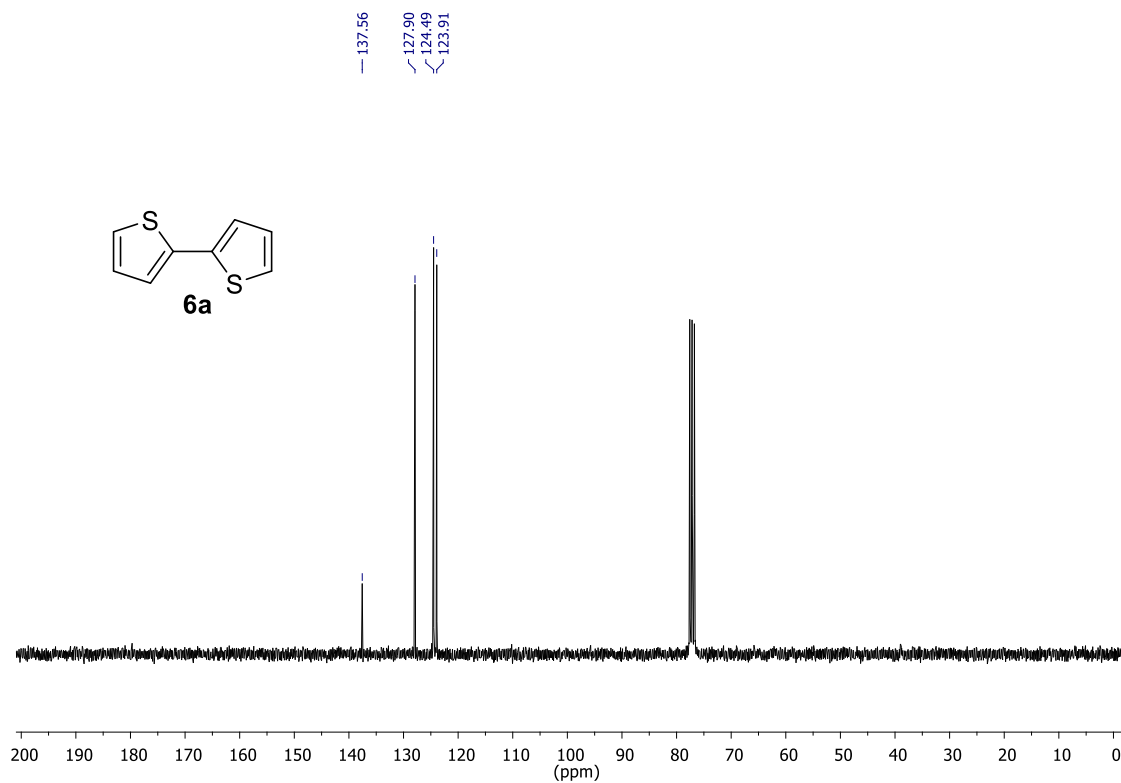
**Hexadeca-7,9-diyne (9e).**<sup>27</sup> Yield: 33%. <sup>1</sup>H NMR (300 MHz, CDCl<sub>3</sub>)  $\delta$ : 2.24 (t,  $J = 6.9$  Hz, 4H), 1.57 – 1.45 (m, 4H), 1.43 – 1.34 (m, 4H), 1.34 – 1.21 (m, 8H), 0.88 (t,  $J = 6.7$  Hz, 3H). <sup>13</sup>C NMR (75 MHz, CDCl<sub>3</sub>)  $\delta$ : 77.67, 65.42, 31.45, 28.67, 28.48, 22.65, 19.36, 14.16. IR ( $\nu$ , cm<sup>-1</sup>): 748, 913, 2930. GC-MS ( $m/z$ , M<sup>+</sup> 218), major peaks found: 218 (0.1%), 189 (10%), 147 (10%), 119 (41%), 91 (100%), 67 (40%), 41 (36%).

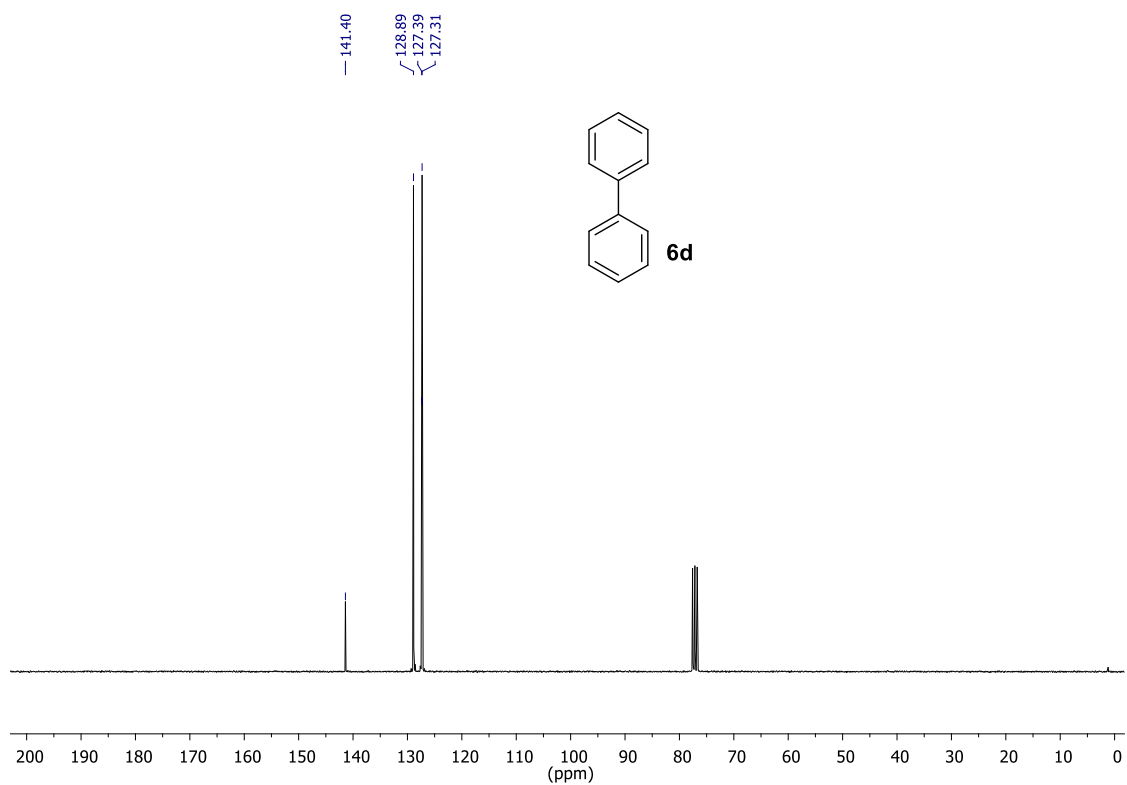
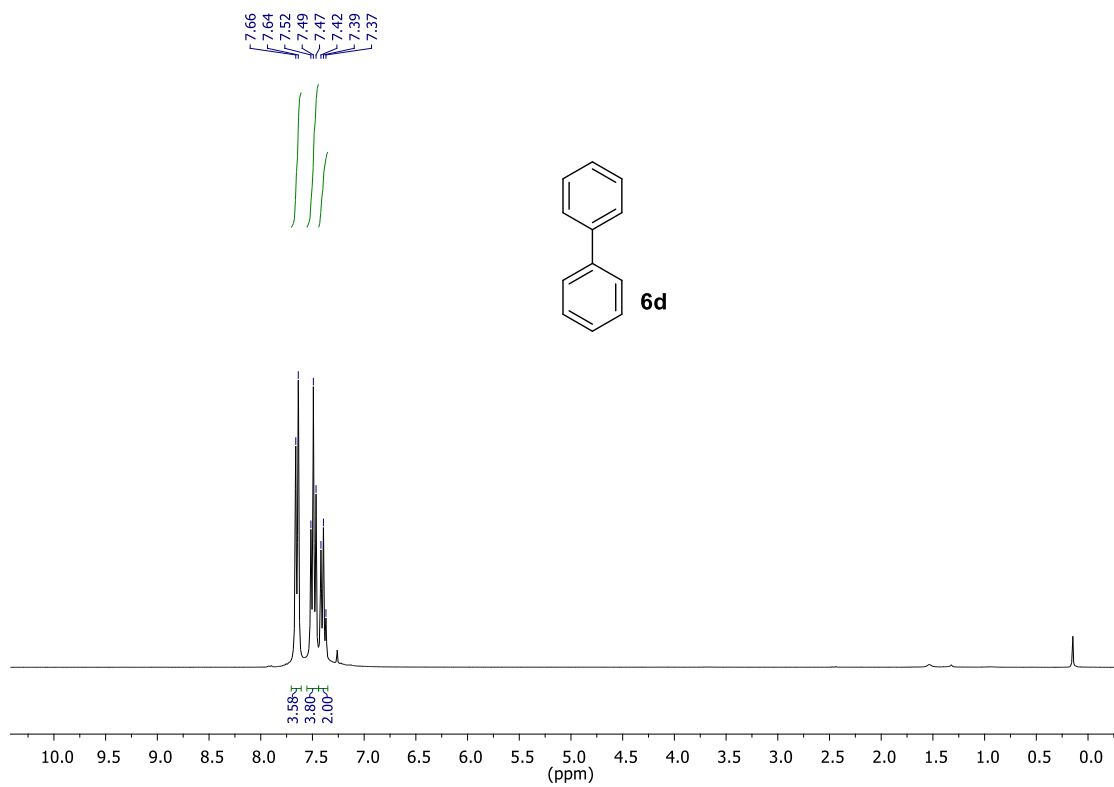


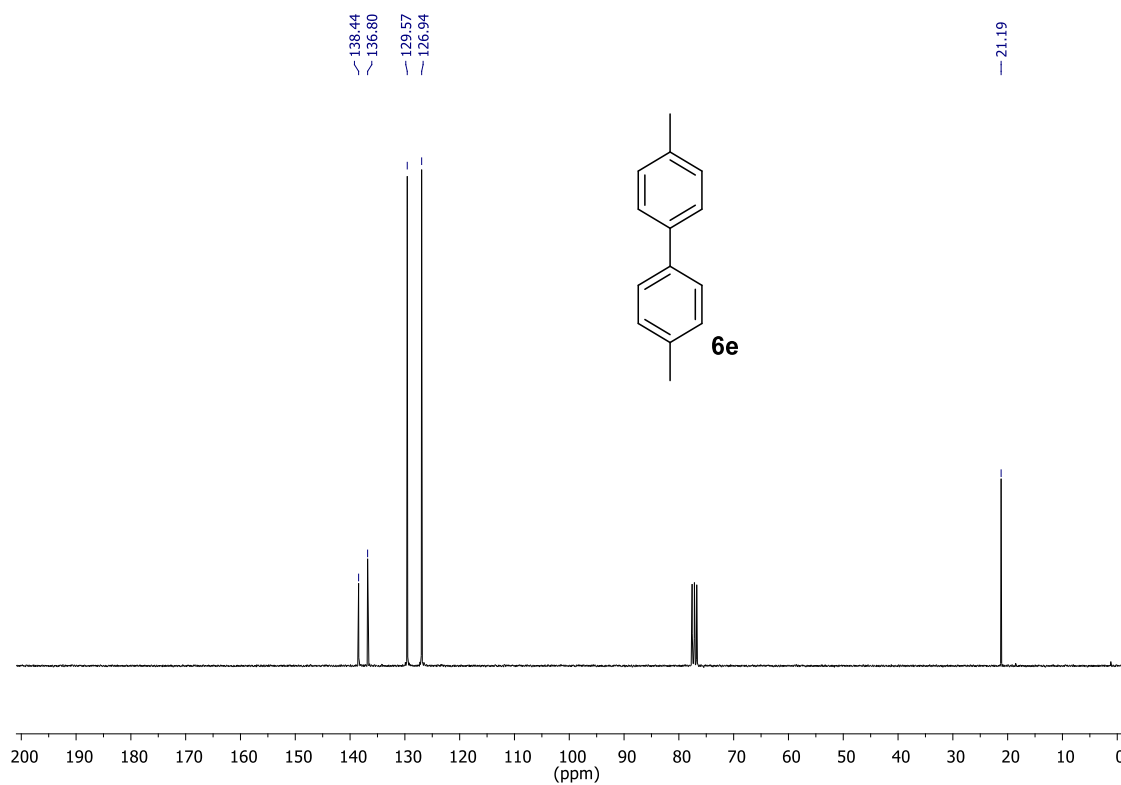
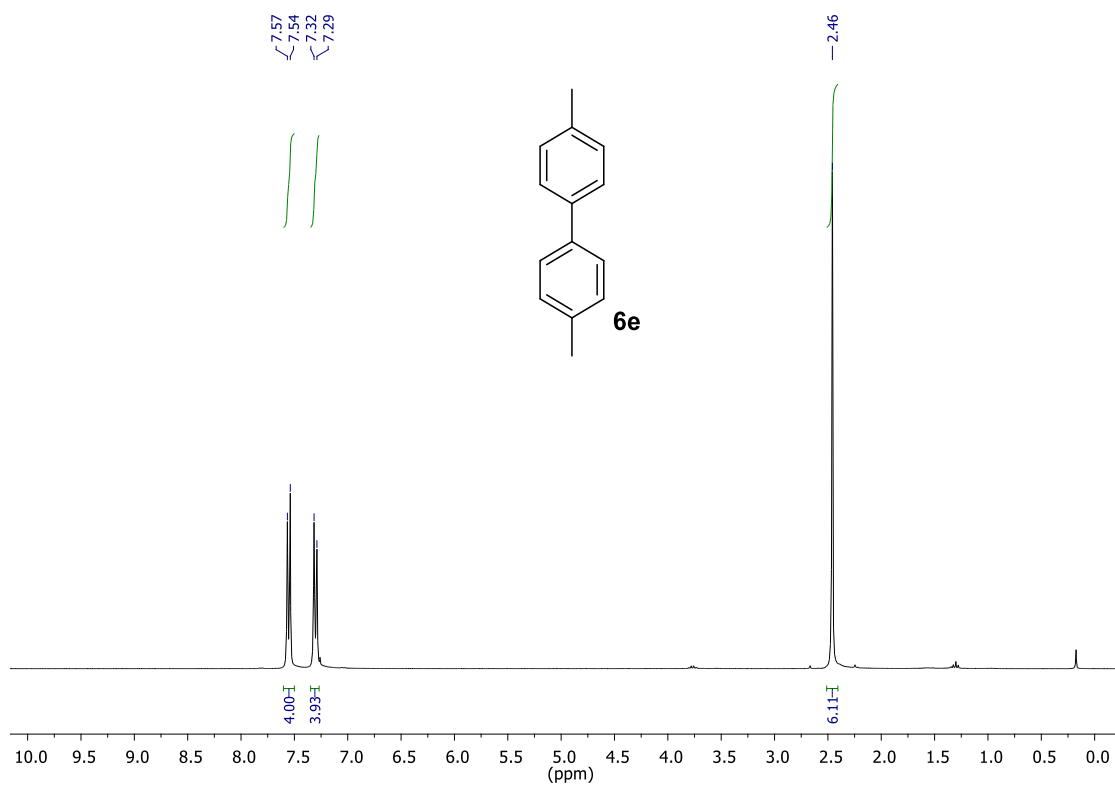
**2-(Phenylethynyl)thiophene (10a).**<sup>28</sup> Yield: 27%. <sup>1</sup>H NMR (300 MHz, CD<sub>3</sub>CN)  $\delta$ : 7.58 – 7.50 (m, 1H), 7.44 – 7.37 (m, 5H), 7.32 (dd,  $J$  = 3.6, 1.1 Hz, 1H), 7.06 (dd,  $J$  = 5.2, 3.7 Hz, 1H). <sup>13</sup>C NMR (75 MHz, CD<sub>3</sub>CN)  $\delta$ : 133.42, 132.22, 130.71, 129.68, 129.09, 128.55, 123.70, 123.57, 82.55. GC-MS ( $m/z$ , M<sup>+</sup> 184), major peaks found: 184 (100%), 152 (13%), 139 (23%).

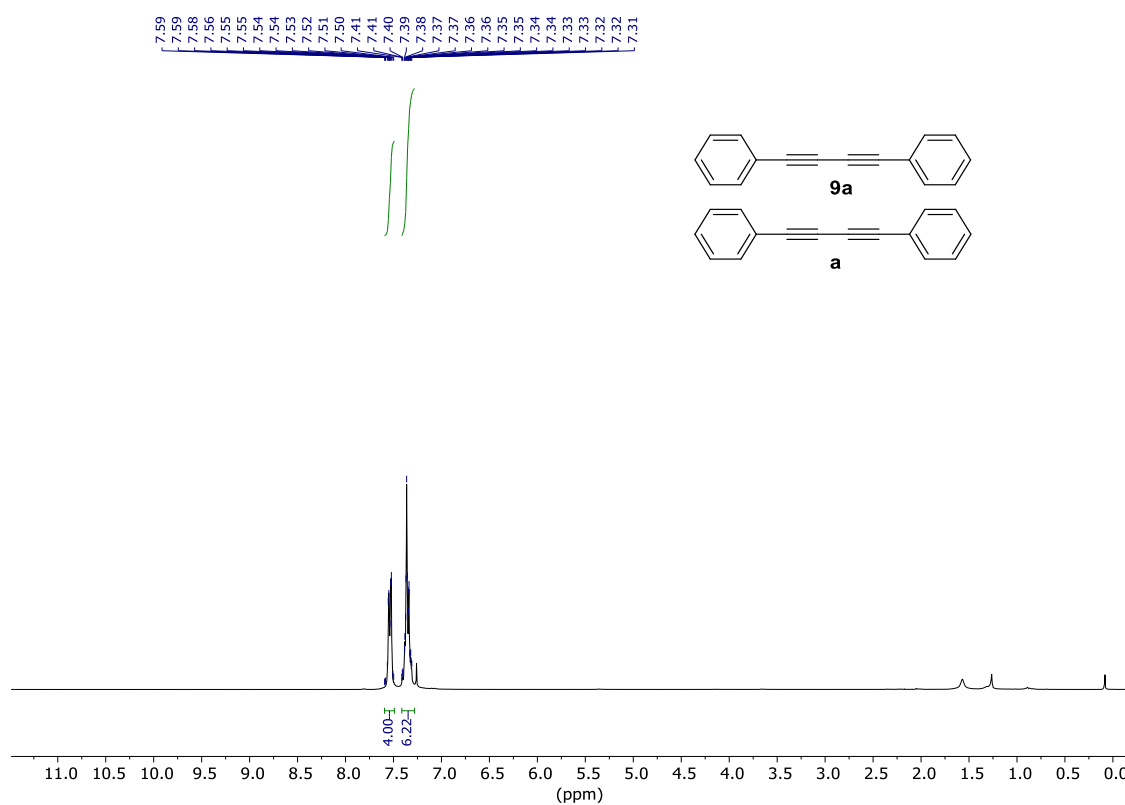
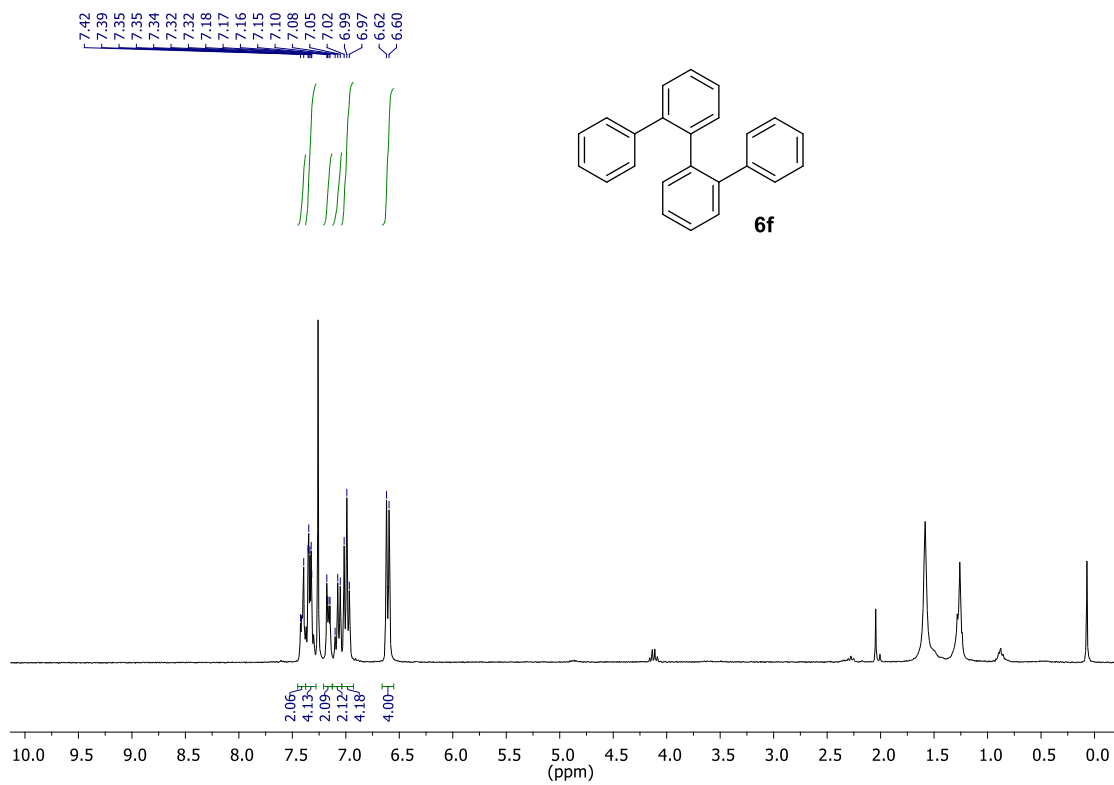
### NMR copies of the isolated compounds:

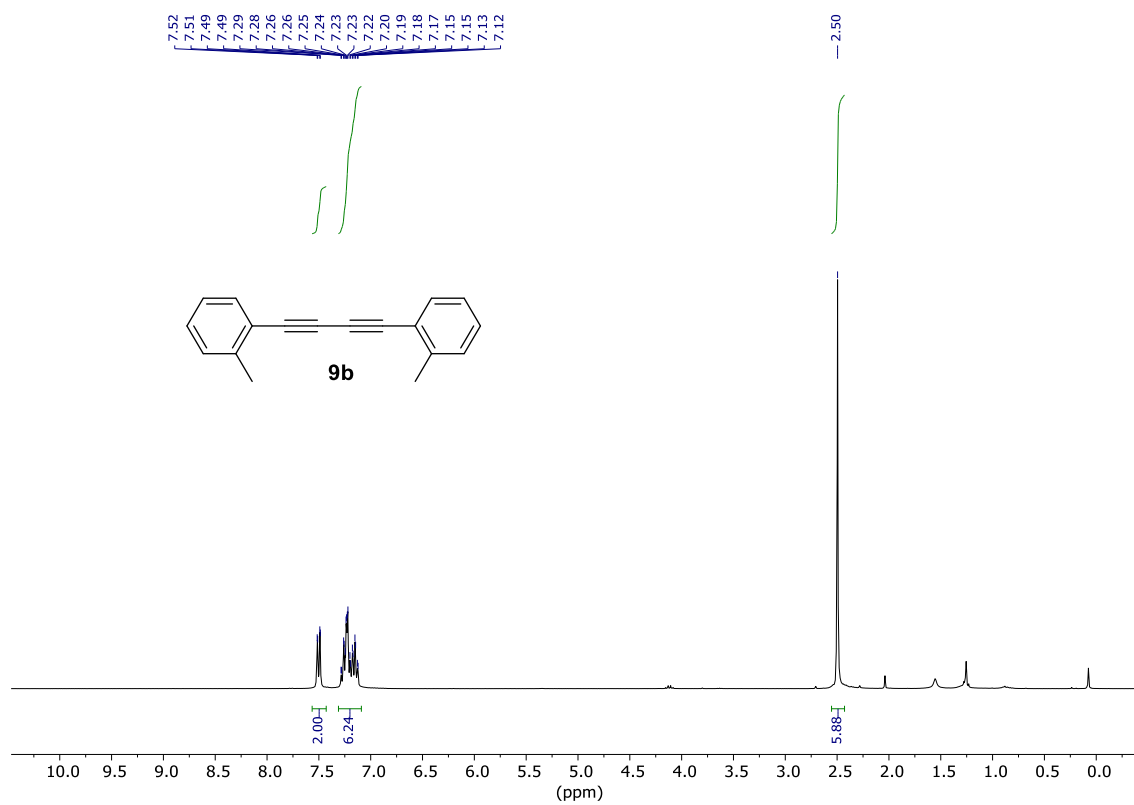
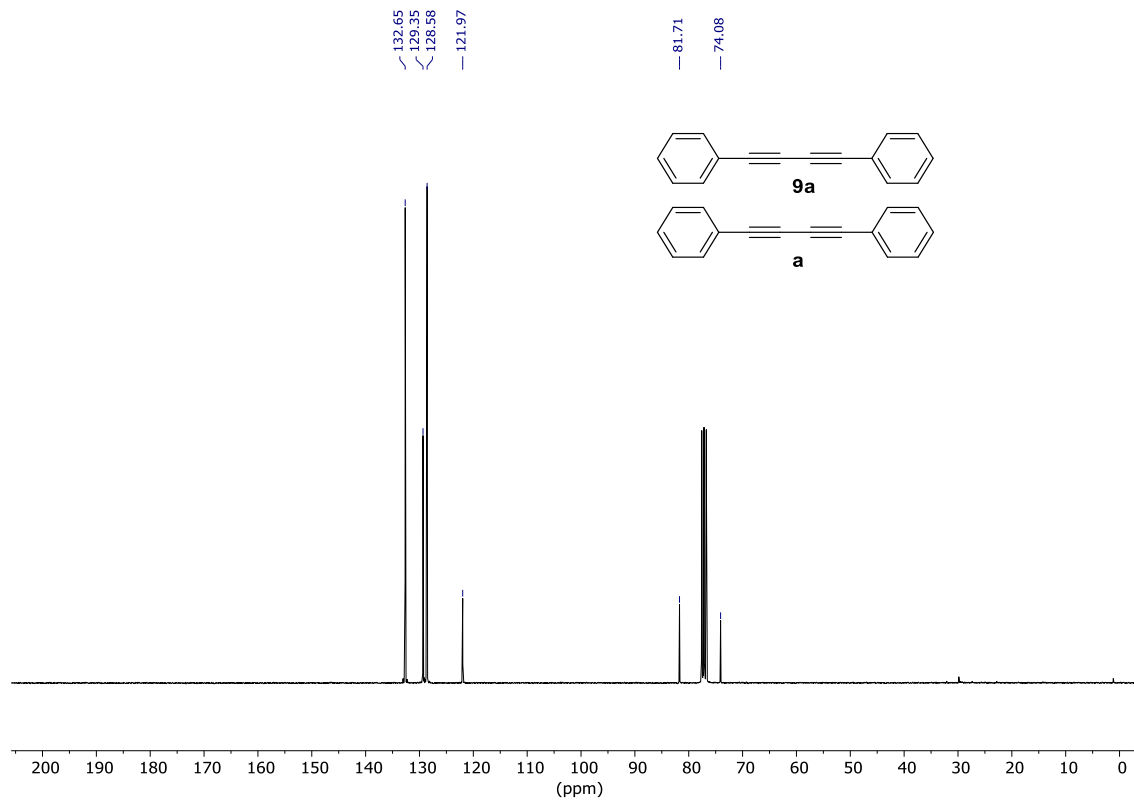


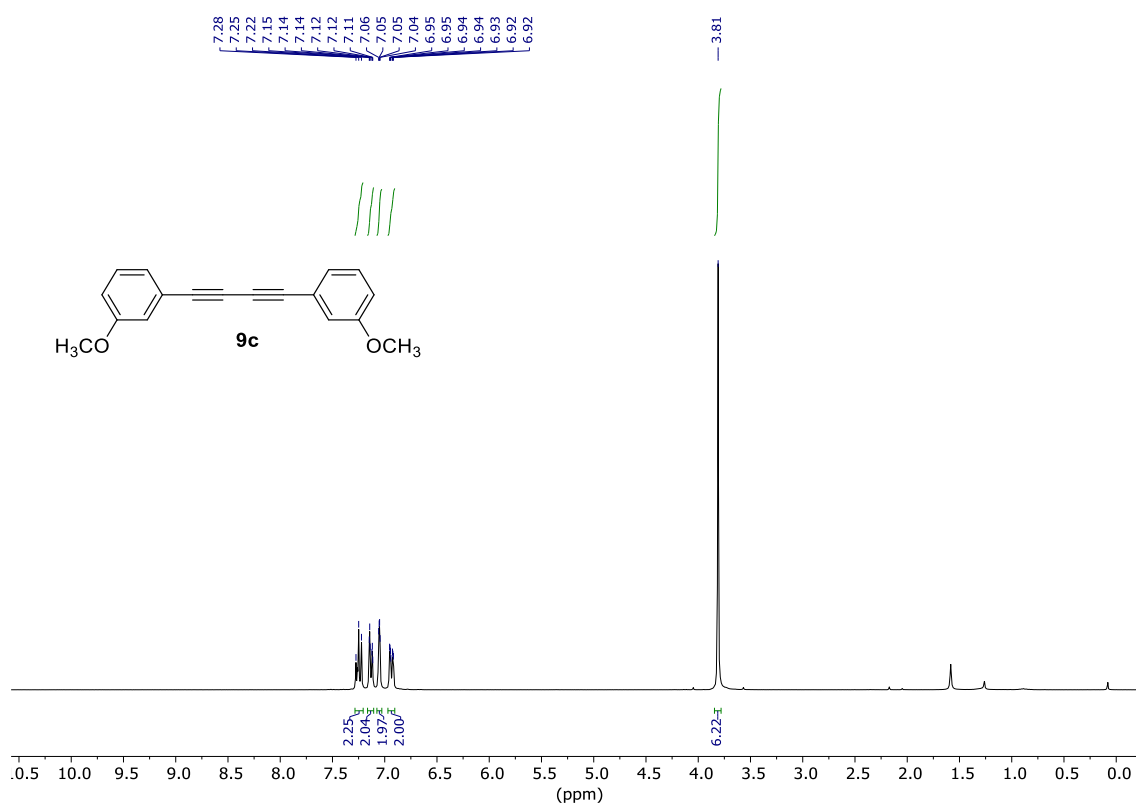
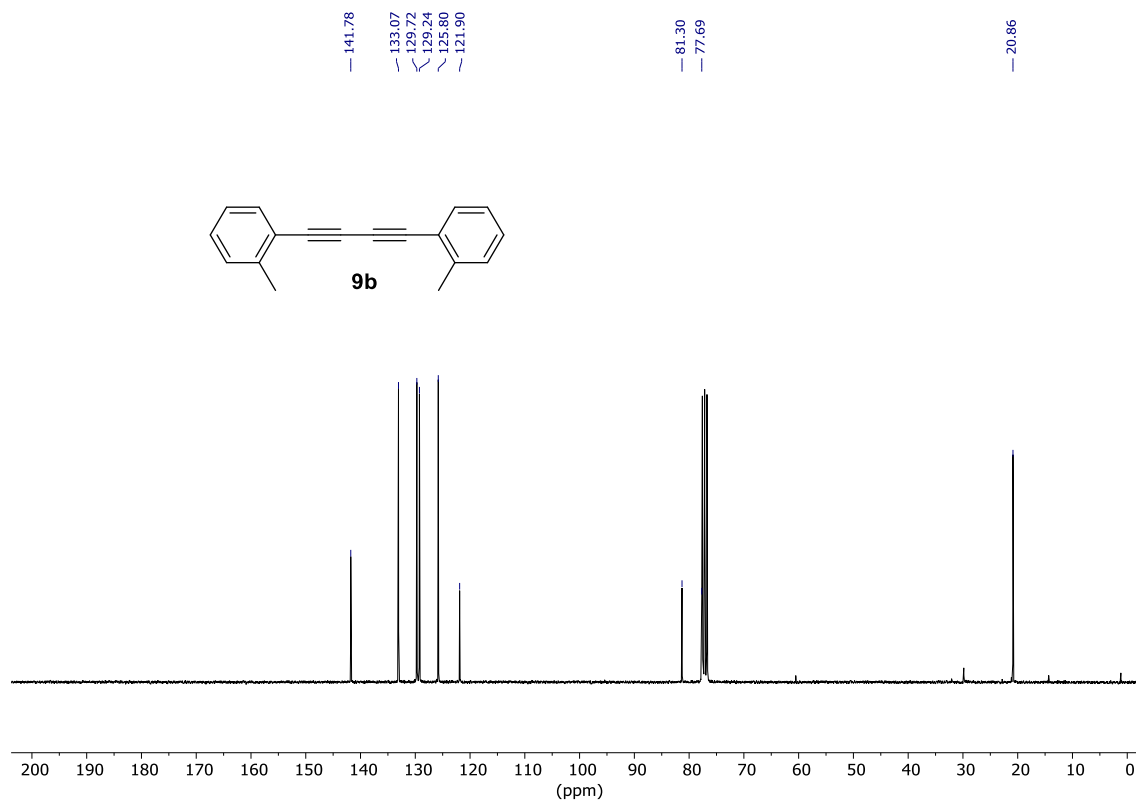


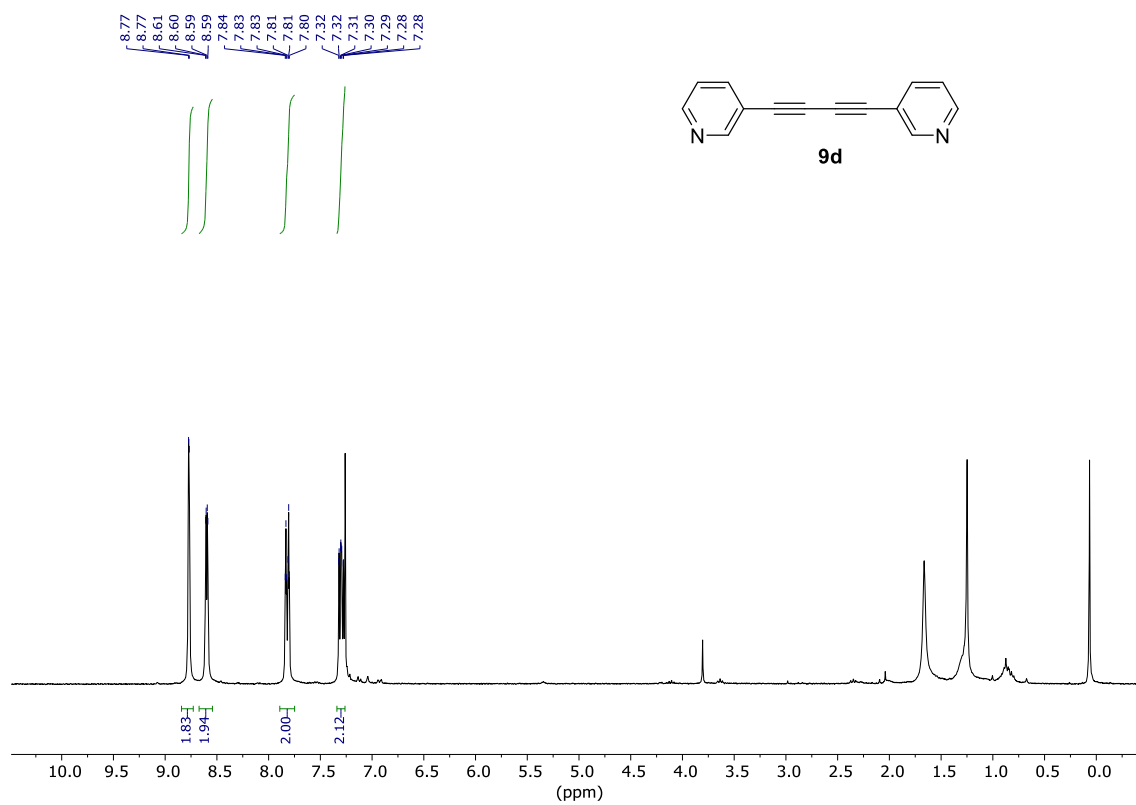
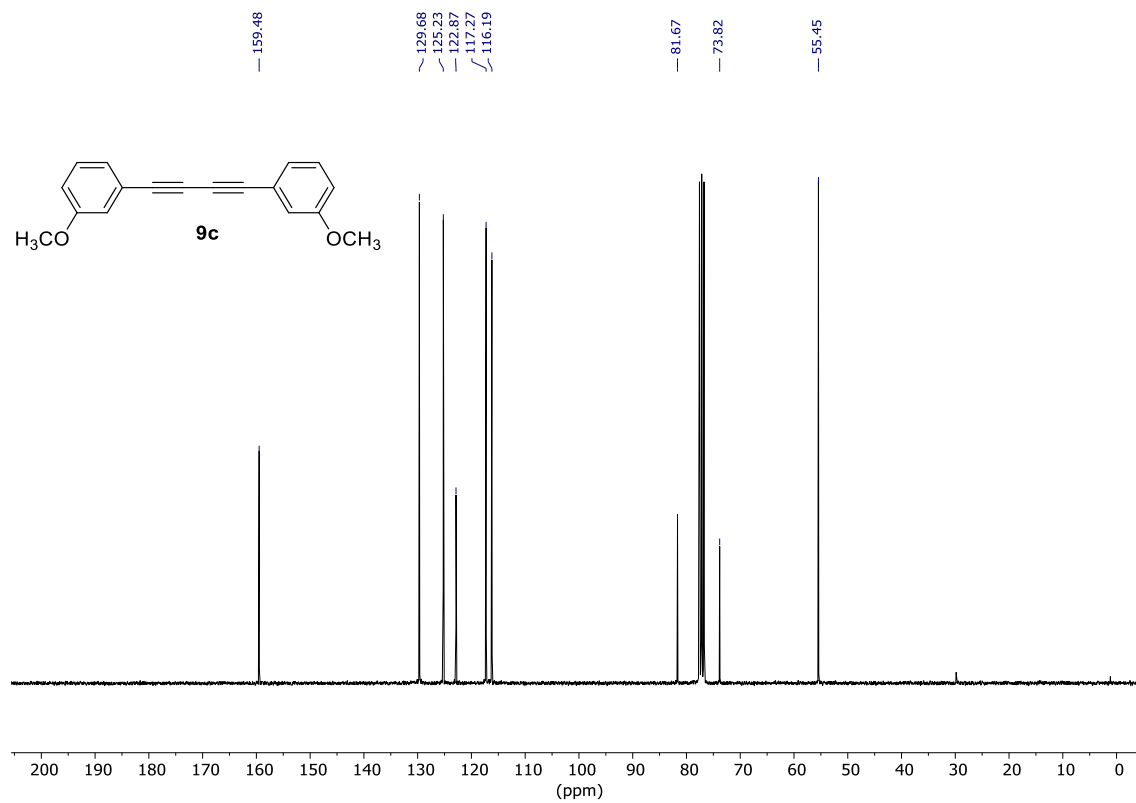


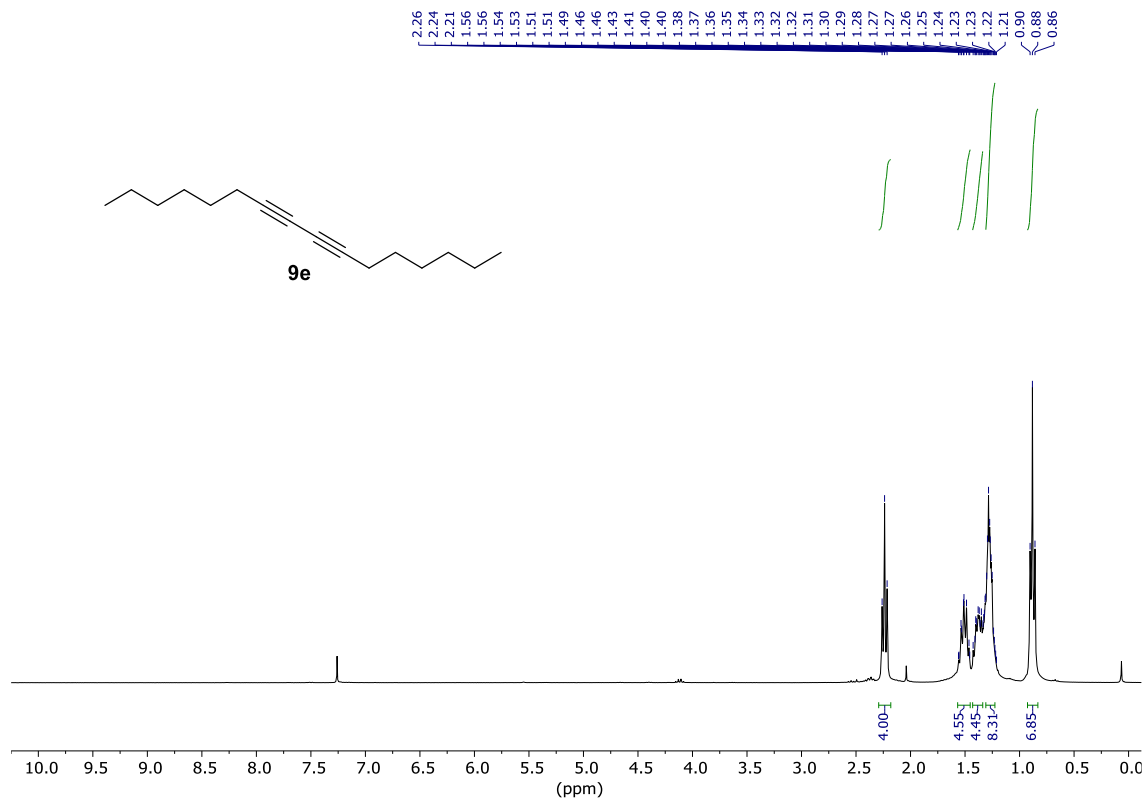
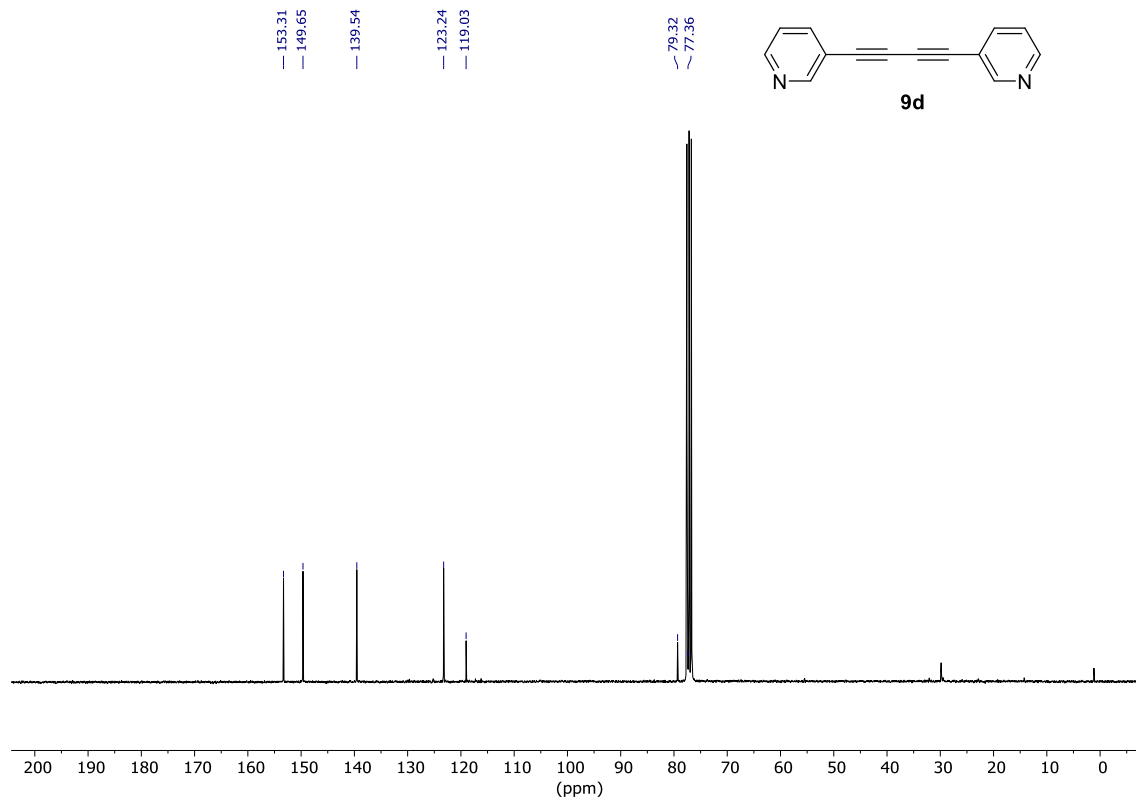












June 12<sup>th</sup> 2019

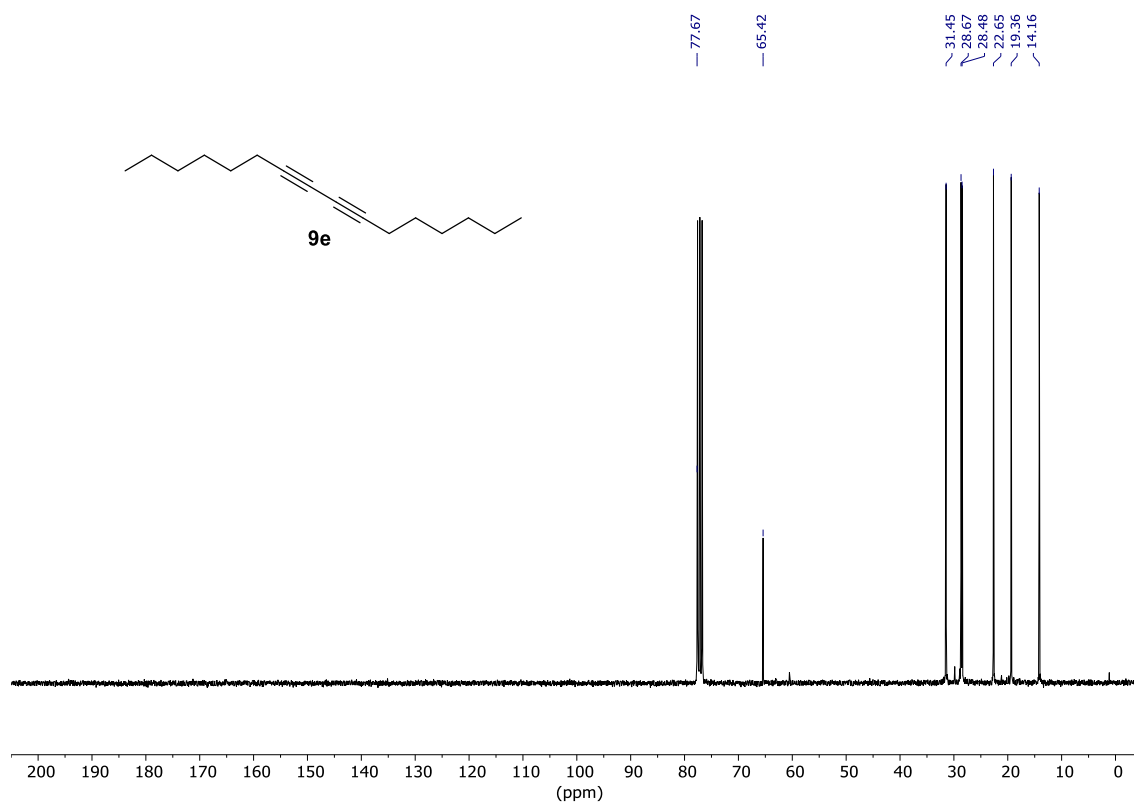


**Table S3.** Solvent study for the homocoupling of **5a**. See main text or general procedures for general reaction conditions. MeOH and CH<sub>3</sub>CN gave some activity but complete leaching of the Pd species under reaction conditions.

Entry	Solvent	Catalyst	6a (%)	7 (%)
1	Toluene	<b>2</b>	8	5
2		<b>3</b>	11	7
3	DCE	<b>2</b>	11	7
4		<b>3</b>	16	10
5	<i>o</i> -Xylene	<b>2</b>	4	2
6		<b>3</b>	5	3
7	BuOH	<b>2</b>	4	3
8		<b>3</b>	3	2
9	EtOAc	<b>2</b>	<b>24</b>	<b>54</b>
10		<b>3</b>	<b>44</b>	<b>38</b>

**Table S4.** Catalyst amount, temperature and atmosphere study for the homocoupling of **5a** catalysed by **3**. See main text or general procedures for general reaction conditions.

Entry	Mol % ( <b>3</b> )	T (°C)	Atmosphere	<b>6a</b> (%)	<b>7</b> (%)
1	2	80	N <sub>2</sub>	27	54
2	1	80	N <sub>2</sub>	23	43
3	0.5	80	N <sub>2</sub>	16	45
<b>4</b>	<b>2</b>	<b>60</b>	<b>N<sub>2</sub></b>	<b>44</b>	<b>38</b>
5	2	60	Air	20	54
6	2	60	O <sub>2</sub>	15	26
7	2	25	N <sub>2</sub>	4	20

**Table S5.** Initial rates for different amounts of benzoquinone and under different atmospheres during the homocoupling of **5a** catalyzed by SCC@MOF **3** (see main text or general procedures for general reaction conditions).

Entry	Benzoquinone (eq.)	Atmosphere	r <sub>0</sub> (%/h)
1	0	N <sub>2</sub>	7.7
2	0	Air	9.3
3	0	O <sub>2</sub>	11.7
4	0.25	N <sub>2</sub>	20.4
5	0.25	O <sub>2</sub>	7.4

**Table S6.** Initial rates for different amounts of benzoquinone and under different atmospheres during the homocoupling of **5a** catalyzed by Pd<sub>4</sub>(L<sub>1</sub>)<sub>4</sub> in CH<sub>3</sub>CN (see main text or general procedures for general reaction conditions).

Entry	Benzoquinone (eq.)	Atmosphere	r <sub>0</sub> (%/h)
1	0	N <sub>2</sub>	7.4
2	0	O <sub>2</sub>	5.7
3	2	N <sub>2</sub>	14.3
4	2	O <sub>2</sub>	18.9

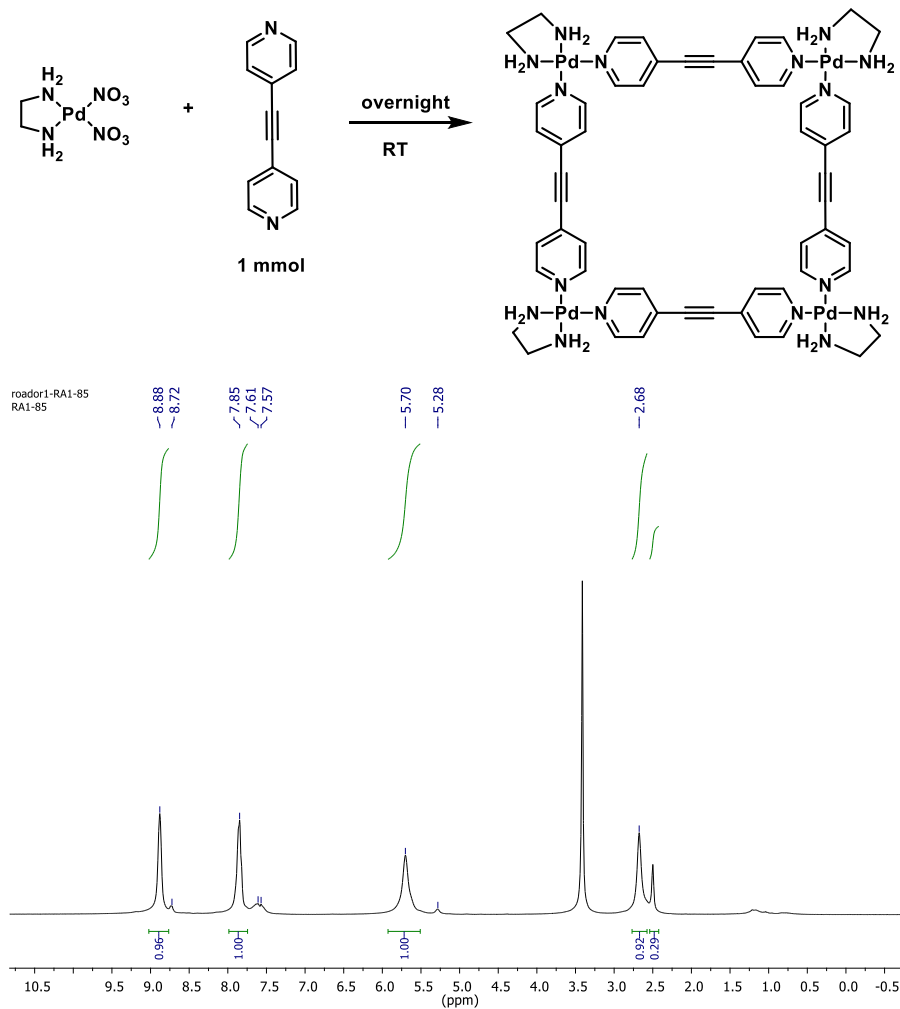


**Figure S20.** Top: Schematic representation of the synthesis of known soluble Pd<sub>4</sub>(L<sub>1</sub>)<sub>4</sub> square used as control for the catalytic experiments. Bottom: The corresponding <sup>1</sup>H NMR (DMSO-d<sub>6</sub>) spectrum. The <sup>1</sup>H NMR spectra is the same in THF-d<sub>8</sub>, D<sub>2</sub>O and AcN-d<sub>3</sub>.

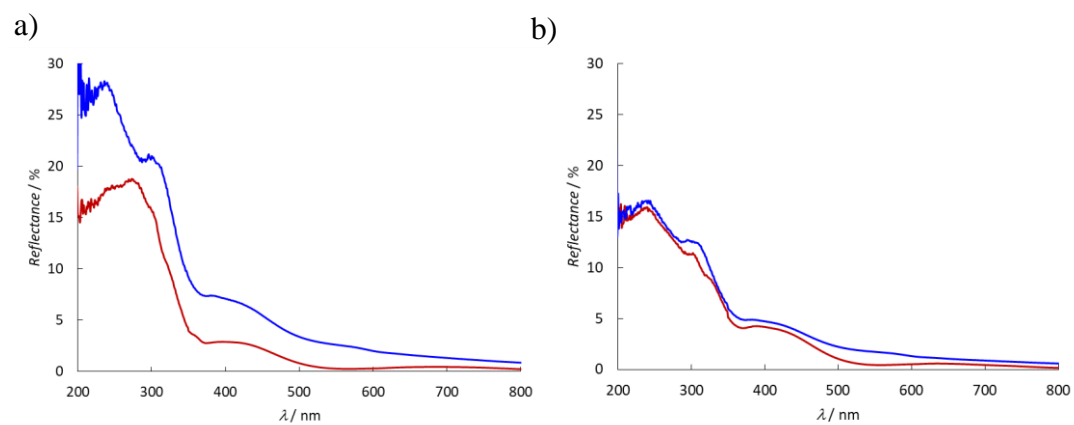


**Figure S21.** Diffuse-reflectance UV-Vis spectrum of SCCs@MOFs **2** (a) and **3** (b) before (red) and after reaction with thienylboronic acid **5a** (blue). See main text for reaction conditions.

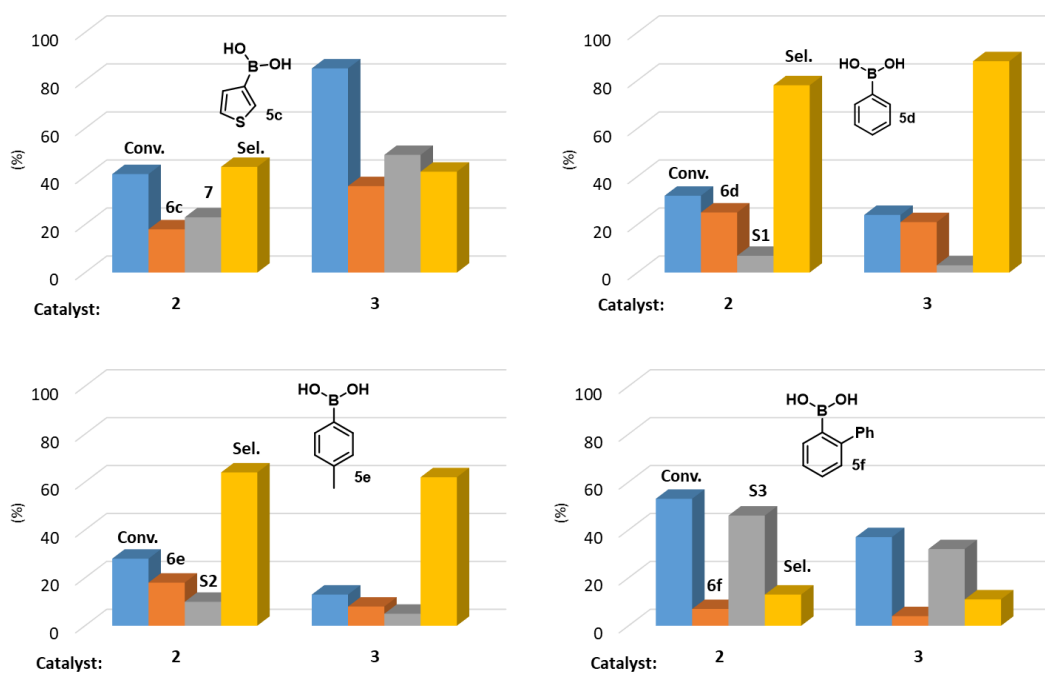


**Figure S22.** Catalytic results for the homocoupling of boronic acids **5c-f** catalyzed by SCCs@MOFs **2** and **3**, see main text and general procedures for reaction conditions, (**5d-g** were coupled in *o*-xylene instead of EtOAc solvent). **S1**: benzene, **S2**: toluene and **S3**: biphenyl.

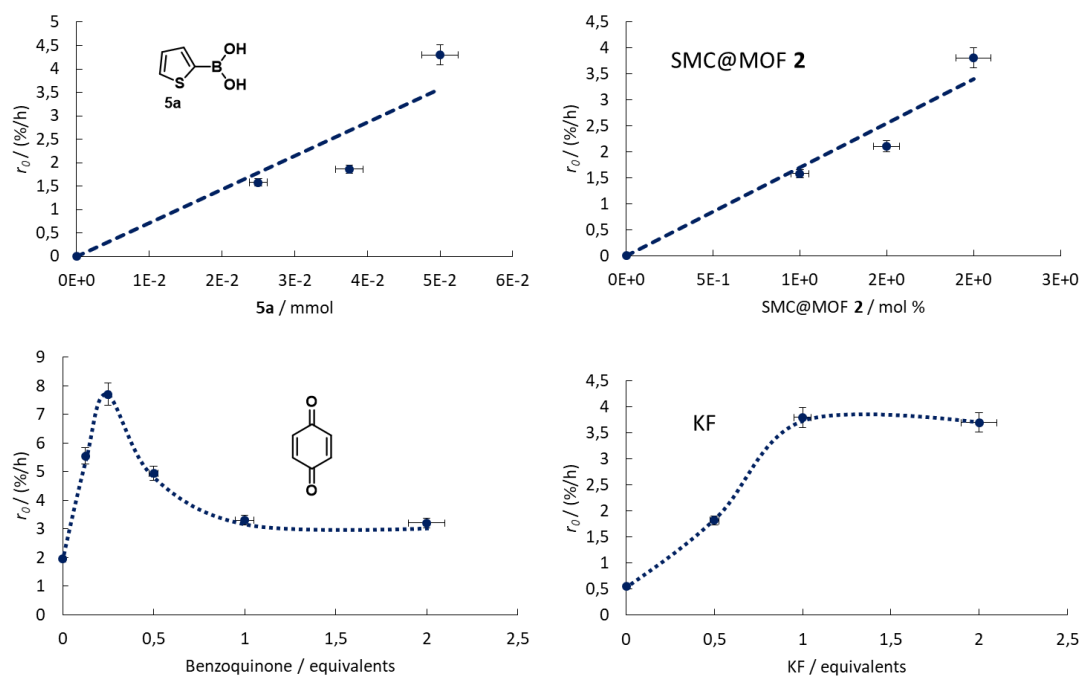


**Figure S23.** Initial rates vs. amount of the different reagents for the homocoupling of **5a** catalyzed by SCC@MOF **2** (see main text for general reaction conditions). Error bars account for 5% uncertainty.

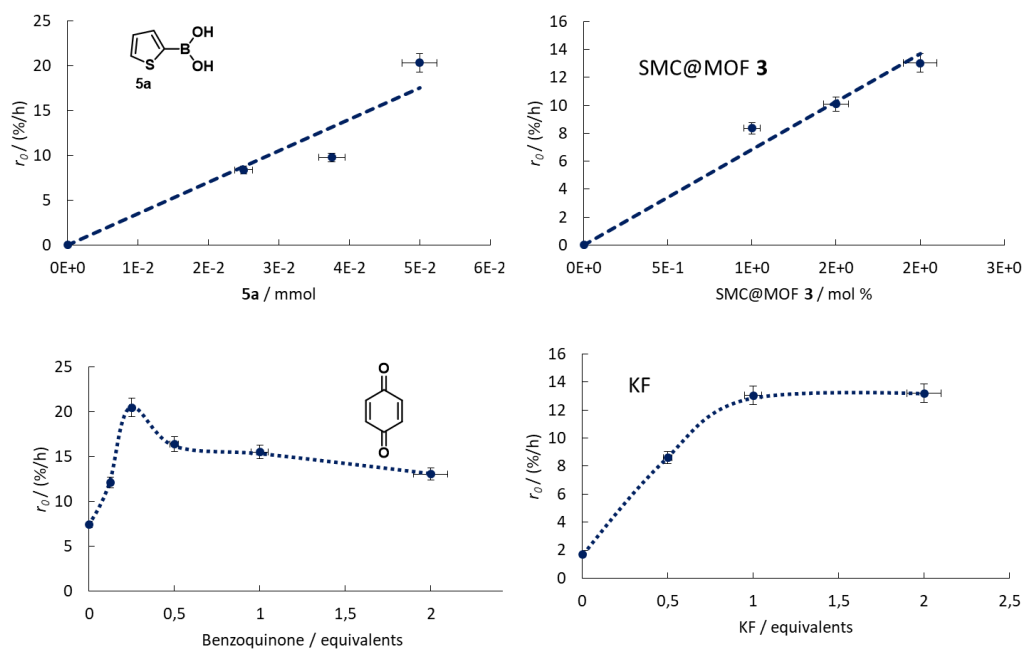


**Figure S24.** Initial rates *vs.* amount of the different reagents for the homocoupling of **5a** catalyzed by SMC@MOF **3** (see main text for general reaction conditions). Error bars account for 5% uncertainty.

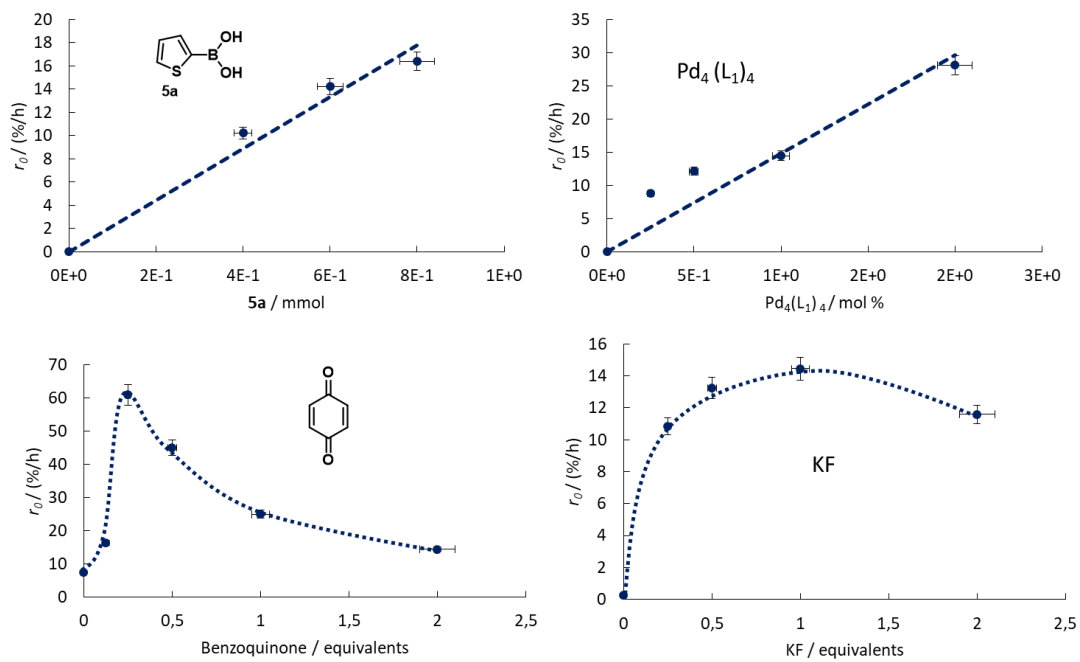


**Figure S25.** Initial rates vs. amount of the different reagents for the homocoupling of **5a** catalyzed by  $\text{Pd}_4(\text{L}_1)_4$  in  $\text{CH}_3\text{CN}$  (see main text for general reaction conditions). See ahead for fitting Pd order. Error bars account for 5% uncertainty.

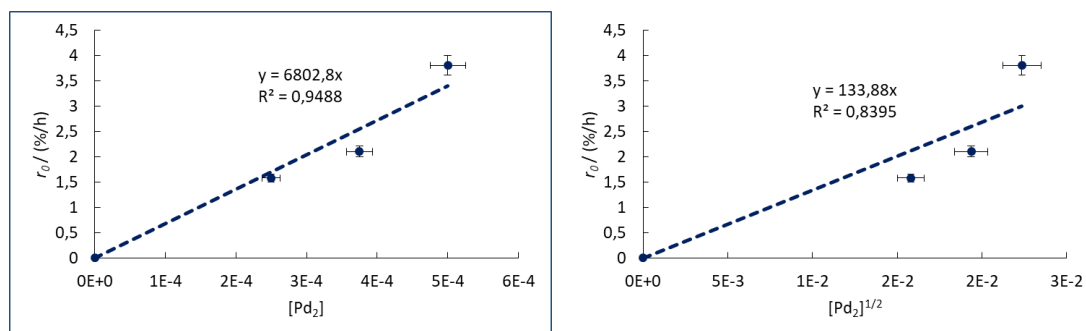


**Figure S26.** Initial rates *vs.* concentration of  $[Pd_2]$  dimers in SCC@MOF **2** to the power of different squares, represented to evaluate the possible dissociation of Pd atoms during reaction (see main text for general reaction conditions). Data are fitted to a linear regression. Error bars account for 5% uncertainty.

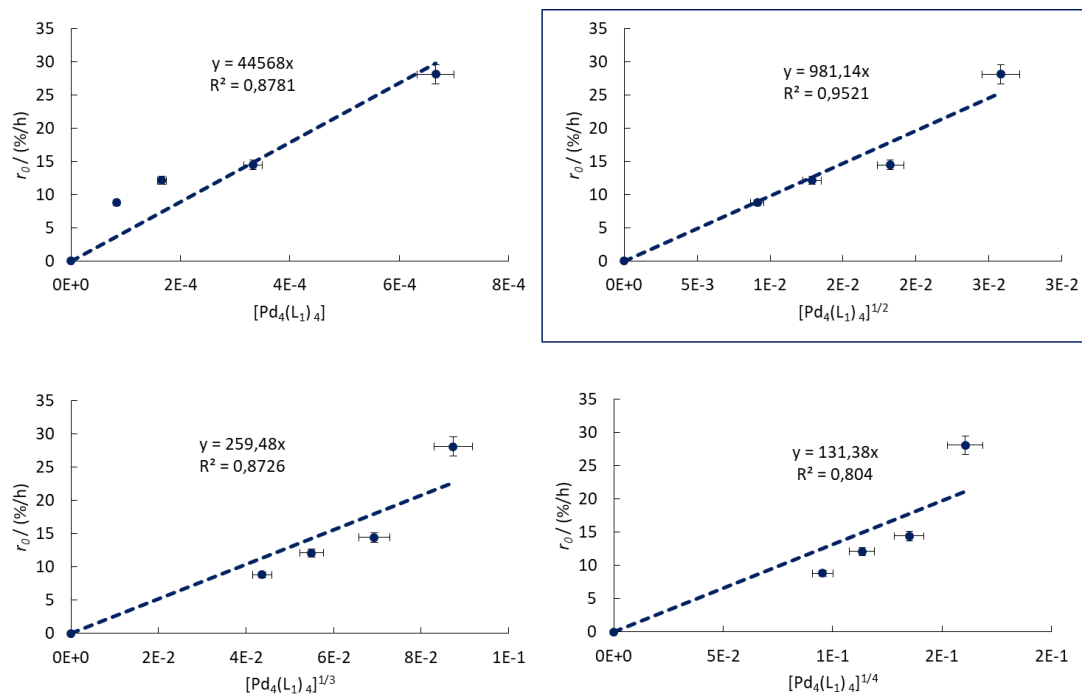


**Figure S27.** Initial rates vs. concentration of  $\text{Pd}_4(\text{L}_1)_4$  in  $\text{CH}_3\text{CN}$  to the power of different squares, represented to evaluate the possible dissociation of Pd atoms during reaction (see main text for general reaction conditions). Data are fitted to a linear regression. Error bars account for 5% uncertainty.

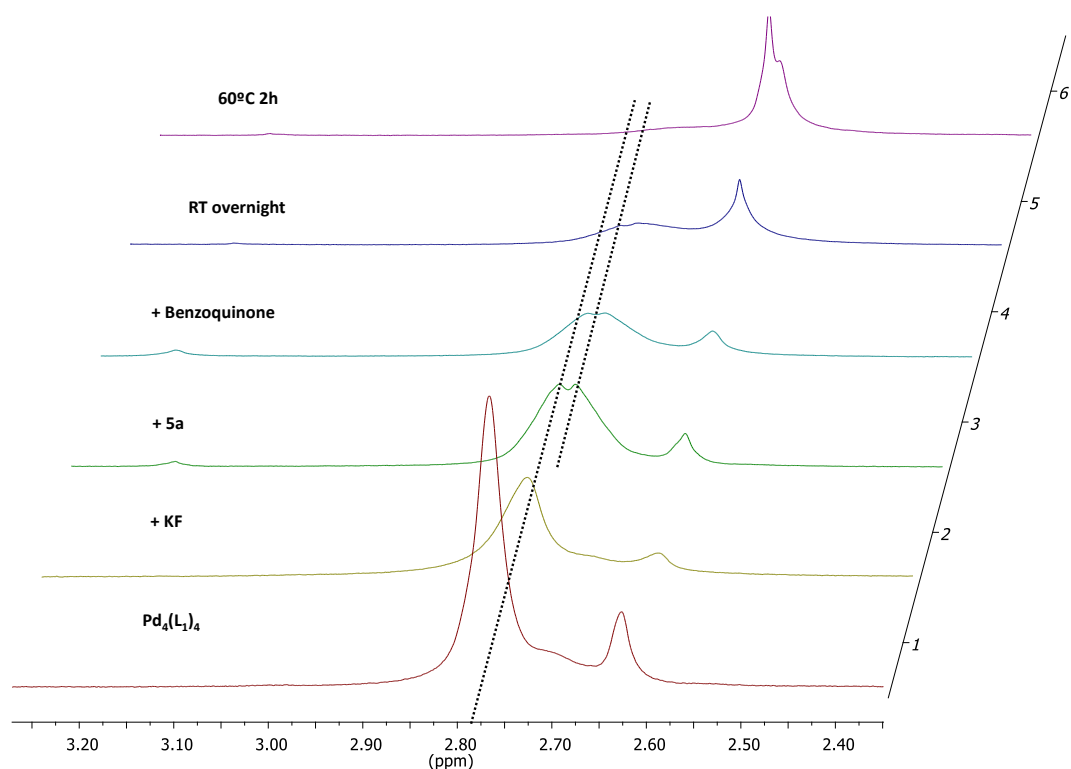
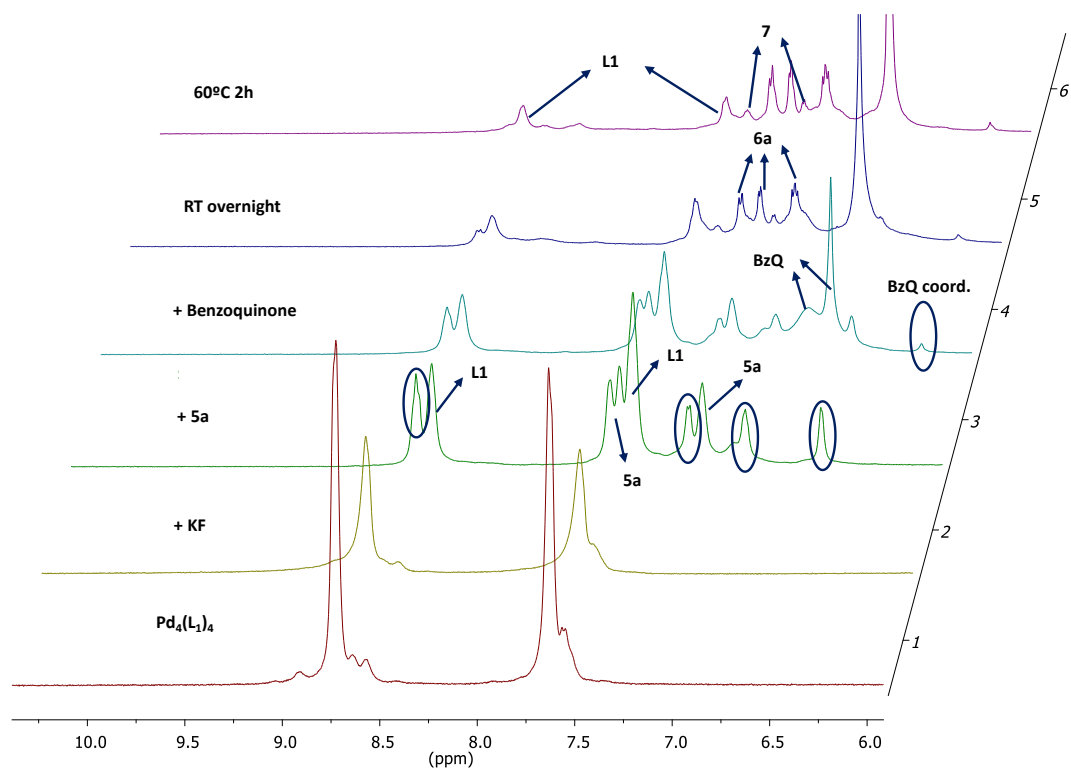


**Figure S28.** Aromatic area (top) and alkyl area (bottom) of the  $^1\text{H}$  NMR spectra of  $\text{Pd}_4(\text{L}_1)_4$  in  $\text{CD}_3\text{CN}$  after sequential addition of all the reagents for the homocoupling of **5a**. Unidentified intermediate species are marked with a circle.

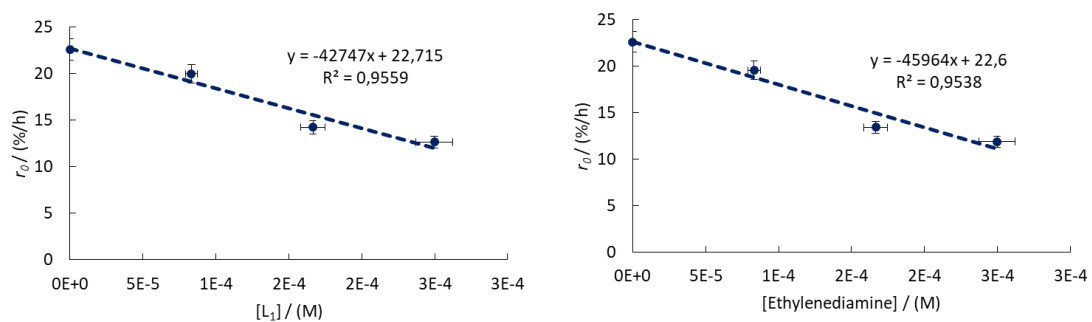


**Figure S29.** Initial rates vs. concentration of added ligands  $L_1$  (left) and ethylenediamine (right) for the homocoupling of **5a** with  $Pd_4(L_1)_4$  as a catalyst in  $CH_3CN$  (see main text for general reaction conditions). Data are adjusted to a linear regression. Error bars account for 5% uncertainty.

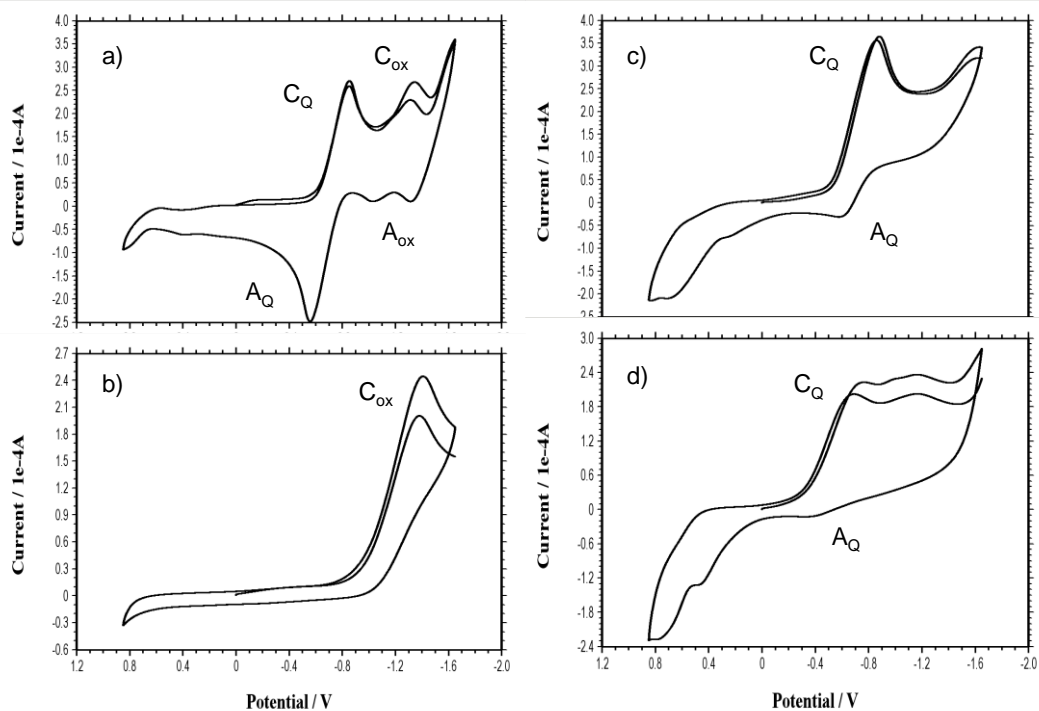


**Figure S30.** Cyclic voltammograms at glassy carbon electrode of air-saturated 0.10 M Bu<sub>4</sub>NPF<sub>6</sub>/MeCN solutions of: a) 5 mM benzoquinone; b) 5 mM **5a**; c) 5 mM benzoquinone + 5 mM **5a** + 5 mM NaF; d) the above solution plus 1 mM Pd(II) acetate. Potential scan rate 500 mV s<sup>-1</sup>.

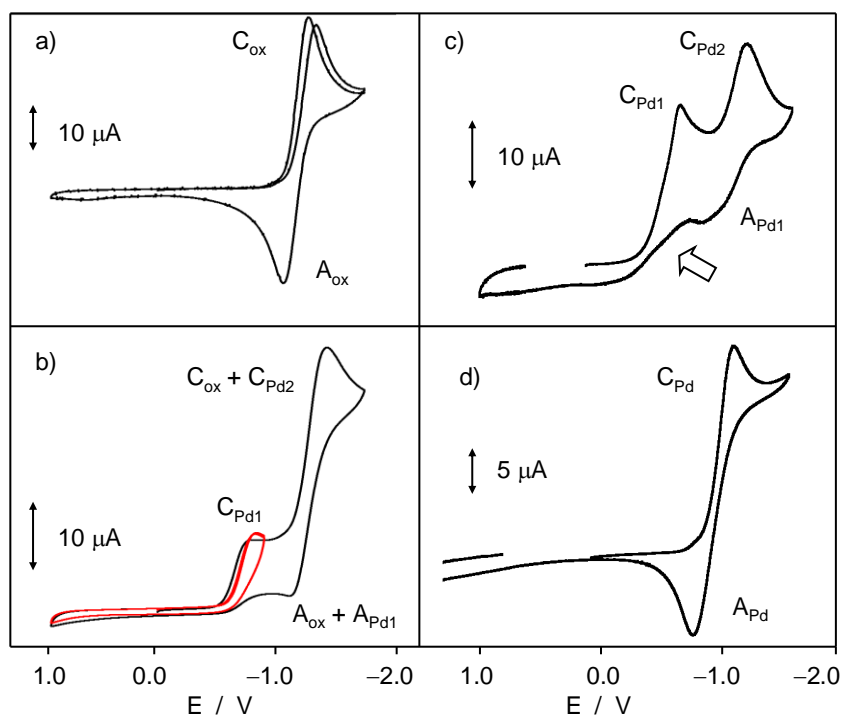


**Figure S31.** Cyclic voltammograms at glassy carbon electrode of: a) air-saturated 0.10 M  $\text{Bu}_4\text{NPF}_6/\text{MeCN}$ ; b) the same solution plus 0.5 mM Pd(II) acetate (voltammograms at two switching potentials are superimposed); c) 0.5 mM Pd(II) acetate solution in 0.10 M  $\text{Bu}_4\text{NPF}_6/\text{MeCN}$ ; d) 0.2 mM solution of  $\text{Pd}_4(\text{L}_1)_4$  complex in 0.10 M  $\text{Bu}_4\text{NPF}_6/\text{MeCN}$ . Potential scan rate  $50 \text{ mV s}^{-1}$ . The arrow in Figure c marks the crossover associated to Pd(I) disproportionation (see text).  $\text{C}_{\text{Pd1}}$  is attributed to a Pd<sup>I</sup> species and  $\text{C}_{\text{Pd2}}$  to a Pd<sup>0</sup> species.

**Table S7.** Solvent study for the homocoupling of **8a** catalyzed by SCC@MOF **4**. See main text and general procedures for general reaction conditions.

<b>Entry</b>	<b>Solvent</b>	<b>Conversion 8 (%)</b>	<b>Selectivity 9a (%)</b>
<b>1</b>	<b>EtOAc</b>	<b>99</b>	<b>77</b>
2	Toluene	99	57
3	THF	67	45
4	Decane	40	54

**Table S8.** Base study for the homocoupling of **8a** catalyzed by SCC@MOF **4**. See main text and general procedures for general reaction conditions.

Entry	Base	Conversion <b>8</b> (%)	Selectivity <b>9a</b> (%)
<b>1</b>	<b>DABCO</b>	<b>99</b>	<b>77</b>
2	NBu <sub>3</sub>	72	6
3	KF	94	4

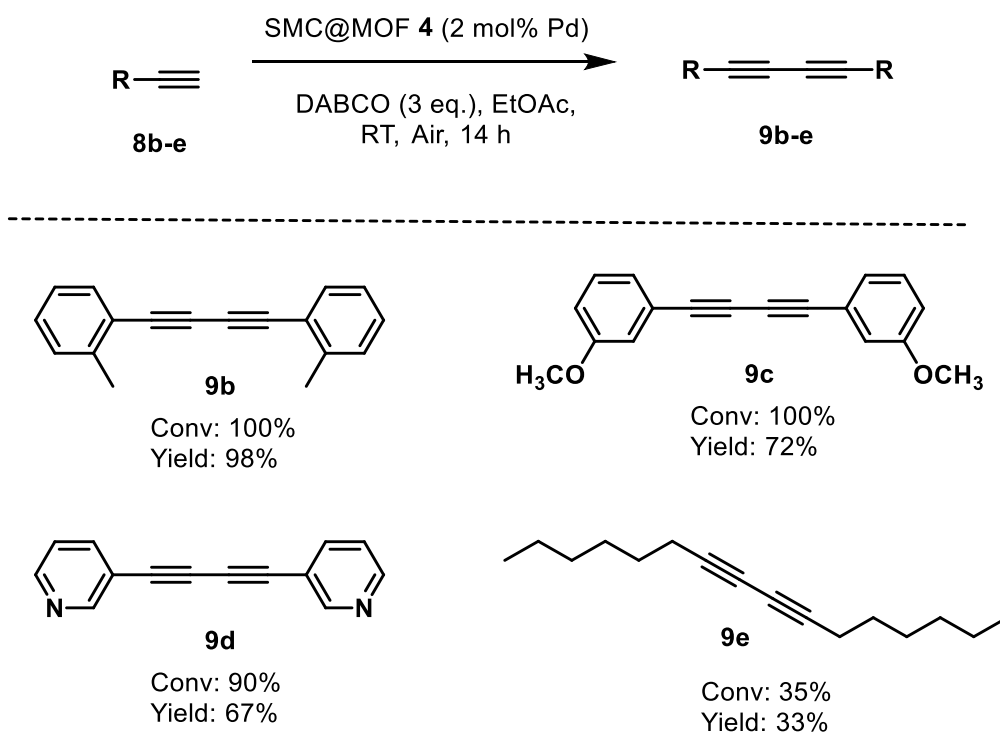


**Figure S32.** Catalytic results for the homocoupling of alkynes **8b-e** catalyzed by SMC@MOF **4** under typical reaction conditions.

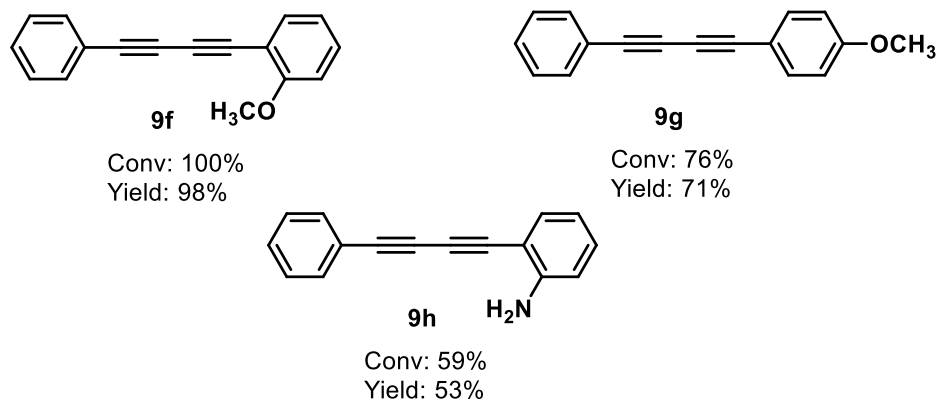
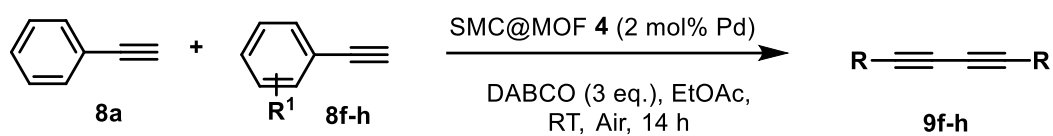


**Figure S33.** Catalytic results for the coupling of phenylacetylene **8a** with alkynes **8f-h** catalyzed by SCC@MOF **4** under typical reaction conditions using an excess of **8f-h** of 3 equivalents.

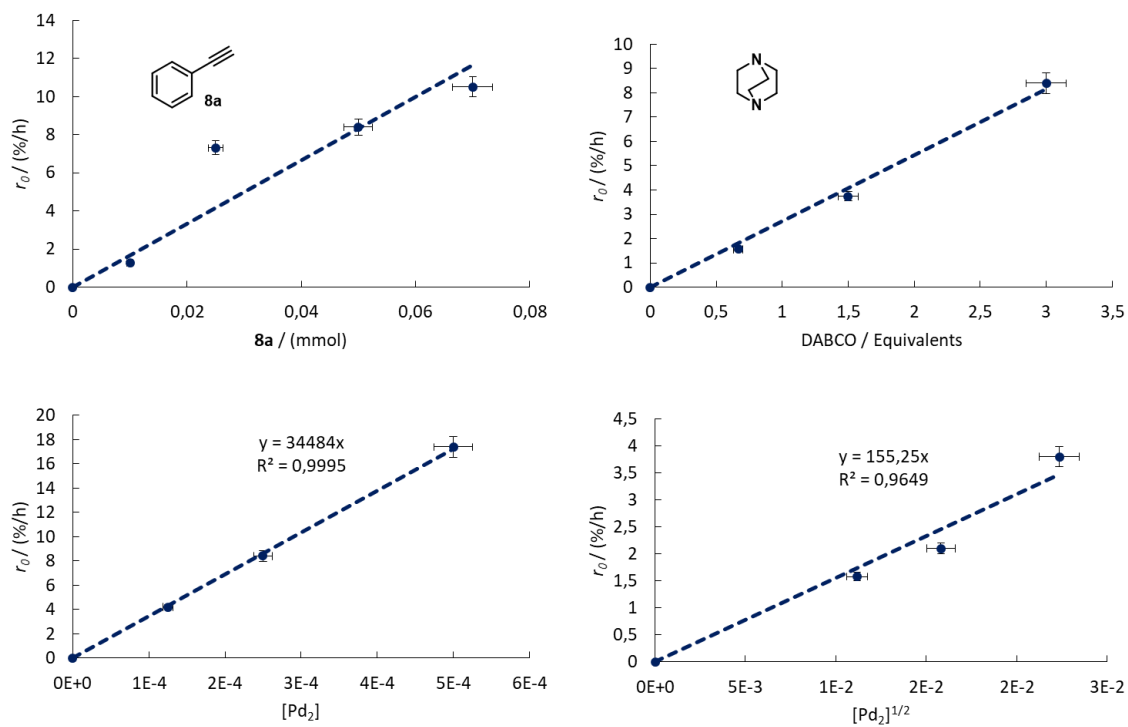


**Figure S34.** Initial rates vs. amount of the different reagents for the homocoupling of **8a** catalyzed by SCC@MOF **4** (see main text for general reaction conditions). [Pd<sub>2</sub>] dimers inside in SCC@MOF **4** fit to a first order kinetics. Data are fitted to a linear regression. Error bars account for 5% uncertainty.

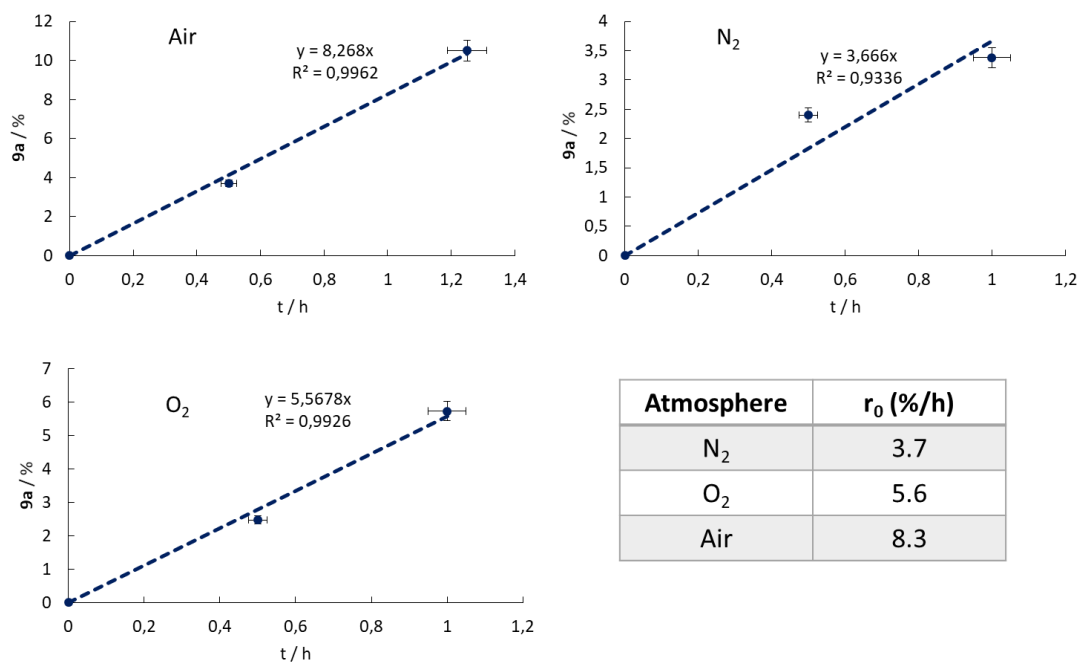
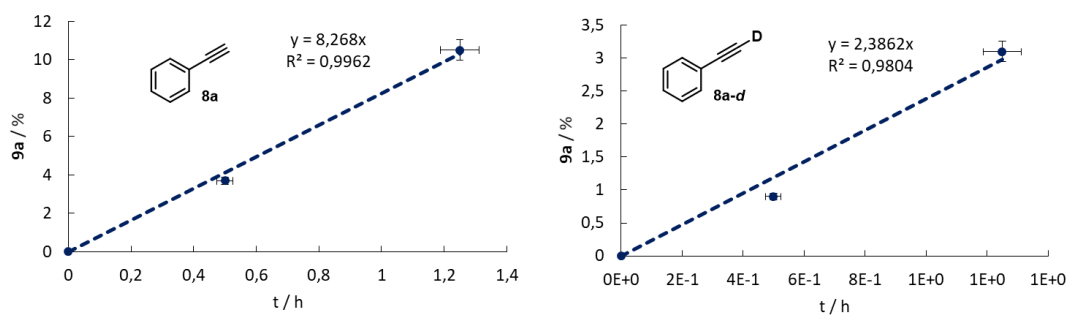


**Figure S35.** Yield-time plots for the homocoupling of **8a** catalyzed by SCC@MOF **4** under different atmospheres (see main text for general reaction conditions) and calculated initial rates.



Start. Mat.	$r_0$ (%/h)
<b>8a</b>	8.3
<b>8a-d</b>	2.4

$$\text{KIE} = k_{\text{H}} / k_{\text{D}} = 3.4(7)$$

**Figure S36.** Yield-time plots for the homocoupling of **8a** and **8a-d** catalyzed by SCC@MOF **4** showing a kinetic isotopic effect (see main text for general reaction conditions).

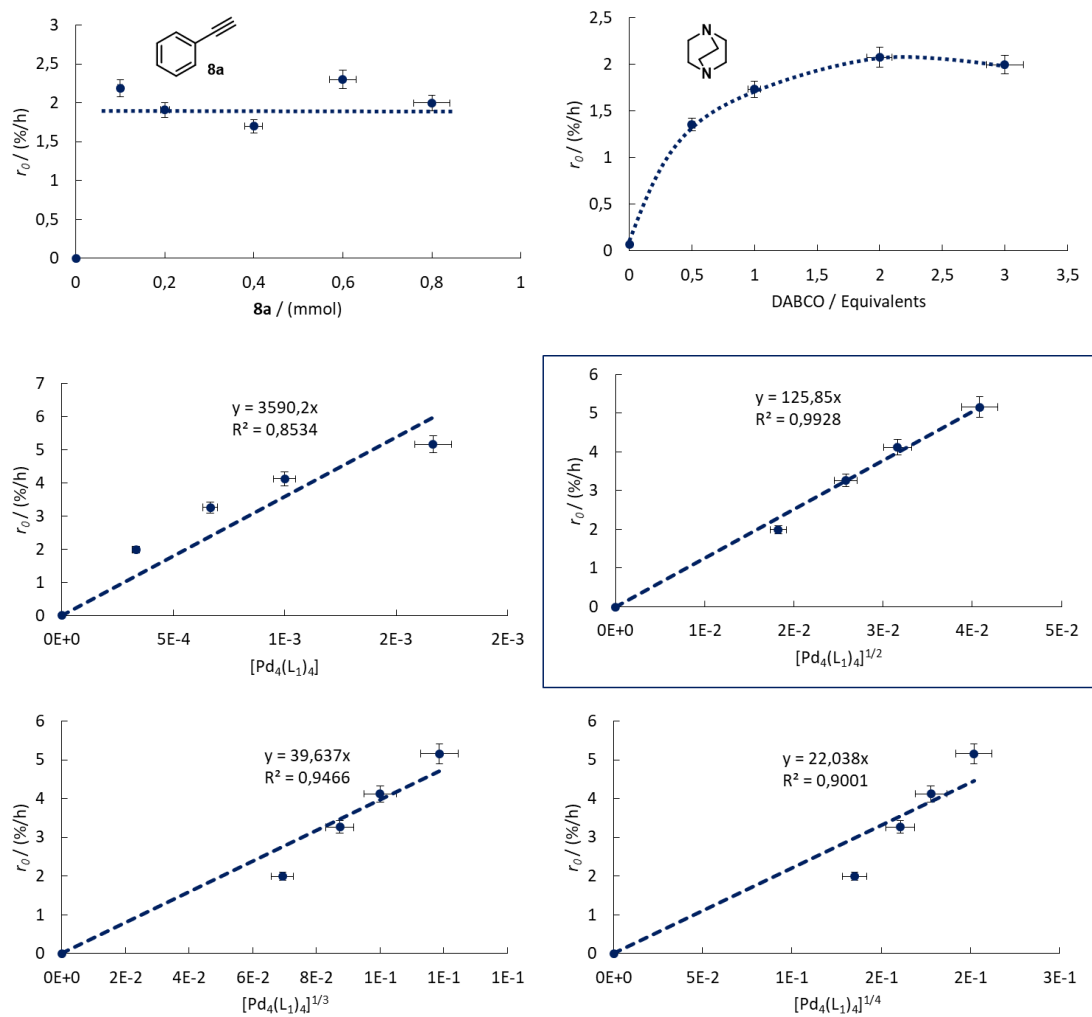


**Figure S37.** Initial rates vs. amount of the different reagents for the homocoupling of **8a** catalyzed by  $\text{Pd}_4(\text{L}_1)_4$  (in  $\text{CH}_3\text{CN}$ ). Data corresponding to  $\text{Pd}_4(\text{L}_1)_4$  are fitted to a linear regression and  $\text{Pd}_4(\text{L}_1)_4$  concentration is analyzed to the power of different squares to evaluate the possible dissociation of Pd atoms during reaction (see main text for general reaction conditions).  $\text{Pd}_4(\text{L}_1)_4$  fits to a 1/2 order kinetics. Error bars account for 5% uncertainty.

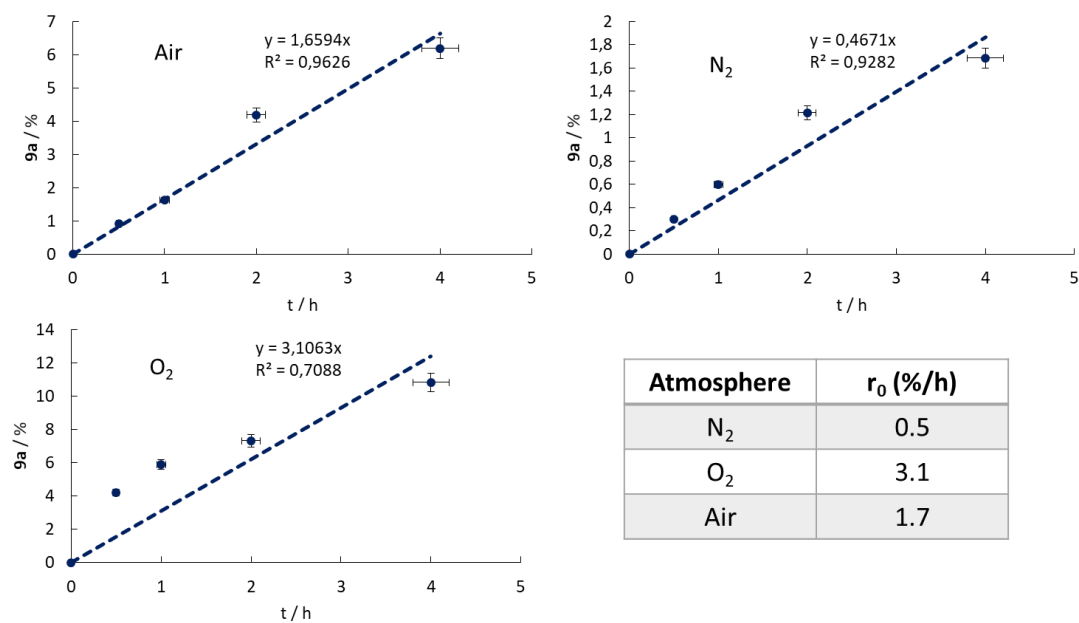
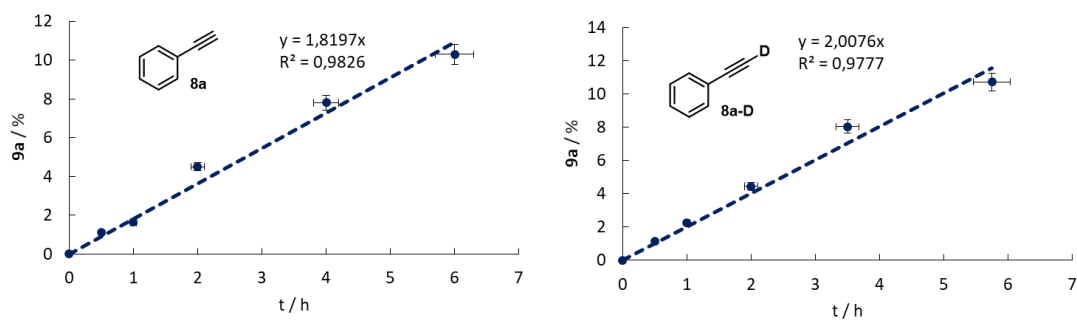


**Figure S38.** Yield-time plots for the homocoupling of **8a** catalyzed by Pd<sub>4</sub>(L<sub>1</sub>)<sub>4</sub> (in CH<sub>3</sub>CN) under different atmospheres (see main text for general reaction conditions) and calculated initial rates.



Start. Mat.	$r_0$ (%/h)
<b>8a</b>	1.8
<b>8a-d</b>	2.0

$$\text{KIE} = k_{\text{H}} / k_{\text{D}} = 0.9(1)$$

**Figure S39.** Yield-time plots for the homocoupling of **8a** and **8a-d** catalyzed by Pd<sub>4</sub>(L<sub>1</sub>)<sub>4</sub> (in CH<sub>3</sub>CN) to evaluate the possible kinetic isotopic effect (see main text for general reaction conditions).

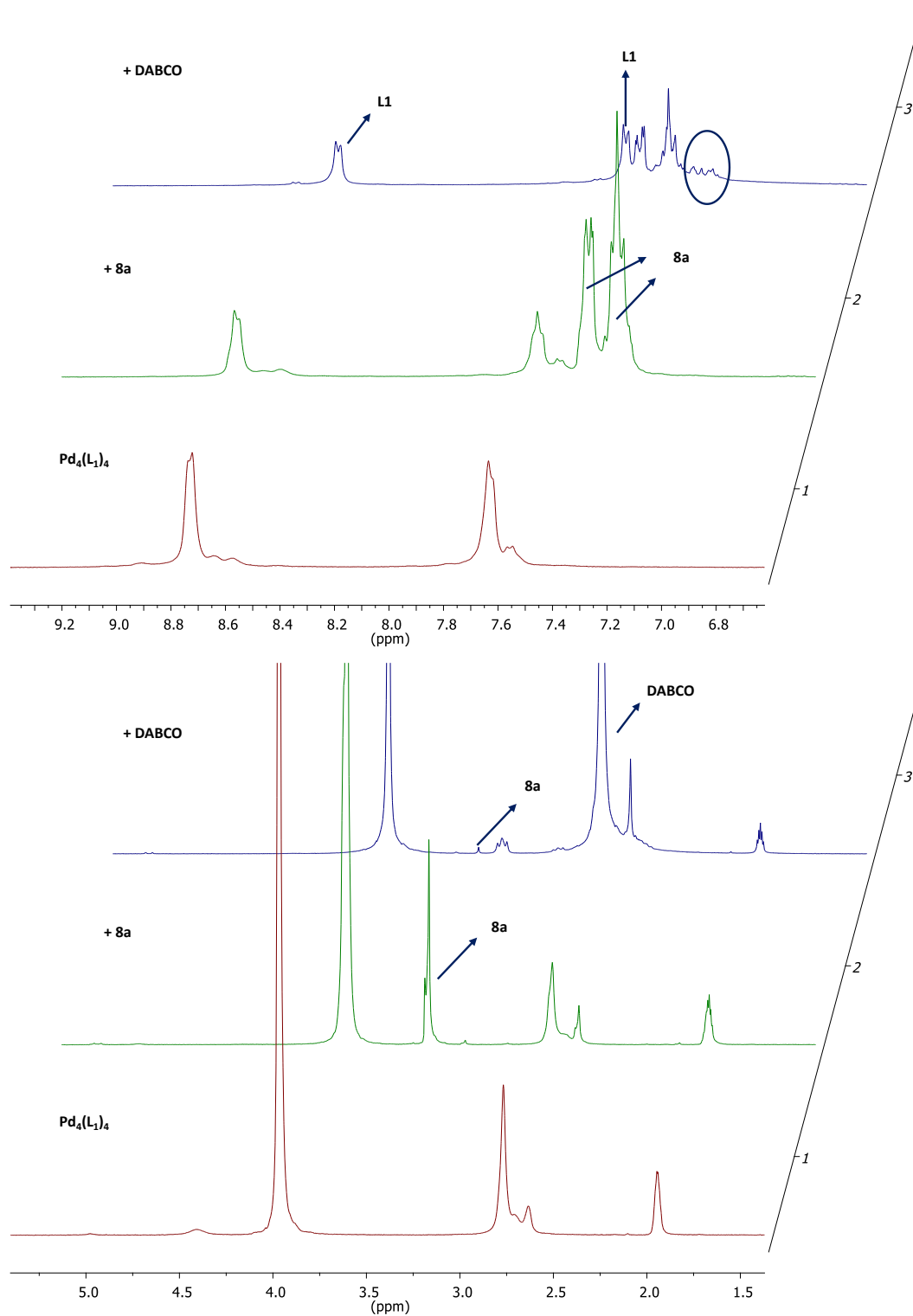


**Figure S40.** Aromatic area (top) and alkyl area (bottom) of the <sup>1</sup>H NMR spectra of Pd<sub>4</sub>(L<sub>1</sub>)<sub>4</sub> in CD<sub>3</sub>CN after sequential addition of all the reagents for the homocoupling of **8a**. Unidentified intermediate species are marked with a circle.

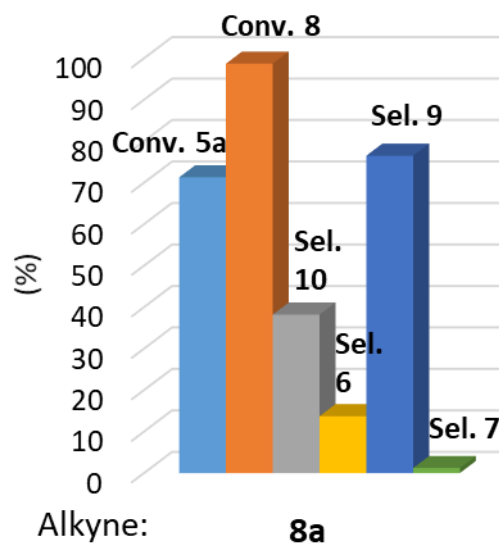
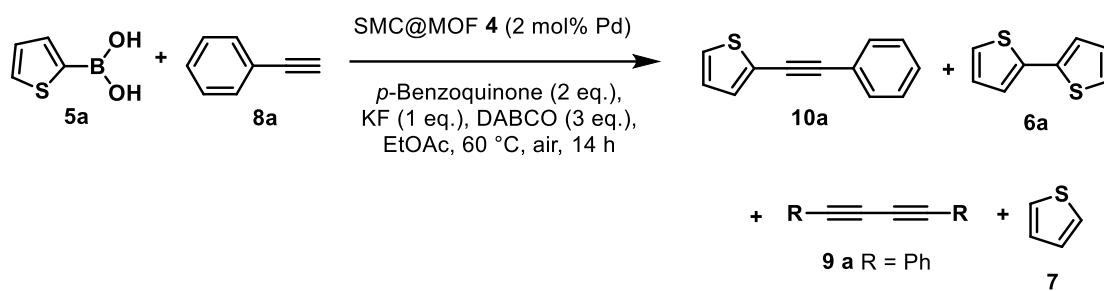


**Figure S41.** Results for the cross-coupling of boronic acid **5a** and phenylacetylene **8a** catalyzed by SCC@MOF **4** (see main text or general procedures for general reaction conditions).

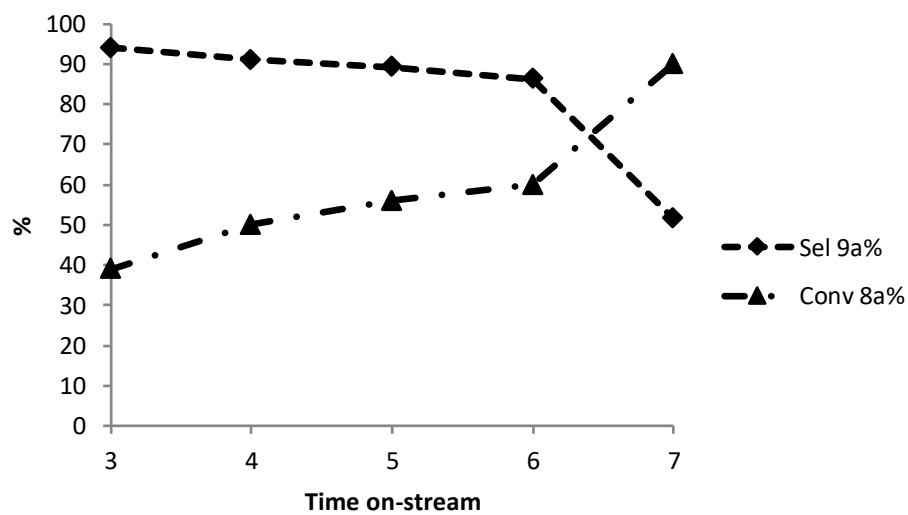


**Figure S42.** Homocoupling of **8a** in a fixed-bed tubular reactor containing the SCC@MOF **4**. Reaction conditions:  $0.01 \text{ ml}\cdot\text{min}^{-1}$  of a mixture of **8a** and DABCO (3 equiv.) in AcOEt (0.05 M) over 50 mg of **4** at  $60 \text{ }^\circ\text{C}$ .

**Supplementary References**

1. Schmidt, B., Berger, R., Kelling, A., Schilde, U. Pd-Catalyzed [2+2+1] Coupling of Alkynes and Arenes: Phenol Diazonium Salts as Mechanistic Trapdoors. *Chem. Eur. J.* **17**, 7032–7040 (2011).
2. Azcarate, I. *et al.* Generation of Photocurrent by Visible-Light irradiation of Conjugated Dawson Polyoxoxphosphovanadotungstate-Porphyrin Copolymers. *Chem. Eur. J.* **21**, 8271–8280 (2015).
3. Fujita, M. *et al.* On the structure of transition-metal-linked molecular squares. *Chem. Commun.* **0**, 1535–1536 (1996).
4. Fortea-Pérez, F. R. *et al.* The MOF-driven synthesis of supported palladium clusters with catalytic activity for carbene-mediated chemistry. *Nat. Mater.* **16**, 760–766 (2017).
5. (a) Evans, P. Sclaing and assessment of data quality. *Acta Cryst. D* **62**, 72–82 (2006). (b) Evans, P. R., Murshudov, G. N. How good are my data and what is the resolution?. *Acta Cryst. D* **69**, 1204–1214 (2013). (c) Winn, M. D. *et al.* Overview of the CCP4 suite and current developments. *Acta Cryst. D* **67**, 235–242 (2011). (d) Winter, G. *xia2*: and expert system for macromolecular crystallography data reduction. *J. Appl. Cryst.* **43**, 186–190 (2010). (e) Winter, G. *et al.* *DIALS*: implementation and evaluation of a new integration package *Acta Cryst.* **2018**, D74, 85-97
6. SAINT, version 6.45, Bruker Analytical X-ray Systems, Madison, WI, 2003.
7. Sheldrick G.M. SADABS Program for Absorption Correction, version 2.10, Analytical X-ray Systems, Madison, WI, 2003.
8. (a) Sheldrick, G. M. Crystal structure refinement with SHELXL. *Acta Cryst. C* **71**, 3–8 (2015). (b) Sheldrick, G. M. A short history of SHELX. *Acta Cryst. A*

- 64**, 112–122 (2008). (c) SHELXTL-2013/4, Bruker Analytical X-ray Instruments, Madison, WI, 2013.
9. (a) Spek, A. L. *PLATON SQUEEZE*: a tool for the calculation of the disordered solvent contribution to the calculated structure factors. *Acta Crystallogr. Sect. C-Struct. Chem.* **71**, 9–18 (2015). (b) Spek, A. L. Structure validation in chemical crystallography. *Acta Crystallogr. Sect. D, Biol. Crystallogr.* **65**, 148–155 (2009).
10. Farrugia, L. J. *WinGX* suite for small-molecule single-crystal crystallography. *J. Appl. Crystallogr.* **32**, 837–838 (1999).
11. D. Palmer, CRYSTAL MAKER, Cambridge University Technical Services, C. No Title, 1996.
12. Tominaga, M. *et al.* Finite, spherical coordination networks that self-organize from 36 small components. *Angew. Chem. Int. Ed.* **43**, 5621–5625 (2004).
13. Sun, Q.-F. *et al.* Self-Assembled  $M_{24}L_{48}$  Polyhedra and Their Sharp Structural Switch upon Subtle Ligand Variation. *Science* **328**, 1144–1147 (2010).
14. Fujita, D. *et al.* Self-assembly of tetravalent Goldberg polyhedra from 144 small components. *Nature* **540**, 563–566 (2016).
15. Fujita, M. *et al.* On the structure of transition-metal-linked molecular squares. *Chem. Commun.* **0**, 1535–1536 (1996).
16. Mon, M. *et al.* Selective gold recovery and catalysis in a highly flexible methionine-decorated metal-organic framework. *J. Am. Chem. Soc.* **138**, 7864–7867 (2016).
17. Doménech-Carbó, A., Leyva, A., Al-Resayes, A. and Corma, A. Electrochemical monitoring of the oxidative coupling of alkynes catalyzed by

- triphenylphosphine gold complexes. *Electrochem. Commun.* **19**, 145-148 (2012).
18. Doménech-Carbó, A., Labuda, J. and Scholz, F. Electroanalytical chemistry for the analysis of solids: characterization and classification (Technical Report). *Pure Appl. Chem.* **85**, 609-631 (2013).
19. Kohler, D. G., Gockel, S. M., Kennemur, J. L., Waller, P. J. and Hull., K. L. Palladium-catalysed anti-Markovnikov selective oxidative amination *Nat. Chem.* **10**, 333-340 (2018).
20. Nising, C. F., Schmid, U. K., Nieger, M. and Brase, S. A New Protocol for the One-Pot Synthesis of Symmetrical Biaryls. *J. Org. Chem.* **69**, 6830–6833 (2004).
21. Billingsley, K. and Buchwald, S. L. Highly Efficient Monophosphine-Based Catalyst for the Palladium-Catalyzed Suzuki-Miyaura Reaction of Heteroaryl Halides and Heteroaryl Boronic Acids and Esters. *J. Am. Chem. Soc.* **129**, 3358–3366 (2007).
22. Bandari, R., Hoche, T., Prager, A., Dirnberger, K. and Buchmeiser, M. R. Ring-Opening Metathesis Polymerization Based Pore-Size-Selective Functionalization of Glycidyl Methacrylate Based Monolithic Media: Access to Size-Stable Nanoparticle for Ligand-Free Metal Catalysis. *Chem. Eur. J.* **16**, 4650–4658 (2010).
23. Kuroboshi, M., Waki, Y. and Tanaka, H. Palladium-Catalyzed Tetrakis(dimethylamino)ethylene-Promoted Reductive Coupling of Aryl Halides. *J. Org. Chem.* **68**, 3938–3942 (2003).

24. Ozasa, S., Fujioka, Y., Okada, M., Izumi, H. and Ibuki, E. Synthesis and Physical Properties of Several Deuterium-labelled Polyphenols. *Chem. Pharm. Bull.* **29**, 370–378 (1981).
25. Park, J. *et al.* Pd-Catalyzed Decarboxylative Coupling of Propiolic Acids: One-Pot Synthesis of 1,4-Disubstituted 1,3-Diynes via Sonogashira–Homocoupling Sequence. *J. Org. Chem.* **76**, 2214–2219 (2011).
26. Schmidt, R. *et al.* Fast, Ligand- and Solvent-Free Synthesis of 1,4-Substituted Buta-1,3-diynes by Cu-Catalyzed Homocoupling of Terminal Alkynes in a Ball Mill. *Chem. Eur. J.* **17**, 8129–8138 (2011).
27. Zhang, S., Liu, X. and Wang, T. An Efficient Copper-Catalyzed Homocoupling of Terminal Alkynes to Give Symmetrical 1,4-Disubstituted 1,3-Diynes. *Adv. Synth. Catal.* **353**, 1463–1466 (2011).
28. Huang, H., Jiang, H., Cheng, K. and Liu, H. Efficient Iron/Copper Cocatalyzed Alkynylation of Aryl Iodides with Terminal Alkynes. *J. Org. Chem.* **73**, 9061–9064 (2008).